



THE HONG KONG
POLYTECHNIC UNIVERSITY

香港理工大學

Pao Yue-kong Library

包玉剛圖書館

Copyright Undertaking

This thesis is protected by copyright, with all rights reserved.

By reading and using the thesis, the reader understands and agrees to the following terms:

1. The reader will abide by the rules and legal ordinances governing copyright regarding the use of the thesis.
2. The reader will use the thesis for the purpose of research or private study only and not for distribution or further reproduction or any other purpose.
3. The reader agrees to indemnify and hold the University harmless from and against any loss, damage, cost, liability or expenses arising from copyright infringement or unauthorized usage.

IMPORTANT

If you have reasons to believe that any materials in this thesis are deemed not suitable to be distributed in this form, or a copyright owner having difficulty with the material being included in our database, please contact lbsys@polyu.edu.hk providing details. The Library will look into your claim and consider taking remedial action upon receipt of the written requests.

The Hong Kong Polytechnic University

Department of Applied Physics

**MAGNETOELECTRIC EFFECT AS A
FUNCTION OF LATTICE COUPLING AND
MICROSTRUCTURE IN
FERROELECTRIC/MAGNETOSTRICTIVE
COMPOSITES**

SUN LI

A thesis submitted in partial fulfillment of the requirements for
the degree of Doctor of Philosophy

July 2012



CERTIFICATE OF ORIGINALITY

I hereby declare that this thesis is my own work and that, to the best of my knowledge and belief, it reproduces no material previously published or written nor material which has been accepted for the award of any other degree or diploma, except where due acknowledgement has been made in the text.

_____ (Signed)

_____ Li Sun _____ (Name of student)



ABSTRACT

Magnetolectric (ME) effect is defined as the induction of dielectric polarization P by an applied magnetic field H (i.e. direct ME effect, or ME_H effect: $P = \alpha H$, where α is called coupling coefficient), and/or the induction of magnetization M by an external electric field E (i.e. converse ME effect, or ME_E effect: $M = \alpha' E$). Among all the composite materials reported in the literature, systems that consist of a piezoelectric phase (represented by $BaTiO_3$, PZT, PVDF and etc.) and a magnetostrictive phase (represented by Terfenol-D, $CoFe_2O_4$ and etc.) are most widely investigated. ME effect in composites, normally measured by the ME coupling efficient, α , is influenced by a number of factors including composition and structure of each individual phase, the way that all phases are connected, external electrical/magnetic conditions, and so on. While significant progress has been made on the research and development of ME composites over the last decade, there are still a number of questions remaining to be answered.

The research work for this thesis has been focusing on the following three issues, which, as we believe, are critical for better understanding of the structure - property relationship in ferroelectric/magnetostrictive composites: direct observation of lattice coupling, analysis of nonlinear piezoelectric response of the ferroelectric phase and analysis of the percolation effect due to the low-resistivity magnetostrictive phase. More details are given below.

First, an experiment was conducted for direct observation of coupled lattice distortion of the ferroelectric and magnetostrictive components in a 0 - 3 type composite consisting of PZT and CFO. In the experiment, the composite sample was



prepared via conventional ceramic processing. With a static electric field applied on the composite, changes in lattice parameter of both PZT and CFO were observed by means of X-ray diffraction running in an ultra-slow mode. The experimental results have verified a coupled lattice distortion in the composite, providing an experimental evidence for the long-existing assumption that the ME effect is based on mechanical coupling. Based on the lattice distortion under different electrical fields, the ME coupling coefficient was estimated and found to match well with experimental data.

Secondly, the influence of microstructural inhomogeneity on the magnetoelectric coupling effect was studied. It is important to note that the piezoelectric coefficient of PZT is sensitive to electrical field strength. In a 0 - 3 composite, the electrical field around CFO particles could be distorted due to the relatively low-resistivity of CFO. Analysis was made to investigate how such electrical field inhomogeneity would affect the performance of the composite via finite element analysis method. An averaged method was developed to evaluate the overall piezoelectric property. The computation results show that the difference in electrical property between PZT and CFO causes a large weakening in PZT's piezoelectric property. Such weakening effect concentrates in the interaction regions between the two phases, which will finally cause an enlarged weakening in the converse magnetoelectric effect.

Thirdly, the influence of percolation effect on the magnetoelectric performance of the composite has been studied by numerical approach. The percolation effect in the composite is also due to the relatively low resistivity of CFO. As a result, there exists an upper limit to the volume fraction of the magnetostrictive phase and consequently a limit to the coupling coefficient as well. Such percolation problem could be



solved through modification of the microstructure - in particular the grain boundaries in the composite. Numerical approaches have been made to reveal how effective it could be to improve the coupling effect through modification of the grain boundaries. Experiments were also conducted to verify the effect. In the experiment, composites with a core-shell type of microstructure were prepared. Wrapped with a thin layer of zirconia, CFO particles became electrically resistive and they would not form electrical conduction paths in the composite. With the shell to act as a barrier to electron and vacancy transportation, the leakage current of the composite material was significantly reduced, giving rise to enhanced coupling effect.

In addition to the above work, effort has also been made to develop prototype devices using PZT - CFO composites as key materials. One of the important devices that have been developed was a magnetically tunable piezoelectric-transformer. The device are designed with a step-down transformer structure and its response to both AC electric field (with/without DC bias) and an AC magnetic field were investigated respectively, which showed good sensitivity to both DC and AC magnetic field and are potentially useful for magnetic field detection.



LIST OF PUBLICATIONS

1. **L. Sun**, T. Y. Sun, Y. M. Hu, H. S. Gu, H. L. W. Chan and Y. Wang, “Direct observation of coupled lattice distortion in $\text{Pb}(\text{Zr,Ti})\text{O}_3 - 0.05\text{CoFe}_2\text{O}_4$ magnetoelectric composite”, submitted to *Journal of the American Ceramic Society*.
2. **L. Sun**, L. F. Fei, H. L. W. Chan and Y. Wang, “Abnormally enhanced magnetization in bismuth ferrite nanoparticles coated with zirconia”, submitted to *Journal of the American Ceramic Society*.
3. **L. Sun**, Y. Wang, T. Y. Sun, Z. H. Yong, L. Yan, K. Li, C. W. Nan and H. L. W. Chan, “Study of the influence of microstructural inhomogeneity on the magnetoelectric coupling effect in piezoelectric - magnetostrictive composites: a numerical approach”, submitted to *Journal of Applied Physics*.
4. J. Q. Qi, **L. Sun**, P. Du and L. T. Li, “Slurry synthesis of bismuth sodium titanate with transient aurivillius-type structure”, *Journal of the American Ceramic Society*, 93(4): 1044 - 1048 (2010).
5. J. Q. Qi, **L. Sun**, P. Du , W. P. Chen, Y. G. Xu and L. T. Li, “Stoichiometry of BaTiO_3 nanoparticles”, *Journal of Nanoparticles Research*, 12(7): 2605 - 2609 (2010).
6. J. Q. Qi, **L. Sun**, Y. Wang, W. P. Chen, P. Du, Y. G. Xu, L. T. Li, C. W. Nan and H. L. W. Chan, “Excess titanium in barium titanate nanoparticles directly synthesized from solution”, *Journal of Physics and Chemistry of Solids*, 71: 1676 - 1679 (2010).



7. J. Q. Qi, **L. Sun**, Y. Wang, W. P. Chen, P. Du, Y. G. Xu, L. T. Li, C. W. Nan and H. L. W. Chan, “Low-temperature synthesis and analysis of barium titanate nanoparticles with excess barium”, *Advanced Powder Technology*, 22(3): 401 - 404 (2011).
8. J. Q. Qi, **L. Sun**, X. W. Qi, Y. Wang and H. L. W. Chan, “Grain size modulation on BaTiO₃ nanoparticles synthesized at room temperature”, *Journal of Solid State Chemistry*, 184(10): 2690 - 2694 (2011).
9. J. Q. Qi, T. Peng, Y. M. Hu, **L. Sun**, Y. Wang, W. P. Chen, L. T. Li, C. W. Nan and H. L. W. Chan, “Direct synthesis of ultrafine tetragonal BaTiO₃ nanoparticles at room temperature”, *Nanoscale Research Letters*, 6: 466, 4pp(2011).
10. **L. Sun**, L. Yan, K. Li, H. L. W. Chan and Y. Wang, “Enhanced magnetoelectric coupling effects in PZT - CFO composites through grain boundary modifications”, in preparation.

The following are conference presentations:

1. **L. Sun**, T. Y. Sun, Z. H. Yong, H. L. W. Chan and Y. Wang, “Distribution of electrical fields inside a magnetoelectric nanocomposite and its influence on the magnetoelectric coupling effect”, Chinese Microstructures & Functional Materials Meeting, Nanjing, China, Aug 22 - 23, 2011.
2. **L. Sun**, L. F. Fei, H. L. W. Chan and Y. Wang, “Development and characterization of bismuth ferrite-based nanoceramics with a core-shell type microstruc-



ture”, presented at MRS Spring Meeting, San Francisco, USA, April 24 - 29, 2011

3. *L. Sun*, Y. Wang and H. L. W. Chan, “Enhancement of magnetoelectric coupling effects in ferroelectric/magnetic composites through microstructure modification”, presented at the Chinese Materials Society Annual Meeting, Beijing, May 18 - 20, 2011.



ACKNOWLEDGEMENTS

I would like to deeply thank my supervisors, Prof. H. L. W Chan and Dr. Y. Wang for their excellent supervision and invaluable advice throughout the whole study period. I would also like to thank Prof. K. H. Wong, Prof. C. W. Nan, Prof. K. Li, Prof. J. Q. Qi, and Dr. Y. M. Hu for their assistance on my research and course-work studies.

I would like to thank Mr. M. N. Yeung of the Materials Research Centre for his assistance in the structure characterization.

I would like to give my thanks to colleagues and friends in AP for their help and assistance. They include Dr. T. Y. Sun, Mr. Z. H. Yong, Mr. L. F. Fei, Dr. G. Y. Gao, Dr. S. M. Ke, Ms. Y. J. Zhang, Ms. L. Yan, Mr. F. L. Li, Mr. F. Cao, Ms. J. Z. Xin, Ms. S. M. Wang and Ms. L. L. Tao.

I gratefully acknowledge the Hong Kong Polytechnic University for affording me this opportunity to pursue PhD degree at the Department of Applied Physics.

Most of all, I would like to thank my parents for their love, understanding and support throughout the period of my undergraduate and postgraduate studies. I admire my parents greatly for their utmost effort towards achieving their level of success in both career and family.



TABLE OF CONTENTS

LIST OF PUBLICATIONS	V
ACKNOWLEDGEMENTS.....	VIII
TABLE OF CONTENTS.....	IX
LIST OF FIGURE CAPTIONS.....	XVII
LIST OF TABLE CAPTIONS.....	XXV
CHAPTER 1 Introduction	1
1.1 Introduction to magnetoelectric materials.....	1
1.1.1 Early history of ME coupling.....	1
1.1.2 ME material development.....	2
1.2 Magnetoelectric composites.....	5
1.2.1 Origin of magnetoelectricity in composites.....	6
1.2.2 Features of magnetoelectricity in composites.....	9
1.2.3 Linear approximation of magnetoelectricity in composites.....	10
1.2.4 Magnetoelectric composite systems.....	11
1.2.5 Potential applications of ME materials	15
1.3 0 - 3 type magnetoelectric composites.....	16



1.3.1	A short introduction to 0 - 3 type particulate composites	17
1.3.2	Typical experimental results of 0 - 3 particulate ME ceramics..	19
1.3.3	Theories of 0 - 3 type particulate ME ceramics	27
1.3.4	Some key issues in 0 - 3 type ME ceramic composites	30
1.4	Scope of the present study.....	33
1.5	Statement of original contribution	35
CHAPTER 2 Techniques for the study of 0 - 3 type $\text{Pb}(\text{Zr}, \text{Ti})\text{O}_3$ - CoFe_2O_4		
	composites	37
2.1	Introduction	37
2.2	Ferroelectric measurement	38
2.2.1	Background	38
2.2.2	Experimental set-ups.....	38
2.3	Magnetoelectric measurement	40
2.3.1	Experimental set-ups.....	40
2.3.2	Determination of the direct magnetoelectric coefficient.....	41
2.4	X-ray Diffraction (XRD).....	42
2.4.1	Principle of XRD measurement techniques	43
2.4.2	The instrument	44



2.5 Scanning electron microscope.....	45
2.5.1 General principle.....	45
2.5.2 Secondary electron image	46
2.5.3 Backscattered electron image.....	47
2.6 Finite element analysis (FEA).....	48
2.6.1 General principle.....	48
2.6.2 Modeling of piezoelectric and magnetostrictive problems	49
2.6.3 Simulation using COMSOL multi-physics software	51
2.7 Summary	54
CHAPTER 3 Direct observation of lattice coupling in 0 - 3 Type Pb(Zr, Ti)O ₃ - CoFe ₂ O ₄ composites	55
3.1 Introduction.....	55
3.2 Investigation of grain lattice by X-ray diffraction	56
3.2.1 Determination of lattice constant by XRD.....	57
3.2.2 Determination of lattice strain by XRD	59
3.3 Prior investigations of the coupled magnetoelectric effect	61
3.4 Experimental procedure	64
3.4.1 Preparation and structural characterization of 0 - 3 type Pb(Zr,	



Ti)O ₃ - CoFe ₂ O ₄ composites	64
3.4.2 Poling and piezoelectric measurements	64
3.4.3 XRD study of the composite under electric field.....	64
3.5 Structures and morphology of the composites	65
3.5.1 Crystal structure of CFO, PZT and 0 - 3 type PZT - CFO composites.....	65
3.5.2 Microstructure of 0 - 3 type PZT - CFO composite.....	67
3.6 XRD study of the converse magnetoelectric effect.....	68
3.6.1 Experiments.....	68
3.6.2 Results and discussions	69
3.7 Derivation of magnetoelectric coefficient based on coupled lattice strain.....	73
3.7.1 Strain-field relationship in PZT and CFO	73
3.7.2 Estimation of the magnetoelectric coefficient in the PZT - CFO composite: a universal condition.....	74
3.7.3 Estimation of the magnetoelectric coefficient in the 0 - 3 type PZT - CFO composite	76
3.8 Summary	78



CHAPTER 4 Magnetolectric coefficient vs. microstructures in piezoelectric/magnetostrictive composites: A numerical approach	79
4.1 Introduction	79
4.2 Theory and simulation method.....	81
4.2.1 General consideration.....	81
4.2.2 Modeling the magnetostrictive effect.....	81
4.2.3 Numerical approach	83
4.2.4 Simulation process	84
4.3 Results and discussions	86
4.3.1 1 - 3 composite	87
4.3.2 0 - 3 composite	89
4.3.3 A short discussion	92
4.4 Evaluating the coupling efficiency.....	95
4.4.1 Lattice coupling at the interface	95
4.4.2 Coupling efficiency in two sets of lattices	97
4.4.3 Coupling efficiency in polycrystalline materials	100
4.5 Summary	102



CHAPTER 5 Study on the influence of microstructural inhomogeneity on magnetoelectric effect.....	104
5.1 Introduction.....	104
5.1.1 Electric-field-related process in 0 - 3 type ME composites.....	105
5.1.2 Previous solution to the inhomogeneous microstructural property.....	106
5.2 The inhomogeneous electric field in 0 - 3 type composites.....	106
5.2.1 Origin of the inhomogeneous electric field in ME composites	107
5.2.2 Materials and models to study the inhomogeneous electric field.....	109
5.2.3 Electric field distribution.....	110
5.3 The inhomogeneous electric field vs. piezoelectric poling.....	112
5.3.1 Introduction to piezoelectric poling.....	112
5.3.2 Inhomogenous poling efficiency within 0 - 3 type composites	113
5.4 The inhomogeneous electric field vs. local d_{33} upon application.....	115
5.4.1 Introduction to the non-linear piezoelectric effect.....	115
5.4.2 Averaged d_{33}	116
5.4.3 Relationship between CFO's volume fraction and the averaged	



d_{33}	119
5.4.4 Overall d_{33}	121
5.4.5 Overall magnetoelectric coefficient, $\alpha_{E, 33}$	122
5.5 Summary	123
CHAPTER 6 0 - 3 type CFO - PZT composite with enhanced piezoelectric and magnetoelectric properties	125
6.1 Introduction	125
6.2 Highly resistive CFO - PZT composites	126
6.2.1 Synthesis of the CFO - PZT composites with high resistivity .	128
6.2.2 Optimization of the experimental conditions.....	130
6.2.3 Microstructural characterization of the ZrO_2 - CFO particles .	131
6.2.4 Microstructural characterization of the PZT - CFO composite	133
6.2.5 Mechanism of the microstructural modification	137
6.3 Magnetoelectric property of the CFO - PZT composite with modified microstructure	140
6.3.1 Dielectric property	141
6.3.2 Ferroelectric property.....	143
6.3.3 Piezoelectric property.....	144



6.3.4	Magnetolectric property	144
6.4	Transformer design	146
6.4.1	Electrical property of the composite	147
6.4.2	The transformer structure	149
6.4.3	Impedance spectra of the transformer structure	150
6.4.4	The transformer's response to electric/magnetic signal	151
6.4.5	Coupled effect in the transformer	153
6.5	Summary	155
CHAPTER 7	Conclusion and future work	156
7.1	Conclusion	156
7.2	Future work	159
Reference	161



LIST OF FIGURE CAPTIONS

- Fig. 1.1 Temperature dependence of the magnetoelectricity in Cr_2O_3 [11]. 2
- Fig. 1.2 Lattice structure of perovskite BiFeO_3 in the absence ($E = 0$) or presence ($E \neq 0$) of an electric field. 4
- Fig. 1.3 Lattice structure of hexagonal HoMnO_3 in the absence ($E = 0$) or presence ($E \neq 0$) of an electric field. 4
- Fig. 1.4 Illustration of the magnetoelectric effect in ferroelectric - ferromagnetic composites..... 7
- Fig. 1.5 Magnetolectric hysteresis curve showing the magnetic response of the PZT - NZFO - Ni bilayer system as a function of the applied electric field. The factor R in figures (a) to (d) stands for the ferrite-to-Ni thickness ratio. MEVC stands for the magnetoelectric voltage coefficient. [36]..... 10
- Fig. 1.6 Microstructure of the first ME composite by Suchtelen [36]. Samples were fabricated by unidirectional solidification of an eutectic composition of the quinary system Fe - Co - Ti - Ba - O. 12
- Fig. 1.7 Schematic illustration of three bulk composites with the three common connectivity schemes. (a) 0 - 3 particulate composite, (b) 2 - 2 laminate composite and (c) 1 - 3 fiber/rod composite. 17
- Fig. 1.8 Maximum ME voltage coefficient of the PZT and Ni-ferrite particulate composites as functions of sintering temperature and Ni-ferrite particle contents. 21



Fig. 1.9	Frequency dependence of transverse ME coefficient for samples with 5 % and 40 % porosity. [111]	21
Fig. 1.10	Static magnetic field H dependence of the longitudinal ME coefficient $\alpha_{E,33}$ for bulk composites of nickel ferrite and lead zirconate titanate (PZT). The data at room temperature and 1 kHz are for samples with porosity $p = 5\%$ and 40% . [111]	22
Fig. 1.11	Scanning electron microscopy images of the NFO - PZT composite ceramics via SPS. (a) Polished surface and (b) fractured surface	23
Fig. 1.12	Comparison of the ME coefficients of the 0 - 3 type NFO - PZT ceramic composites via SPS and conventional sintering	24
Fig. 1.13	Schematic diagrams of distribution of CoFe_2O_4 phase (in black) in BaTiO_3 matrix in two different ways. (a) Composite materials prepared by mixing and sintering method and (b) composite materials produced by one-pot approach. [115]	26
Fig. 1.14	Calculated $\alpha_{E,33}$ for 0 - 3 or 1 - 3 $\text{CoFe}_2\text{O}_4/\text{BaTiO}_3$ ceramic composites (BaTiO_3 as the matrix phase). [33]	30
Fig. 2.1	A typical ferroelectric hysteresis loop	38
Fig. 2.2	A schematic circuit of the Sawyer - Tower bridge	39
Fig. 2.3	A schematic diagram of the hysteresis measurement	40
Fig. 2.4	A schematic diagram of the set-ups for magnetoelectric measurement ..	41
Fig. 2.5	Illustration for the (a) lattice grains and (b) Bragg's law	43
Fig. 2.6	The Rigaku automated multipurpose Smartlab X-ray diffractometer	44



Fig. 2.7	Illustration of interaction volumes for various electron - specimen interactions.	47
Fig. 2.8	Schematic illustration of determination of magnetoelectric coupling coefficient.....	50
Fig. 2.9	Illustration for the modeling of piezoelectric ceramic through COMSOL multi-physics software. (a) The operation geometric model, (b) the meshes generated in COMSOL by default options, (c) the displacement at the upper surface and (d) the displacement at the bottom surface.	53
Fig. 3.1	Illustration of a typical peak in XRD patterns.	57
Fig. 3.2	Two types of strain-induced lattice deformation and the corresponding XRD peak. (a) Original lattice without strain, (b) lattice with uniform expansion and (c) lattice with non-uniform deformation.....	60
Fig. 3.3	XRD pattern of the LBMO/PMN - PT structure. Insets (a) and (b) are the ferroelectric hysteresis loop of the PMN - PT substrate and the electrical measurement circuit, respectively. [146]	62
Fig. 3.4	Lattice constant c of the PMN - PT substrate and LBMO film as a function of the electric field. Insets (a) and (b) show the temperature and field dependence of the resistance for the LBMO film, respectively. [146]	63
Fig. 3.5	Illustration of the sample used for XRD measurement.....	66
Fig. 3.6	XRD patterns of (a) PZT, (b) CFO and (c) PZT - CFO ceramics.....	66
Fig. 3.7	TEM images of the PZT - CFO ceramic at (a) low and (b) high	



	magnification. The inset of (a) is the corresponding SAED pattern.	67
Fig. 3.8	Illustration of the $\theta - 2\theta$ scan used in the measurement.	68
Fig. 3.9	XRD patterns of PZT - CFO ceramic composite during the measurement. (a) $20^\circ - 70^\circ$ scan, (b) PZT (211) peak and (c) CFO (511) peak.	70
Fig. 3.10	Two connection modes. (a) series connection and (b) parallel connection.	72
Fig. 3.11	The relationship between CFO's strain and PZT's strain under ideal series connection and parallel connection.	72
Fig. 3.12	Calculated relationship between ME coupling coefficient and the magnetic field under a static DC bias for PZT - CFO composite with ideal parallel connection, series connection and 0 - 3 type connectivity.	77
Fig. 4.1	The process of the self-consistent process.	84
Fig. 4.2	Simulation results for the 1 - 3 type PZT - CFO composite. (a) The geometric construction of the structure; (b) The distribution of electric potential, and the slice is along the center of the structure; (c) The total displacement of CFO matrix; (d) Output electric field vs. input magnetic field; (e) dE/dH vs. input magnetic field.	89
Fig. 4.3	Simulation results for the 0 - 3 type PZT - CFO composite. (a) The particles distribute in the matrix randomly, and the figure gives the result in one of the simulations; (b) The distribution of electric potential on center of the slice of piezoelectric solid in one of the simulations; (c) The total displacement of piezoelectric matrix; (d) The total displacement of magnetic particles; (e) Output electric field vs. input magnetic field; (f)	



	dE/dH vs. input magnetic field.....	91
Fig. 4.4	Lattice coupling models at the interface.	97
Fig. 4.5	Lattice coupling between two sets of 1D lattices.....	99
Fig. 5.1	The electric dipoles in piezoelectric material. (a) Before (ferroelectric ceramic), (b) during and (c) after poling (piezoelectric ceramic).	105
Fig. 5.2	Illustration of the inhomogeneous electric field. (a) Electric field intensity within composites with no conducting particles, (b) electric field intensity within composites with conducting particles, (c) electric field direction within composites with no conducting particles and (d) electric field direction within composites with conducting particles. The grey levels in figures (a) and (b) stand for the value of local field intensity. The arrows in figures (c) and (d) stand for the direction of local field.	108
Fig. 5.3	Illustration for the unit model of 0 - 3 type composite.	110
Fig. 5.4	Distribution of local electric field in the unit model. (a) Schematic diagram of the unit model, (b) two slices selected, (c) local electric field along z direction (E_z) in the slice $x = 0.1$ and (d) local electric field along z direction (E_z) in the slice $x = 0.3$	111
Fig. 5.5	Piezoelectric elementary cell (a) above and (b) below the Curie point (T_c).	112
Fig. 5.6	The relationship between poling field and piezoelectric effect. [170]...	114
Fig. 5.7	Distribution of local piezoelectric property (d_{33}) in (a) the slice $x = 0.1$ and (b) the slice $x = 0.3$	116



Fig. 5.8	The $d_{33, \text{average}}/d_{33, 0}$ value in the unit-cell model.....	119
Fig. 5.9	The $d_{33, \text{average}}/d_{33, 0}$ value as a function of position (described with distance to the CFO center) in composites with different volume percentages of CFO.....	120
Fig. 5.10	The calculated magnetoelectric effect. The straight curve stands for the condition in which non-linear piezoelectricity is not included. The dash curve stands for the condition in which non-linear piezoelectricity is included.....	123
Fig. 6.1	Illustration for the highly resistive PZT - CFO composite.	127
Fig. 6.2	The working principle of the highly resistive composite. (a) No CFO particle is modified with a highly resistive shell; (b) and (c) stand for the condition that one or more of the particles are modified with highly resistive shells; (d) All the CFO particles are modified with highly resistive shells.	128
Fig. 6.3	TEM images of ZrO_2 coated CFO particles prepared with solution with different concentrations of zirconium n-butoxide. (a) 0.1 mol/L, (b) 0.19 mol/L and (c) 0.27 mol/L.	131
Fig. 6.4	XRD pattern of the ZrO_2 -coated CFO particles.....	132
Fig. 6.5	(a) TEM image of CFO particle coated with ZrO_2 particles. (b) and (c) gives the HRTEM image of two edges of the ZrO_2 coated CFO particle. (d) The dispersed ZrO_2 particles.	133
Fig. 6.6	XRD patterns of $x\text{CFO} - (1 - x)\text{PZT502}$ ($x = 0.15, 0.3$ and 0.45) particulate ceramic composites prepared with ZrO_2/CFO particles.....	134



Fig. 6.7	STEM-BSE image of the 0.15CFO - 0.85PZT ceramic composites prepared with ZrO ₂ /CFO particles.	135
Fig. 6.8	SEM-EDX element maps of the 0.15CFO - 0.85PZT ceramic composites.	136
Fig. 6.9	SEM-EDX analysis of the 0.15CFO - 0.85PZT ceramic composites (linear scan). (a) SEM image and (b) elemental analysis.....	137
Fig. 6.10	The percolation threshold as a function of the fraction of ZrO ₂ modified CFO particles in the PZT - CFO particulate composites.	139
Fig. 6.11	(a) Dielectric constant and (b) loss of x CFO - (1 - x)PZT502 composites. ($x = 0.15, 0.30$ and 0.45)	142
Fig. 6.12	Ferroelectric hysteresis loops of x CFO - (1 - x)PZT502 composites. ($x = 0.15, 0.30$ and 0.45).....	143
Fig. 6.13	(a) Frequency dependence of impedance for x CFO - (1 - x)PZT502 ($x = 0.15, 0.3$ and 0.45) composites. (b) Variations of α_E with $H_{DC} = 9$ kOe at different frequencies of x CFO - (1 - x)PZT502 composites. The inset is the DC magnetic field dependent variation of α_E at EMR frequency. ...	146
Fig. 6.14	Cole-Cole plots of the 0.15CFO - 0.85PZT sample at room temperature.	148
Fig. 6.15	Frequency dependence of the AC impedance's real part and imaginary part for the 0.15CFO - 0.85PZT sample.	148
Fig. 6.16	Schematic diagram of the piezoelectric transformer structure.....	149
Fig. 6.17	Frequency dependence of the impedance and phase for the transformer	



structure. (a) 10 - 1250 kHz and (b) 95 - 105 kHz..... 150

Fig. 6.18 The transformer's response to (a) AC electric signal and (b) AC magnetic signal. 152

Fig. 6.19 The coupled effect of the AC magnetic input signal and the AC electric input signal on the output electric signal. (a) The output signal driven by AC magnetic input signal, (b) the output signal driven by AC electric input signal and (c) the output signal driven by coupled AC magnetic and AC electric input signals. 154



LIST OF TABLE CAPTIONS

Table 1-1 Saturation magnetostriction of some representative magnetic phases in ME composites at room temperature.	13
Table 1-2 Longitudinal and transverse piezoelectric strain constant (d_{33} and d_{31}) of some representative piezoelectric phase in ME composites at room temperature.....	14
Table 5-1 Resistivity of typical components in ME composites.....	109
Table 6-1 Piezoelectric property of x CFO - (1 - x)PZT502 composites. ($x = 0.15, 0.30$ and 0.45).....	144



CHAPTER 1

Introduction

1.1 Introduction to magnetoelectric materials

Magnetoelectric (ME) materials are featured with electrical polarization in the presence of external magnetic field and magnetization in the presence of external electric field, i.e., the magnetoelectric (ME) effect. These magnetoelectric materials provide potentials in various technological applications including magnetic field sensors, transformers, gyrators, oscillators, filters, phase shifters and so on. The study of magnetoelectricity also remains one active area in solid state physics and materials science for decades [1 - 4].

1.1.1 Early history of ME coupling

The ME effect was first discovered in 1888 by Rontgen, who found that a moving dielectric became magnetized when placed in an electric field [5]. And later in 1905, the converse effect, i.e., the polarization of a moving dielectric in a magnetic field, was observed [6]. The first theoretical statement about the interaction between magnetic field and electric field was made by Curie in 1894 who pointed out the possibility for an asymmetric molecular body to polarize directionally under the influence of a magnetic field [7]. Curie stated that there should be materials whose magnetism is induced by electric field (i.e., $M_\alpha = G_{\beta\alpha}E_\beta$) and whose polarization by



magnetic field (i.e., $P_\beta = G_{\alpha\beta}B_\alpha$). Then Landau and Lifshitz [8] stated that a linear ME can occur in magnetically ordered crystals based on symmetry considerations. Subsequently, Dzyaloshinskii [9] predicted the existence of the ME effect in anti-ferromagnetic Cr_2O_3 on the basis of theoretical analysis. This prediction was further confirmed by Astrov [10] through measuring the electric field induced magnetization (see Fig. 1.1 (a)) and later by Rado and Folen [11] through detection of the magnetic field-induced polarization (see Fig. 1.1 (b)).

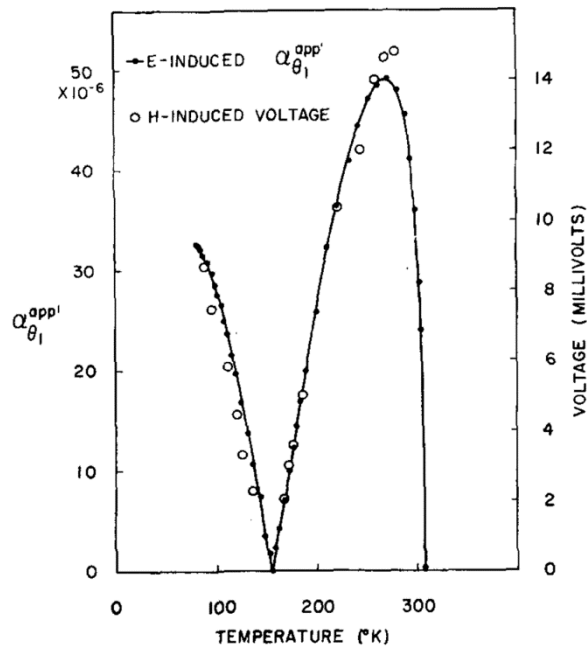


Fig. 1.1 Temperature dependence of the magnetolectricity in Cr_2O_3 [11].

1.1.2 ME material development

After its first observation in Cr_2O_3 , magnetolectricity has been found to exist in tens of natural and man-made compounds, such as Ti_2O_3 [12], GaFeO_3 [13], several



boracite [14] and phosphate [15] compounds, solid solutions like $\text{PbFe}_{0.5}\text{Nb}_{0.5}\text{O}_3$ [16] and garnet films [17, 18], and tens of other compounds [19]. These single phase materials show two transitions: one from ferroelectric to paraelectric state and the other from ferromagnetic/ferrimagnetic/antiferromagnetic to paramagnetic state. ME effect in these compounds arises from the local interaction between the ordered magnetic and ferroelectric sub-lattices. Currently these single phase materials can be summarized into four major crystallographic types: compounds with perovskite structure (represented by $\text{PbFe}_{1/2}\text{Nb}_{1/2}\text{O}_3$, BiFeO_3) [20 - 23], compounds with hexagonal structure (represented by hexagonal manganites, i.e., RMnO_3 with $\text{R} = \text{Sc, Y, In, Ho, Er, Tm, Yb, Lu}$) [24 - 27], Boracites ($\text{M}_3\text{B}_7\text{O}_{13}\text{X}$, with $\text{M} = \text{Cr, Mn, Fe, Co, Cu, Ni}$ and $\text{X} = \text{Cl, Br, I}$) [28, 29] and BaMF_4 compounds ($\text{M} = \text{Mg, Mn, Fe, Co, Ni, Zn}$) [30, 31].

Figures 1.2 and 1.3 give the lattice structure of BiFeO_3 and HoMoO_3 with/without an electric field. In their structures, the electric field induces reordering of its antiferromagnetic lattice and ferromagnetic lattice. The function of the electric field is not only to transform the sample into a single-domain ferroelectric state and generate a saturated macroscopic polarization P . For this purpose the electric field is best applied close to room temperature since at low temperature the ferroelectric polarization reversal is difficult to achieve. During cooling, the electric field can be removed once the single-domain state is stable at zero fields. The polarization interacts with the induced magnetization M of the lattice and lowers the free energy via the magnetoelectric contribution.

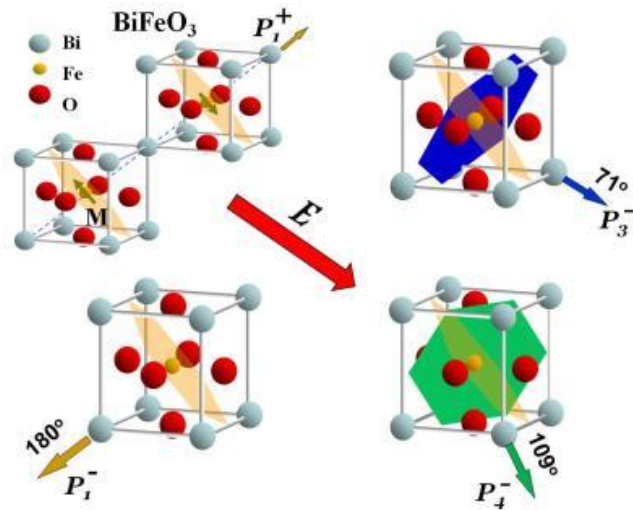


Fig. 1.2 Lattice structure of perovskite BiFeO_3 in the absence ($E = 0$) or presence ($E \neq 0$) of an electric field.

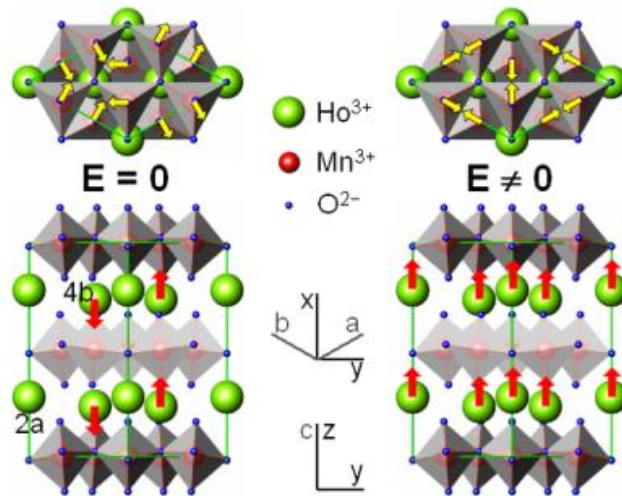


Fig. 1.3 Lattice structure of hexagonal HoMnO_3 in the absence ($E = 0$) or presence ($E \neq 0$) of an electric field.

Although extensive study has been made, single-phase multiferroic materials are not ready for application due to several limitations:



(1) The realizable magnitude of the magnetoelectric voltage coefficient in the single phase material is of the order of $\sim 1 - 20$ mV/cm Oe, which is not sufficient for practical applications. The reason as proposed by Brown *et al* in 1974 is that the magnetoelectric effect in single phase materials cannot be larger than the geometric mean of electric and magnetic permeability. That is,

$$\alpha_{ij}^2 < \chi_{ii}^e \chi_{jj}^m \quad (1-1)$$

where α_{ij} is the coupling coefficient, χ_{ii}^e is the electric permeability and χ_{jj}^m is the magnetic permeability.

(2) The working range of temperature is limited for these materials. Most of the single phase materials can be used only at very low temperatures.

(3) Many of the materials are expensive and suffer from degradation under cyclic conditions. The processing technique is also expensive.

The solution to these limitations is offered by shifting to composite materials, which provide greater design flexibility and larger coupling coefficient. In Section 1.2, a detailed introduction is given to the magnetoelectric composites.

1.2 Magnetoelectric composites

Magnetoelectric (ME) composites are multi-component material systems typically made by combining piezoelectric and magnetic substances together. The coupl-



ing interaction between piezoelectric and magnetic substances could produce a large ME response (several orders of magnitude higher than that in those single phase ME materials) at room temperature. With large multi-functionality, these ME composites have drawn significant interest in recent years and provide opportunities for potential applications as multifunctional devices such as magnetoelectric transducers, actuators, and sensors.

1.2.1 Origin of magnetoelectricity in composites

The ME effect in composites is realized by using the concept of product properties introduced by Van Suchetelene [32] in 1972. According to this concept, a suitable combination of two phases can yield the desirable property. For example, a combination of piezomagnetic and piezoelectric phases, or a combination of magnetostrictive and piezoelectric phases, can yield the magnetoelectric effect. The ME effect can also be realized by coupling the thermal interaction in pyroelectric-pyromagnetic composites.

The most investigated ME composites are made of ferroelectric and ferromagnetic phases (Fig. 1.4), in which ME effects arise from the cross interaction between different orderings in the composites, i.e., the magnetostrictive effect (magnetic/mechanical effect) in the magnetic phase and the piezoelectric effect (mechanical/electrical effect) in the piezoelectric one [32 - 34].

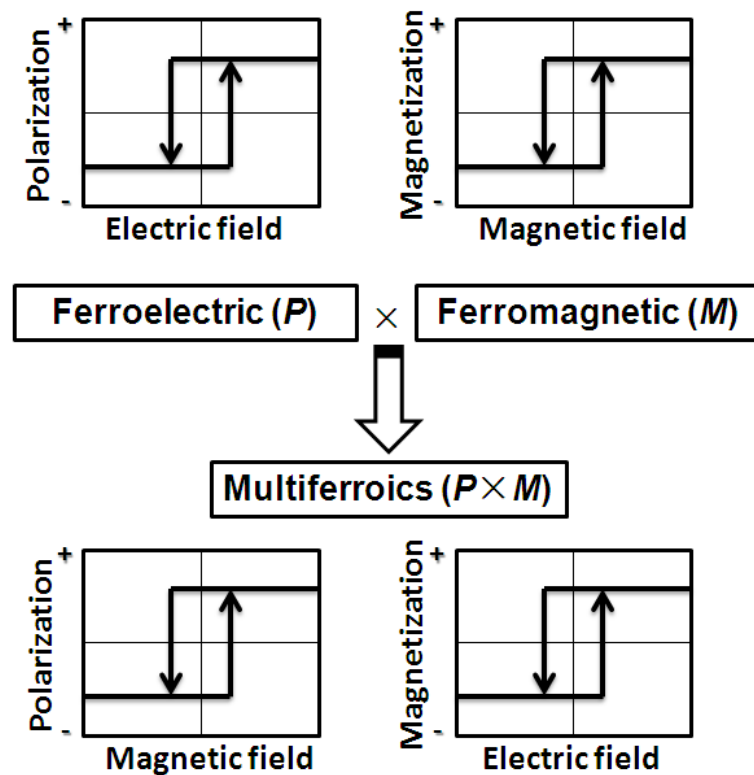


Fig. 1.4 Illustration of the magnetoelectric effect in ferroelectric - ferromagnetic composites.

The coupling between the electric and magnetic components is achieved via the elastic interaction at the phase boundary. That is, for the ME_H effect, when a magnetic field is applied to a composite, the magnetic phase changes its shape magnetostrictively. The strain is then passed along to the piezoelectric phase, resulting in an electric polarization. Therefore, the ME effect in composites is an extrinsic effect, of which the magnitude is largely dependent on the composite microstructure and coupling interaction across the magnetic-piezoelectric interfaces. To express this process quantitatively, if an input magnetic field (H) is applied to this composite material, we may have:



$$\frac{\partial S}{\partial H} = e^m \quad (1-2)$$

for the magnetic phase, and

$$\frac{\partial E}{\partial S} = e \quad (1-3)$$

for the piezoelectric phase, where S is the strain and e^m and e are, respectively, piezomagnetic and piezoelectric coefficients. As a result, this two-phase composite material can be characterized by:

$$\alpha = \frac{\partial P}{\partial H} = \frac{\partial P}{\partial S} \times \frac{\partial S}{\partial H} = k_c e^m e \quad (1-4)$$

where k_c is a coupling factor ($0 \leq |k_c| \leq 1$) between the two phases, and α is the ME coefficient of the composite. Thus, a new property (i.e., a nonzero ME coefficient) appears in the composite consisting of magnetic and piezoelectric phases, since neither constituent phase is magnetoelectric. This new ME product response is due to elastic coupling between the two constituent phases. High piezomagnetic/piezoelectric coefficients and strong coupling with large k_c favor a large ME coefficient. [1, 33, 35]



1.2.2 Features of magnetoelectricity in composites

Compared with the ME effects in single-phase materials, ME effects in composites show two distinguished features. They are :

(1) Nonlinearity. Most ferromagnetic materials show the magnetostrictive effect, however, piezomagnetic effect in these materials has not been observed. This means that the strain caused by a magnetic field in these materials is not linearly proportional to the field strength but is related to the square of the magnetic field strength. This makes the product property, the magnetoelectric effect in the piezoelectric-magnetostrictive composites, a non-linear effect. As a contrast, the ME effect in single phase materials is a linear effect over a wide range of the magnetic or electric field.

(2) Hysteretic behavior. Fig. 1.5 shows an example of the hysteretic magnetoelectric effect in a PZT/LSMO laminated composite, in which one can find the hysteresis loop highly sensitive to the volume fractions of the components. The hysteresis behavior of ME composites makes it difficult for them to apply in linear devices.

To achieve the linearity in such composites, a bias magnetic field is applied across them, i.e., by DC biasing the magnetostrictive phase to an effective piezomagnetic state, so that the magnetoelectric effect over a short range around this bias can be approximated as a linear effect. The hysteretic nature of this effect can be deployed in memory devices, for which there is no need for a bias magnetic field.

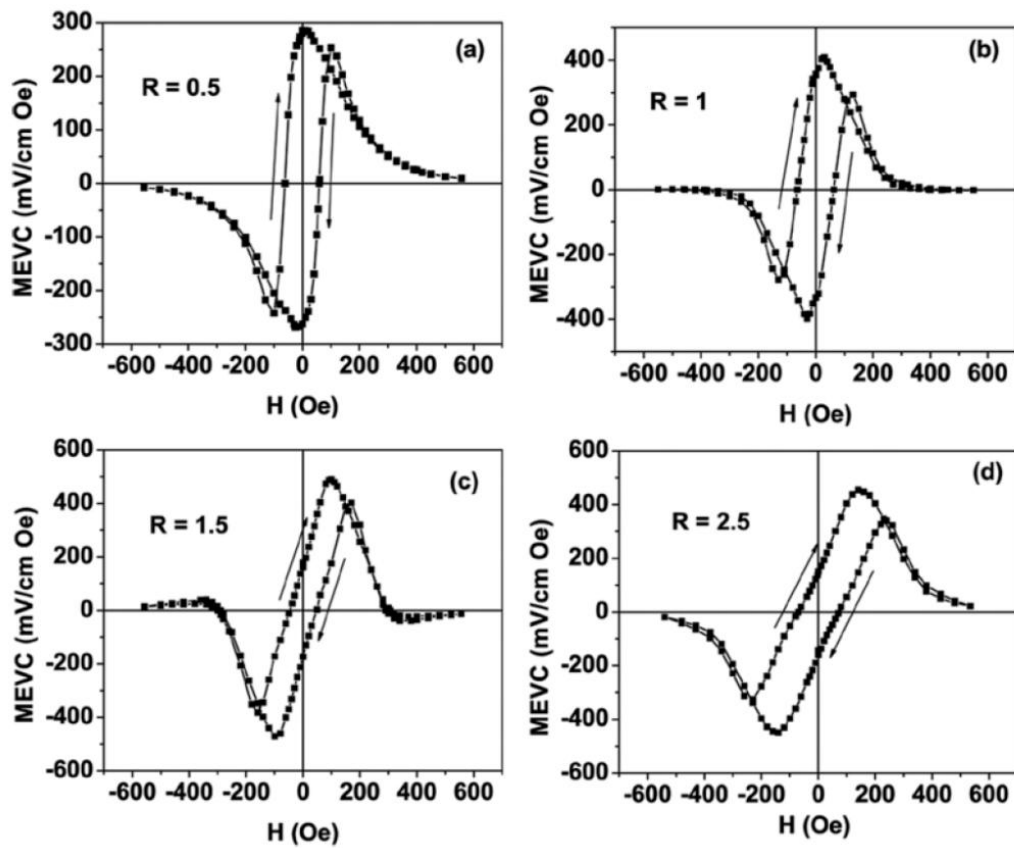


Fig. 1.5 Magnetoelectric hysteresis curve showing the magnetic response of the PZT - NZFO - Ni bilayer system as a function of the applied electric field. The factor R in figures (a) to (d) stands for the ferrite-to-Ni thickness ratio. MEVC stands for the magnetoelectric voltage coefficient. [36]

1.2.3 Linear approximation of magnetolectricity in composites

The constitutive equation for describing coupled mechanical-electric-magnetic response in ME composites to linear approximation can be written by direct notation for tensors as:



$$\begin{aligned}\sigma &= \mathbf{c}S - \mathbf{e}^T E - \mathbf{q}^T H, \\ D &= \mathbf{e}S + \boldsymbol{\varepsilon}E + \boldsymbol{\alpha}H, \\ B &= \mathbf{q}S + \boldsymbol{\alpha}^T E + \boldsymbol{\mu}H,\end{aligned}\tag{1-5}$$

where σ , S , D , E , B , and H are the stress, strain, electric displacement, electric field, magnetic induction, and magnetic field, respectively; \mathbf{c} , $\boldsymbol{\varepsilon}$, and $\boldsymbol{\mu}$ are, respectively, the stiffness, dielectric constant, and permeability; \mathbf{e} and \mathbf{q} are the piezoelectric and piezomagnetic coefficients, respectively; $\boldsymbol{\alpha}$ is the ME coefficient. The superscript T means the transpose of the tensor. The tensors \mathbf{c} , \mathbf{e} , \mathbf{q} , $\boldsymbol{\varepsilon}$, $\boldsymbol{\mu}$ and $\boldsymbol{\alpha}$ are (6×6), (3×6), (3×6), (3×3), (3×3) and (3×3) matrices, respectively, by means of the compressive representation. For the piezoelectric phase (e.g., BaTiO₃ and PZT) in the composites, $\mathbf{q} = 0$ and $\boldsymbol{\alpha} = 0$; while for the magnetic phase (e.g., Co ferrites and Ni ferrites) in the composites, $\mathbf{e} = 0$ and $\boldsymbol{\alpha} = 0$. For their composites, however, the effective ME coefficient $\boldsymbol{\alpha} \neq 0$, which depends on details of the composite microstructures, i.e., component phase properties, volume fraction, grain shape, phase connectivity, etc.

1.2.4 Magnetolectric composite systems

A large ME effect was produced in composites experimentally soon after the product ME property in the composite combining magnetostrictive and piezoelectric phases was proposed. The first artificial magnetolectric composite was grown by van Suchtelen *et al* by combining ferroelectric piezoelectric BaTiO₃ and ferromag-



netic piezomagnetic CoFe_2O_4 in an eutectic composite (quinary Fe - Co - Ti - Ba - O system) by unidirectional solidification. [37 - 40] The microstructure of this composite is given in Fig. 1.6. Depending on the growth conditions, the magnetoelectric voltage coefficient obtained with this method reached as high as $\delta E/\delta H = 0.13$ V/cm·Oe at room temperature, which exceeds the largest values observed in single-phase compounds by more than an order of magnitude. [3]

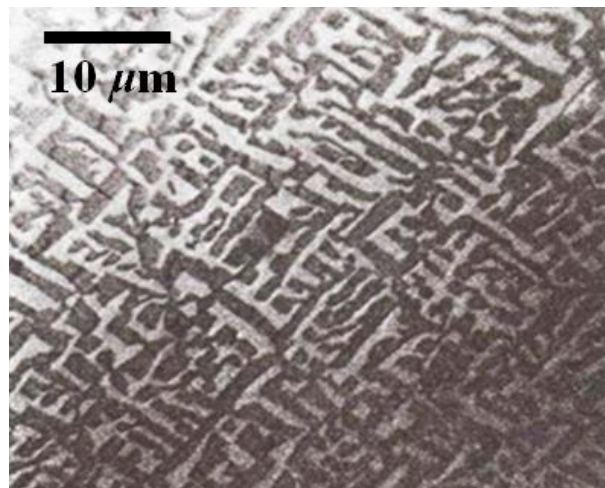


Fig. 1.6 Microstructure of the first ME composite by Suchtelen [36]. Samples were fabricated by unidirectional solidification of an eutectic composition of the quinary system Fe - Co - Ti - Ba - O.

The composite ME effect is an addition to the class of ME coupling phenomena. Many new parameters can be tuned in order to optimize the ME response, such as the stoichiometry and microstructure of the composite. Subsequent to the pioneering experiment on $\text{BaTiO}_3/\text{CoFe}_2\text{O}_4$, a variety of titanate/ferrite compositions were investigated [41 - 49]. A material that combines a large piezoelectric constant and com-



mercial availability is $\text{Pb}(\text{Zr}_x\text{Ti}_{1-x})\text{O}_3$ (PZT) [3], whereas aside from ferrites, $\text{Tb}_{1-x}\text{Dy}_x\text{Fe}_2$ alloys (Terfenol-D) also display superior magnetostrictive behavior [50]. Therefore PZT/ferrite and PZT/Terfenol-D represent the most frequently studied composites thus far [3, 51 - 63], although materials with higher piezoelectric coefficients do exist [64, 65]. Further, experiments on many doped titanate/ferrite composites like $\text{Ba}_{0.8}\text{Pb}_{0.2}\text{TiO}_3/\text{CuFe}_{1.8}\text{Cr}_{0.2}\text{O}_4$ [66] were reported. Other piezoelectric constituents include $\text{Bi}_4\text{Ti}_3\text{O}_{12}$ [3], polyvinylidene fluoride (PVDF) [67], $\text{Pb}(\text{Mg}_{1/3}\text{V}_{2/3})\text{O}_3$ [68] and $\text{PbX}_{1/3}\text{Nb}_{2/3}\text{O}_3 - \text{PbTiO}_3$ ($X = \text{Mg, Zn}$) [3, 69]. As alternative magnetostrictive ingredient manganites [49, 70], LiFe_5O_8 [3], YIG [71] and Permendur [72] have been studied as well.

Table 1-1 Saturation magnetostriction of some representative magnetic phases in ME composites at room temperature.

Material	Terfenol-D	CoFe_2O_4	NiFe_2O_4	MnFe_2O_4	CuFe_2O_4	LiFe_5O_8
$\lambda_s (\times 10^{-6})$	1080	-110	-26	-5	-9	-8

Table 1-1 provides a list of the frequently used magnetostrictive materials in ME composites. [73 - 75] High magnetostrictive coefficients are obtained in the binary compound $\text{Tb}_{0.3}\text{Dy}_{0.7}\text{Fe}_{1.9-1.95}$ commercially known as Terfenol-D, which has the highest room-temperature magnetostriction. Terfenol-D is widely employed as the magnetostrictive material in several important applications including active noise and vibration control systems, low frequency under-water communications (sonar), linear and rotational motors, ultrasonic cleaning and so on. This material also has importance as the magnetostrictive phase in ME laminated composites.



Table 1-2 Longitudinal and transverse piezoelectric strain constant (d_{33} and d_{31}) of some representative piezoelectric phase in ME composites at room temperature.

Material	d_{33} (pC/N)	d_{31} (pC/N)
BaTiO ₃	190	- 78
APC 850 (soft PZT)	400	-175
APC 855 (soft PZT)	630	-276
APC 840 (hard PZT)	290	-125
PZT - Pb(Ni _{1/3} Nb _{2/3})O ₃	600	-250
0.92 Pb(Zn _{1/3} Nb _{2/3})O ₃ - 0.08PbTiO ₃ (<001>)	2230	-1080
PVDF	-33	23

The choice for the piezoelectric material in magnetoelectric composites is also diverse including ceramics, single crystals, and polymers as shown in Table 1-2. [76 - 79] The compound Pb(Zr_xTi_{1-x})O₃ (PZT) is commonly used as the piezoelectric material due to its availability, low costs and convenience to process. Also, some relaxor ferroelectric single crystal material, such as PZN - PT listed in Table 1-2, provides considerably high piezoelectric performance but suffers from their low transition temperatures, high nonlinearity, and large temperature and vibration sensitivities at the same time. Besides, piezoelectric polymers, like PVDF (polyvinylidene fluoride), [80] can also be used for the piezoelectric phase. In the preparation of the



magnetolectric composites, selection of both magnetic and piezoelectric components depend on the fabrication technique including ceramic processing, hot-pressing, lamination, co-firing and so on.

1.2.5 Potential applications of ME materials

The possible applications of the ME materials have been reviewed by Wood and Austin. [81] They proposed 15 types of applications of ME materials and discussed devices for (i) modulation of amplitudes, polarizations and phases of optical waves, (ii) ME data storage and switching, (iii) optical diodes, (iv) spin-wave generation, (v) amplification and (vi) frequency conversion. The prospect of these applications is more promising after researchers found that composite ME effects can exceed the intrinsic ME effect in single-phase compounds by many orders of magnitude.

Based on the aspect that the composite ME effect is a dynamic effect: a pronounced linear ME response is only observed for an AC field oscillating in the presence of a stronger DC bias field, composite ME effect is predetermined for microwave applications. Different frequency ranges are accessed by using the enhancement from the electromechanical resonance (~ 100 kHz), the ferromagnetic resonance (~ 10 GHz) or the antiferromagnetic resonance (~ 100 GHz) [82]. At resonance frequencies, a ME composite can be used as a transducer which converts the microwave magnetic field into a microwave electric field. Because of the shift in the resonance frequency in a static magnetic or electric bias field the composite materials can be employed as phase shifters or attenuators. For this type of applications, the field-induced shift in the resonance frequency must be at least of the order of magni-



tude of the resonance line width. For example, for PZT/NiFe₂O₄, an electric field of 300 kV/cm is required for obtaining a line shift of 330 Oe for a resonance line width of 450 Oe [82].

Because of the hysteretic nature of the ME effect, ME composites may find applications in memory devices. The linear ME effect has a positive or a negative sign, depending on the annealing conditions (parallel or anti-parallel magnetic and electric fields). In binary data storage devices, the ME material can thus store information in two different states distinguished by the sign of the ME response. Such a memory will be an effective read-only memory, since the reading can be done at very high frequencies. Data writing is more difficult because it involves temperature annealing in magnetic and electric fields or the use of very high writing fields [3].

Further applications include magnetic field sensors (thus complementing Hall sensors and current measurement probes). Since the magnetic field input is required to have two components, a DC bias and an AC probe, either of the two can be detected by providing the other component. The ME composite can thus be used as a magnetic probe for detecting AC or DC fields. The transduction properties of the ME effect can also be employed in ME recording heads and electromagnetic pick-ups [3].

1.3 0 - 3 type magnetoelectric composites

According to the connectivity schemes between the two component phases, most magnetoelectric composites can be commonly divided into three major categories (see Fig. 1.7): (i) 0 - 3 type particulate composites which are mostly in the state of bulk ceramic, (ii) 2 - 2 type laminated composites which can be bulk ceramics [83



- 88] or heterostructures [89 - 93], and (iii) 1 - 3 type composites with fibers/rods of one phase embedded in the matrix of another phase [94 - 96].

Among these composite structures, the ferromagnetic/piezoelectric 0 - 3 composite ceramics have attracted much research interest mainly because their fabrication procedures are compatible with conventional ceramic processing process, thus can be produced at low cost in large quantities easily. Many 0 - 3 type composites have been developed such as $\text{LaFeO}_3/\text{PbTiO}_3$, $\text{PZT}/\text{NiFeMnO}$, CFO/PZT , $(\text{Ni}_{0.5}\text{Zn}_{0.5})\text{Fe}_2\text{O}_4/\text{BaTiO}_3$, $\text{Ni}_{0.2}\text{Co}_{0.8}\text{Fe}_2\text{O}_4/\text{PbZr}_{0.8}\text{Ti}_{0.2}\text{O}_3$, $\text{Sr}_{0.5}\text{Ba}_{0.5}\text{Nb}_2\text{O}_6/\text{CoFe}_2\text{O}_4$, $[\text{Pb}(\text{Ni}_{1/3}\text{Nb}_{2/3})\text{O}_3 - \text{PbTiO}_3]/[(\text{Ni}_{0.2}\text{Cu}_{0.2}\text{Zn}_{0.6})\text{Fe}_2\text{O}_4]$, $\text{Ni}_{0.2}\text{Co}_{0.8}\text{Fe}_2\text{O}_4/\text{PbZr}_{0.8}\text{Ti}_{0.2}\text{O}_3$, $\text{Co}_{0.9}\text{Cd}_{0.1}\text{Fe}_2\text{O}_4/\text{PZT}$, and $\text{PZT} - \text{NCZF}$. [97 - 108]

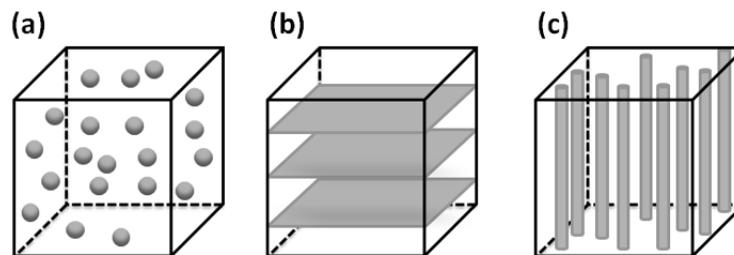


Fig. 1.7 Schematic illustration of three bulk composites with the three common connectivity schemes. (a) 0 - 3 particulate composite, (b) 2 - 2 laminate composite and (c) 1 - 3 fiber/rod composite.

1.3.1 A short introduction to 0 - 3 type particulate composites

As mentioned in Section 1.2.2, the first work on ME composites was done at



Philips Laboratories in the Netherlands. The particulate ME composites were prepared by unidirectional solidification of a eutectic composition of the quinary system Fe - Co - Ti - Ba - O. [36 - 39] Unidirectional solidification helps in the decomposition of the eutectic liquid into alternate layers of a piezoelectric perovskite phase and a piezomagnetic spinel phase. For example, their results showed that excess of TiO_2 by 1.5 wt % gives a high ME voltage coefficient ($\alpha_E = 50 \text{ mV/cm Oe}$). However, other compositions showed a lower α_E of 1 - 4 mV/cm Oe only. In a subsequent work, a high ME coefficient of 130 mV/cm Oe was obtained in a eutectic composition of BaTiO_3 - CoFe_2O_4 by unidirectional solidification. However, this method is complex and requires critical control over the composition.

In comparison, sintered composites are easier and cheaper to fabricate with several advantages such as freedoms in the selection of constituent phases, their starting particle sizes, and the sintering temperatures. Furthermore, sintering does not require the presence of eutectic or eutectoid transformations, and also provides the opportunity to combine phases with widely different crystal structures.

In the past two decades, various particulate composites consisting of piezoelectric and magnetostrictive materials with 0 - 3 connectivity have been prepared using the traditional sintering method. In a common preparation process for such ceramic composites, the powders of piezoelectric ceramics and magnetic oxides (mostly ferrites) are firstly mixed together, and then the mixed powders are pressed into green bulks followed by sintering at high temperature.

Accordingly, there are some primary requirement to prepare this kind of composites using the sintering route, including: (1) individual phases should be in equili-



brium, (2) mismatch between grains should not be present, (3) large magnetostriction and piezoelectric effects in the respective constituent phases, (4) high dielectric insulation so that accumulated charge does not leak through the composite, and (5) the ability to pole the piezoelectric phase in the composite.

At low frequencies and under DC bias fields, the magnitude of the ME coefficient from the bulk sintered composites was in the order of 10 - 100 mV/cm Oe. Hot-pressed samples exhibited an order of magnitude improvement in the ME voltage coefficient, as compared to the sintered samples [27]. Some typical experimental results are stated in Section 1.3.2.

1.3.2 Typical experimental results of 0 - 3 particulate ME ceramics

Ryu *et al* have investigated the effect of sintering temperature on the sintering behaviors, microstructures, piezoelectric, and ME properties of particulate composites constituting Ni-ferrite doped with Co, Cu, Mn particles in a PZT matrix [51, 52]. It was found that not only the connectivity of the ferrite phase, but also the sintering temperature are important parameters for higher ME voltage coefficient dE/dH . The chemical reaction of PZT with ferrite, and connection of ferrite particles makes it difficult to get high ME effects. Fig. 1.8 shows the maximum ME voltage coefficient of various composition as a function of sintering temperature [52]. They obtained the highest ME voltage coefficient (115 mV/cm Oe) from the composite with 20 % of ferrite added and sintered at 1250 °C. These excellent results were attributed to homogeneous and well dispersed microstructure, no chemical reaction between the two phases, and large grain size of the matrix PZT phase. [109]



The low-frequency ME coefficients of the sintered 0 - 3 composite ceramics is in the range of 10 to 100 mV/cm·Oe in the literature, while this value can be enlarged to as much as \sim V/cm·Oe at resonance frequency. For example, Petrov *et al* studied the frequency dependence of the ME coupling. [110, 111] The bias field was set at a constant value and the ME voltage coefficients were measured as the frequency (f) of the AC field was varied. Typical $\alpha_E - f$ profiles are shown in Fig. 1.9. In the figure, for the sample with porosity = 5 %, upon increasing f , $\alpha_{E,31}$ remains small and constant for f up to 250 kHz. At higher f , one notices a rapid increase in $\alpha_{E,31}$ to a peak value of 9 V/cm·Oe at 350 kHz. The peak value of $\alpha_{E,31}$ is a factor of 100 higher than the 1 kHz value and then it levels off at a much lower value. A similar resonance in α_E was also observed for longitudinal fields, which is not shown here. In this study it was also found that the increase in the magnitude of ME coefficient at resonance is much higher in the sintered samples as compared to the laminated composites.

Magnetic field is also a factor affecting the magnetoelectric effect, which has been widely studied. In Petrov's work, for example, the bias magnetic field H dependence of $\alpha_{E,33}$ was studied[111]. In Fig. 1.10, for samples with $p = 5$ %, one observes a general increase in $\alpha_{E,33}$ with H to a peak value, followed by a rapid drop.

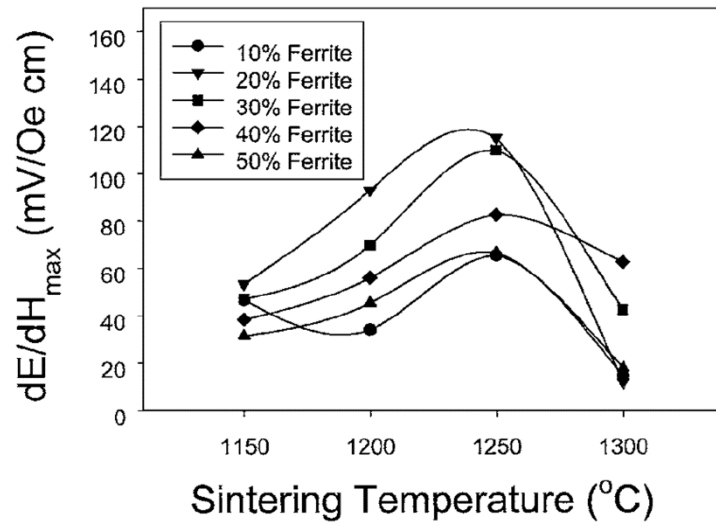


Fig. 1.8 Maximum ME voltage coefficient of the PZT and Ni-ferrite particulate composites as functions of sintering temperature and Ni-ferrite particle contents.

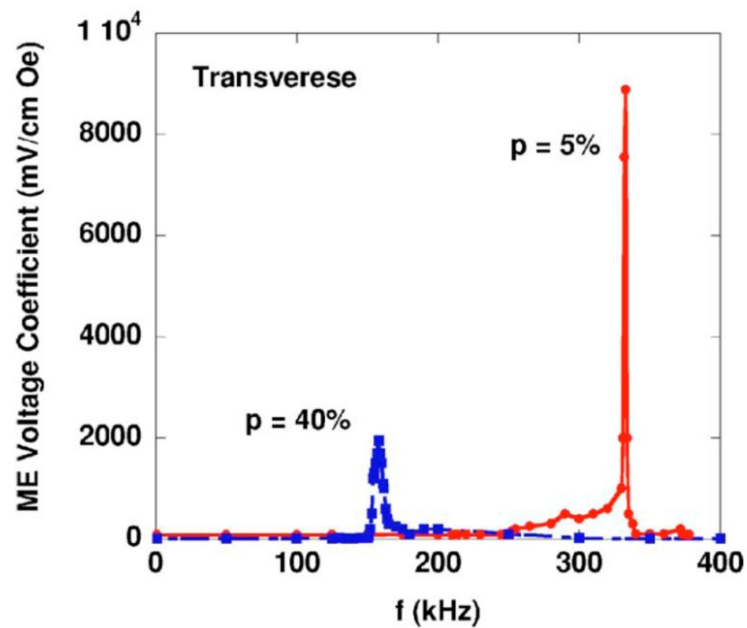


Fig. 1.9 Frequency dependence of transverse ME coefficient for samples with 5 % and 40 % porosity. [111]



The influence of microstructure such as porosity was also studied in Ref. [111]. In Figs 1.9 and 1.10, the p value stands for the porosity, which is obtained by varying the applied pressure to the sample over a wide range from 700 kPa to 200 MPa (corresponding to porosity $p = 5\% - 40\%$). It was found that compared to the sample with $p = 5\%$, the sample with $p = 40\%$ exhibited quite small peak value at a much lower frequency in the $\alpha_{E,31} - f$ relationship and a much lower magnetic bias in the in the $\alpha_{E,33} - H$ relationship.

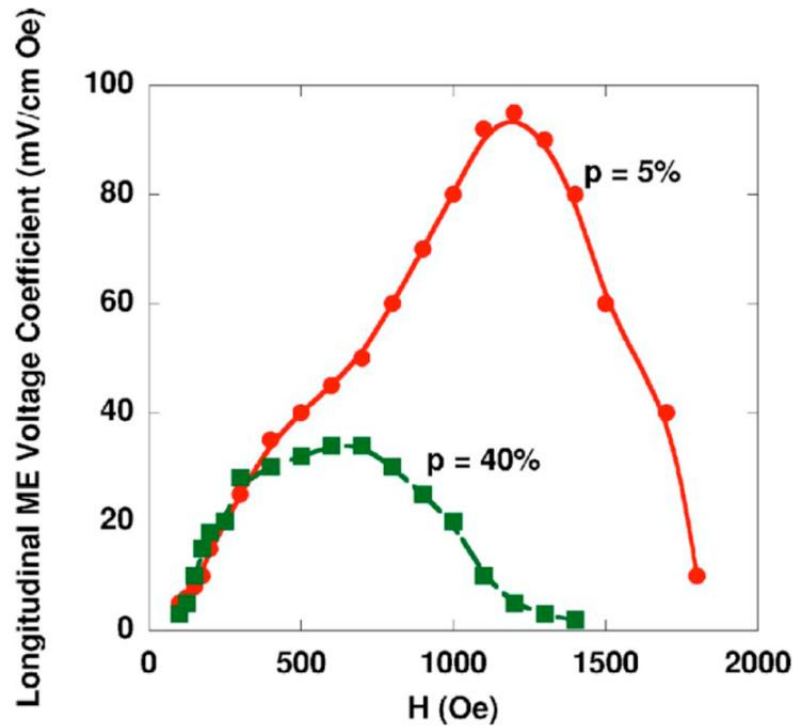


Fig. 1.10 Static magnetic field H dependence of the longitudinal ME coefficient $\alpha_{E,33}$ for bulk composites of nickel ferrite and lead zirconate titanate (PZT). The data at room temperature and 1 kHz are for samples with porosity $p = 5\%$ and 40% . [111]

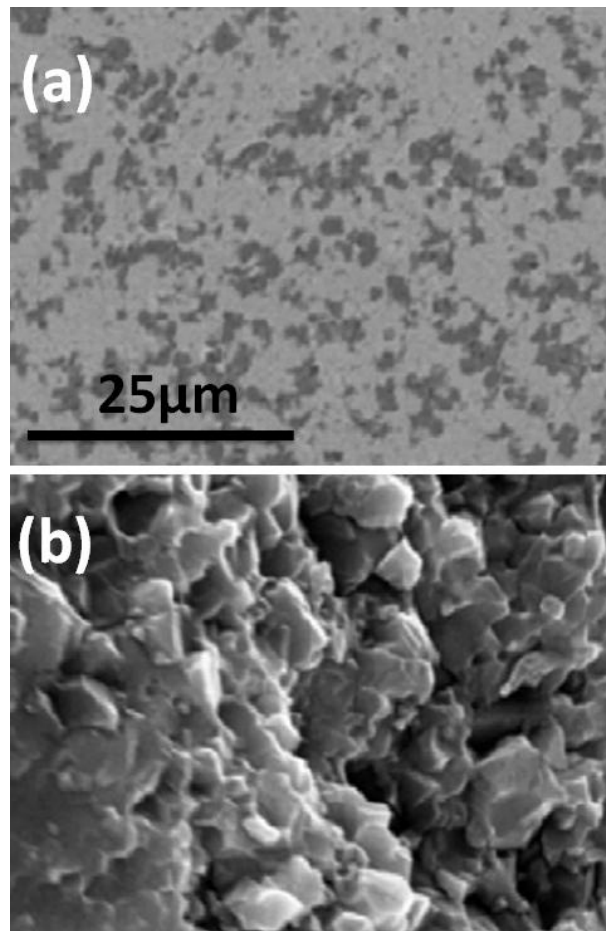


Fig. 1.11 Scanning electron microscopy images of the NFO - PZT composite ceramics via SPS. (a) Polished surface and (b) fractured surface

Apart from the traditional sintering method, some other techniques including hot pressing [112] and spark plasma sintering [113] (SPS) were developed in order to achieve sufficient bulk density while avoid possible reactions between the constituent phases to occur. Hot-pressed and SPS samples exhibited a large improvement in the ME voltage coefficient, as compared to the conventionally sintered samples. SPS offers an efficient sintering that allows rapid consolidation (e.g., 5 min) at comparatively low temperatures, [114] which is considered an efficient process to fabricate composites with high density and prevent unwanted reaction to occur. For example,



dense composite NFO - PZT ceramics with relative density of 99 % have recently been prepared by SPS consolidation of mechanically mixed powder mixtures. [113] Also, the composite ceramics via SPS is shown to lead to fine microstructure and an obvious improvement in the ME voltage coefficient. The composite ceramics via SPS exhibit fine microstructure (Fig. 1.11), and the SPS condition has an essential influence on the ME properties. In comparison to the conventional sintering, SPS leads to an obvious improvement in the ME voltage coefficient, as shown in Fig. 1.12, though the grain size in the ceramics via SPS is much smaller than those via conventional sintering.

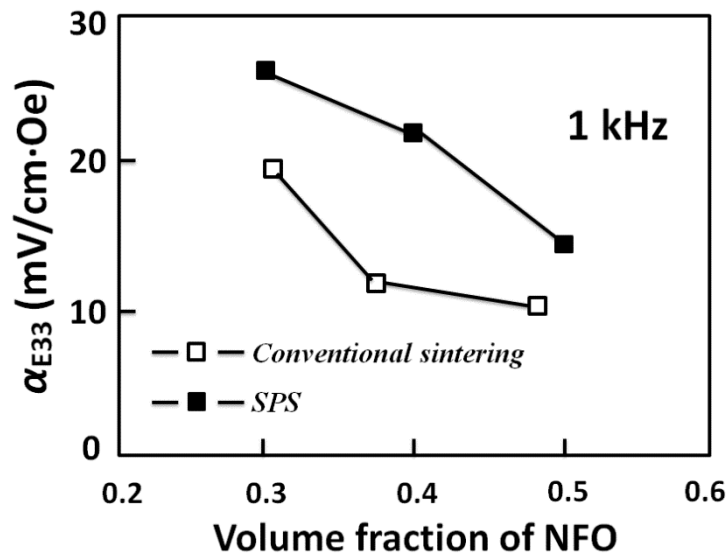


Fig. 1.12 Comparison of the ME coefficients of the 0 - 3 type NFO - PZT ceramic composites via SPS and conventional sintering.

There is also much work about the relationship between the composite's proper-



ties and the content of the component phase. A series of studies on the dielectric and magnetoelectric properties of several composites as a function of relative phase content have been reported by Patankar and co-workers, including: NiCo [45, 115], Cu [116], CuCr [117] and CuCo [43] ferrite - $\text{Ba}_{0.8}\text{Pb}_{0.2}\text{TiO}_3$ composites; and MnCr [118], Cu [119] and CuCr [120] ferrite - BaTiO_3 composites. In most cases, the maximum static magnetoelectric coupling coefficient is found for ferroelectric contents between 70 - 85 %, with maximum values in the range of 0.1 - 0.5 mV/cm·Oe at an optimum magnetic field in the range of 0.5 - 2 kOe. The small load of the magnetic phase in the composites suggests that leakage may be an important limiting factor for the magnetoelectric property. The role of conductivity in the ferrites in reducing α_E was demonstrated by Srinivasan *et al* [121] in NiFe_2O_4 - PZT composites, where substitution of 2 % of the Fe with Co leads to a sharp increase in resistivity by six orders of magnitude and a concomitant increase in α_E by nearly a factor of 10. Besides, analysis of the conductivity response of these sintered composites suggests that conduction takes place via polaron hopping at high temperatures and via impurities or defects at low temperatures. [45, 117, 119]

In order to achieve good dispersion of a high concentration of ferrite particles in the composite ceramics, wet-chemical processing (e.g., sol - gel method) has also been employed to in situ synthesize the homogeneously mixed composite powders of the piezoelectric and ferrite oxides. [122 - 125] For example, Ren *et al* [122] used a one-pot method, which added cobalt ferrite nanoparticles obtained by coprecipitation into the precursor gel of BTO, to allow the in-situ formation of ferrite - BTO composite. The one-pot synthesized samples showed a piezoelectric d_{33} constant approximately six times larger and a ME voltage coefficient approximately three times



larger than the corresponding mechanically milled samples. This high property was attributed to improved distribution of CoFe_2O_4 phase in the BaTiO_3 matrix (see Fig. 1.13), which restricted the contact of the ferrite particles during sintering.

The converse ME effect has been measured less often in these composite structures. One instance has been reported in a BaTiO_3 - LaMnO_3 ceramic composite, [126] where a large change in the saturation magnetization is observed as a function of the applied electric field. The presence of magnetism is attributed to the formation of $(\text{La}, \text{Ba})\text{MnO}_3$ at sintering temperatures near $1100\text{ }^\circ\text{C}$, and the modifications in the magnetization are attributed to strain and to the sensitivity of the colossal magnetoresistance (CMR) manganites to strain, giving $\alpha = 3.4 \times 10^{-4}\text{ Oe}\cdot\text{cm}/\text{V}$ at room temperature.

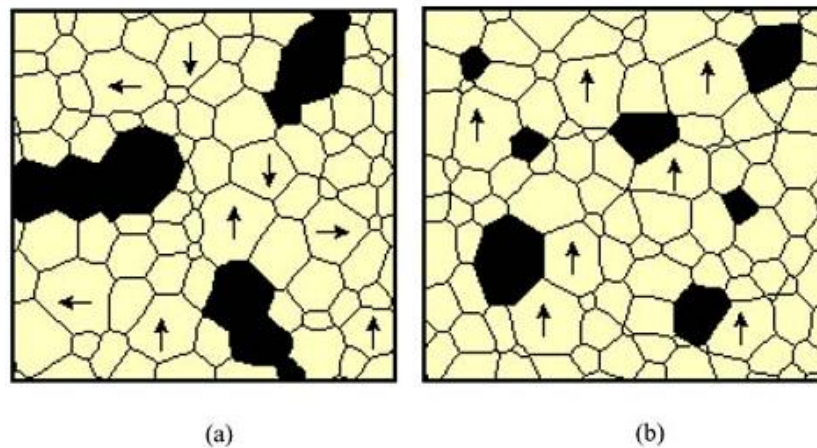


Fig. 1.13 Schematic diagrams of distribution of CoFe_2O_4 phase (in black) in BaTiO_3 matrix in two different ways. (a) Composite materials prepared by mixing and sintering method and (b) composite materials produced by one-pot approach. [115]



1.3.3 Theories of 0 - 3 type particulate ME ceramics

Theoretical models are available in the literature to account for the large ME effect of composites [38, 127, 128]. In the past, studies on ME composites have concentrated on estimation of the effective properties of the composite as a function of microstructural variables such as physical properties of individual phases, volume fraction, shape and connectivity. These models have their own advantages and disadvantages.

Van den Boomgaard *et al* [38] assumed that if (1) the dielectric constant of BaTiO₃ >> dielectric constant of the ferrite, (2) Young's moduli for both phases are equal and (3) there is perfect coupling between the phases, then the ME voltage coefficient is given as:

$$\left(\frac{dE}{dH}\right)_{\text{comp}} = m_v \left(\frac{dx}{dH}\right)_{\text{ferrite}} \left(\frac{dE}{dx}\right)_{\text{BaTiO}_3} \quad (1-6)$$

where (dx/dH) is the change in dimension per unit magnetic field and (dE/dx) is the change in dimension per unit electric field. The subscript 'comp' stands for composite and m_v is the volume fraction of the ferrite. Using the maximum optimistic value for these parameters, the ME coefficient is estimated as 5 V/cm Oe. This value was later modified by Zubkov [127], giving the expression as:



$$\begin{aligned}\left(\frac{dE}{dH}\right)_{\text{comp}} &= m_v \left(\frac{dS}{dH}\right)_{\text{ferrite}} (1-m_v) \left(\frac{dE}{dS}\right)_{\text{piezo}} \\ &= m_v \left(\frac{dS}{dH}\right)_{\text{ferrite}} (1-m_v) (g_{33} C_{33})_{\text{piezo}}\end{aligned}\quad (1-7)$$

where g_{33} and C_{33} are the piezoelectric voltage and stiffness coefficients of the piezoelectric phase. This modification gives the ME voltage coefficient dE/dH as 0.92 V/cm Oe.

Harshe *et al* calculated the ME voltage coefficient theoretically by using a cubes model with 3 - 0 or 0 - 3 connectivity of phases [128]. They assumed a simple cube model, in which the particulate composites were considered as consisting of small cubes, and then solved the fields in one cube for which the boundary value problem involved is tractable. According to their results, for the best ME effect, both phases should have comparable elastic and dielectric properties. The maximum theoretical effect for the composites studied was found to be in a CoFe_2O_3 (80 %) and PZT - 4 (20 %) composite. The magnitude of the ME coefficient was 4.5 (V/m)/(A/m) (equals to ~ 358 V/cm·Oe). This simple cube model is an elementary single-grain model. Though conceptually straightforward and providing physical insight, it cannot be generalized to other phase topologies.

More rigorous treatments of the ME behavior of the composites were then performed by using physically based methods. One typical method is the Green's function technique (multiple-scattering approach). [33, 129] Green's function technique was developed for solving the constitutive Eq. (1-5) for the ME composites. It de-



rived the effective properties of the composites, defined as usual in terms of averaged fields. All effective properties of the composites can be obtained by this approach. With this method, Nan *et al* calculated the magnetoelectric coefficient $\alpha_{E, 33}$ for 0 - 3 or 1 - 3 $\text{CoFe}_2\text{O}_4/\text{BaTiO}_3$ ceramic composites (BaTiO_3 being the matrix phase). [33] The effect of the grain shape and phase connectivity on the ME response of this composites is also discussed. They demonstrated that for 0 - 3 particulate ceramic composites, the ME voltage coefficient $\alpha_{E, 33}$ reaches a maximum in the middle concentration region around $f \sim 0.6$ with $\alpha_{E, 33} \sim 400$ mV/cm Oe, but for 1 - 3 composites, the maximum $\alpha_{E, 33}$ appears at $f \sim 0.9$ with a relatively small $\alpha_{E, 33} \sim 200$ mV/cm Oe (f stands for the volume fraction of magnetic phase). This result is given in Fig. 1.14. Thus remarkable ME effect could be achieved in the composites with high concentration of particulate magnetic phase well dispersed in the piezoelectric phase.

Similarly, the constitutive equation (Eq. (1-5)) for the ME composites can also be solved by using micromechanics methods. Among them, Li [129 - 134] and Huang [135 - 137] gave more details about these micromechanics simulations. The micromechanics models are also formally straightforward and universal. It has been already known that micromechanics methods give almost the same approximations as the Green's function technique.

Although the calculations above focus on ferrites/piezoelectric ceramic composites with the piezoelectric phase as the matrix, not high enough resistivity of the ferrite phase would make it hard to obtain high ME response in the 0 - 3 particulate composites with high concentration of ferrite grains as expected, due to their large leakage. Also, it has been difficult to obtain qualified multiferroic 0 - 3 composite



ceramics due to ions diffusion during the sintering process while few research papers have reported about ferroelectric, piezoelectric and magnetic parameters.

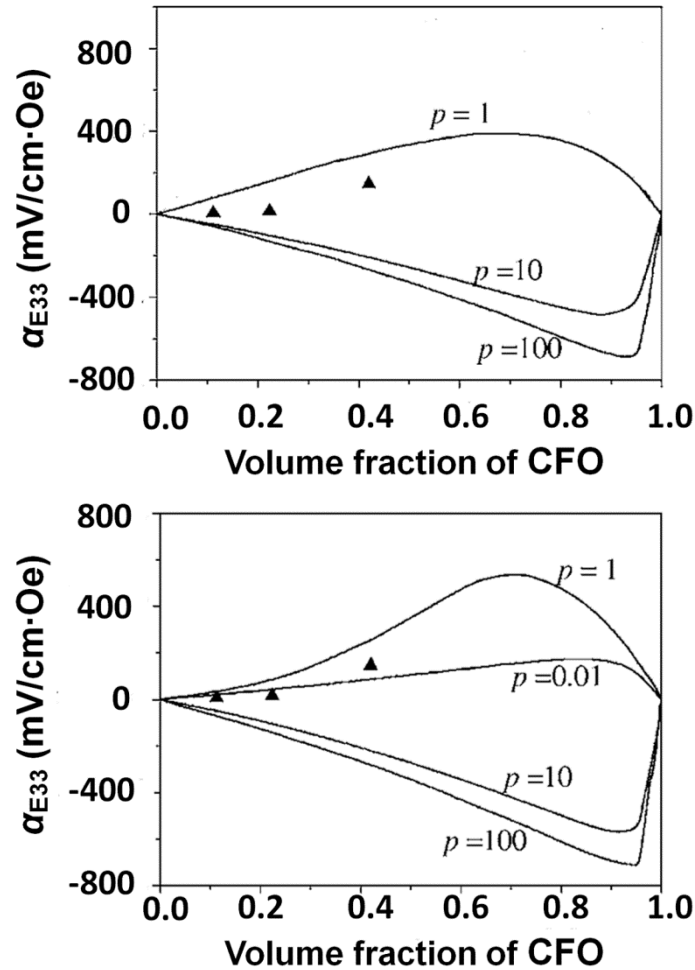


Fig. 1.14 Calculated $\alpha_{E,33}$ for 0 - 3 or 1 - 3 $\text{CoFe}_2\text{O}_4/\text{BaTiO}_3$ ceramic composites (BaTiO_3 as the matrix phase). [33]

1.3.4 Some key issues in 0 - 3 type ME ceramic composites

Although 0 - 3 ME ceramic composites were considered to exhibit promising



larger ME effects, the ME effect so far observed in co-fired ceramic composites is ten times or more lower than that predicted, mainly due to their inherent preparation problems, such as atomic interfacial diffusion and/or reaction problems between two ceramic phases during high-temperature preparation. A large number of combinations of piezoelectric oxides and magnetic oxides (mainly ferrites) have been studied. However, several important problems still remain to be solved, including:

1) Though most of the theoretical work devoted to the constitutive problem is based on the mechanical interaction between the components in a macroscopic view, little work is done to provide experimental evidence about the coupling in the scale of crystal lattice in 0 - 3 type composites. This issue is of importance to understand the mechanism of magnetoelectric coupling effect in composites.

2) Magnetoelectric composites are a multiphase material system expected to work under electric/magnetic field, while the piezoelectric/magnetic properties of its component is sensitive to the external field, which may cause the local material to exert its property under application. Such effect of microstructural inhomogeneity under external field is not studied in detail.

3) Another difficulty lies in the achievement of high concentration of magnetic phase in the composite. Though it is predicted theoretically the 0 - 3 type ceramic has a potential to produce larger coupling coefficient than 2 - 2 type composites, this conclusion is based on the assumption that the magnetic phase content in the composites could reach 0.4 - 0.6 for particles with an aspect ratio of ~ 1 . [33, 132, 133] In experiment, it still remains a problem to achieve a high concentration of the magnetic grain in the co-fired ceramics. At high magnetic phase content, current leakage hap-



pens through this phase and reduces or even breaks down magnetoelectric coupling. Considering this system as a resistance network, one may estimate the magnetic phase content above which such effects are likely to dominate. For a cubic lattice in three dimensions, the bond percolation threshold (p_c) occurs at ~ 0.25 , [138] while for a three-dimensional “Swiss cheese” continuum percolation model, p_c is ~ 0.3 . [139] Therefore, in 0 - 3 composites, electric leakage can only be expected to disappear with a magnetic phase weight content below 20 - 30 %. This is confirmed experimentally in 0 - 3 type co-fired piezoelectric-ferrite ceramics. For example, in BaTiO₃ - Ni_{0.3}Zn_{0.7}Fe_{2.1}O₄ ceramic composites, the percolation threshold happens at $p_c = 0.27$. [140, 141] Also, in most of the reported results about 0 - 3 co-fired ceramics, the systems exhibited the largest magnetoelectric effect at the lowest magnetic contents. This is because the large current leakage effectively precludes the use of piezoelectric effect. Besides, other difficulties related to electrical percolation from the low resistivity magnetic component includes limiting the electric field strength used for poling and resulting in the loss of induced voltage. [46, 142]

4) To achieve maximum product property, good mechanical interaction is required between the phases. At the same time, it is desired that no chemical reaction occur between the phases. In the sintered composites or the unidirectionally solidified composites of piezoelectric materials and ferrites, the temperature of processing is too high to avoid any chemical reaction of the phases. Also small deviations in compositions while sintering may cause a reasonable drop in the piezoelectric or magnetostrictive properties of the component phase. This will hinder their applications in real systems.



1.4 Scope of the present study

As discussed above, 0 - 3 type co-fired magnetoelectric ceramic composites has been extensively investigated but there are still a number of questions that remain unanswered. The research work for this thesis has been focusing on the following three issues, which, as we believe, are critical for better understanding of the structure - property relationship in 0 - 3 type ferroelectric/magnetostrictive composites: direct observation of lattice coupling, evaluation of the coupling efficiency, and influence of inhomogeneous internal electric field caused by the low-resistivity magnetostrictive phase. The primary objective for this dissertation is to (1) provide an experimental evidence for the mechanical coupling in 0 - 3 type ME composites; (2) study the influence of microstructural inhomogeneity on the magnetoelectric coupling effect; (3) develop a method to prevent the electric percolation in 0 - 3 type composites; and (4) make 0 - 3 type PZT - CFO ceramic composites-based prototype devices.

Following the introduction given in this Chapter, the thesis involves the next five Chapters:

Chapter 2 gives a short introduction to the key techniques that have been employed in the study, including X-ray diffraction, ferroelectric/magnetoelectric measurements, scanning electron microscope, and finite element analysis method.

Chapter 3 focuses on the experimental evidence for the mechanical coupling between magnetic and piezoelectric phases in 0 - 3 type PZT - CFO ceramic composites. The PZT - CFO composite was synthesized via conventional ceramic sintering method. With a static electric field applied on the composite, changes in lattice pa-



parameter of both PZT and CFO were observed by means of X-ray diffraction running in an ultra-slow mode. The experimental results have verified a coupled lattice distortion in the composite, providing an experimental evidence for the long-existing assumption that the ME effect is based on mechanical coupling. Based on the lattice distortion under different electrical fields, the ME coupling coefficient was also estimated.

Chapter 4 gives a numerical approach to estimate the magnetoelectric effect in composites with any desired structures. This method is based on finite element analysis method. By including a component to simulate the magnetostrictive effect, this method can be used to calculate the electric response of a composite to an applied magnetic field directly. In particular, the random distribution of CFO particles in 0 - 3 type ME composites is simulated by introducing a Monte - Carlo method. Besides, a method based on lattice coincidence is developed to evaluate the interfacial coupling efficiency in ME composites.

Chapter 5 is related to the influence of microstructural inhomogeneity in magnetoelectric composite. Analysis was made to investigate how the electrical field inhomogeneity in 0 - 3 type PZT - CFO composites would affect its performance via finite element analysis method. The effect of inhomogeneous internal electric field on the poling behavior (before use) and efficient piezoelectric property (under use) are both discussed. It is proposed that the difference in electrical property between PZT and CFO causes a large weakening in PZT's piezoelectric property. Such weakening effect concentrates in the interaction regions between the two phases, which will finally cause an enlarged weakening in the converse magnetoelectric effect.



Chapter 6 aims to improve the electric percolation effect on the magnetoelectric performance of the 0 - 3 type PZT - CFO. Composites with a core-shell type micro-structure were prepared. Wrapped with a thin layer of zirconia, CFO particles became electrical resistive and they would not form electrical conduction paths in the composite. With the shell to act as a barrier to electron and vacancy transportation, the leakage current of the composite material was significantly reduced, giving rise to enhanced coupling effect. In addition, effort has also been made to develop prototype devices using PZT - CFO composites as key materials. A magnetically tunable piezoelectric-transformer are designed with a step-down transformer structure and its response to both AC electric field (with/without DC bias) and an AC magnetic field were investigated respectively, which showed good sensitivity to both DC and AC magnetic field and are potentially useful for magnetic field detection.

Conclusions and suggestion for future work are given in Chapter 7.

1.5 Statement of original contribution

To the best of my knowledge, the present work has made the following original contributions:

Experimental evidence for the long-existing assumption that the ME effect is based on mechanical coupling is observed in 0 - 3 type magnetoelectric composites in the grain lattice scale by the method of X-ray diffraction.

The influence of microstructural inhomogeneity on the magnetoelectric coupling effect was studied in detail. Computation results show that the difference in electrical



property between PZT and CFO causes a large weakening in PZT's piezoelectric property and an enlarged weakening in the converse magnetoelectric effect.

A numerical approach is developed to estimate the magnetoelectric effect in composites with any designed structures. This approach can be based on the commercial finite element analysis software and is universal to composites with any complex structures.

Composites with a core - shell type microstructure were prepared to increase the percolation threshold in 0 - 3 type PZT - CFO ceramics. The modified composites are observed to exhibit enhanced piezoelectric and magnetoelectric properties. The composite is also used to fabricate a magnetically-tunable piezoelectric transformer based on its piezoelectric performance.



CHAPTER 2

Techniques for the study of 0 - 3 type $\text{Pb}(\text{Zr}, \text{Ti})\text{O}_3$ - CoFe_2O_4 composites

2.1 Introduction

The study of 0 - 3 type $\text{Pb}(\text{Zr}, \text{Ti})\text{O}_3$ - CoFe_2O_4 composites involves a number of advanced techniques and facilities. They include:

(1) Ceramic preparation: conventional ceramic sintering process, sputter coater (for Au electrode coating).

(2) Structural characterization: X-ray diffraction (XRD), scanning electron microscopy (SEM), SEM - BSE (backscattered electron), transmission electron microscopy (TEM).

(3) Electrical and magnetoelectric characterization: dielectric tests by impedance analyzer, ferroelectric tester, piezoelectric tester and magnetoelectric measurement.

(4) Numerical simulation: Finite Element Analysis (FEA).

In this Chapter, a short introduction is given to some typical techniques and equipment that were particularly useful in our research. They are: ferroelectric measurement, magnetoelectric measurement, XRD, SEM and finite element analysis method.



2.2 Ferroelectric measurement

2.2.1 Background

The hysteresis loop is referred to as the electric displacement (or polarization) - electric field loop ($D - E$ loop or $P - E$ loop as $D \propto P$ in a ferroelectric material), which is similar to that shown in Fig. 2.1. In the $P - E$ loops, the coercive field E_c , remnant polarization P_r , and spontaneous polarization P_s , of the material can be determined.

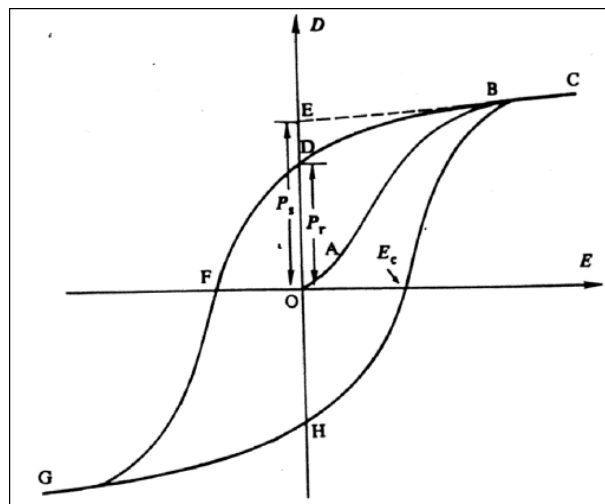


Fig. 2.1 A typical ferroelectric hysteresis loop.

2.2.2 Experimental set-ups

The hysteresis loops of the samples were measured by a modified Sawyer Tower circuit at 10 Hz [143]. Fig. 2.2 shows the basic idea of the Sawyer - Tower circuit in which C_F and C_R are the ferroelectric capacitor (sample) and a reference capacitor,



respectively. During the hysteresis measurements, the value of C_R should be much greater (around 1000 times) than that of C_F . Otherwise, the resultant hysteresis loop cannot be formed.

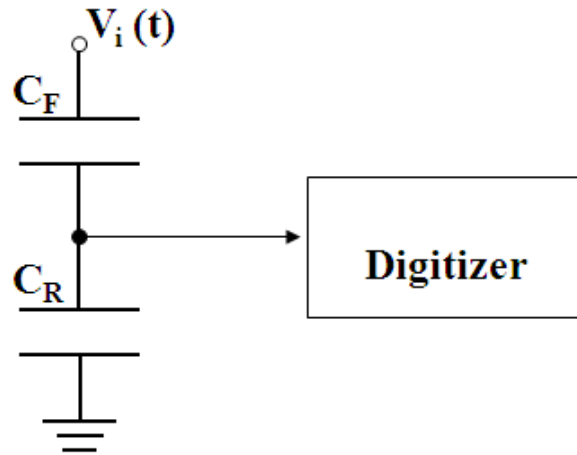


Fig. 2.2 A schematic circuit of the Sawyer - Tower bridge.

Figure 2.3 shows the computer-controlled experimental setup of the hysteresis measurement. During the measurement, the sample was put into a silicone oil bath to avoid electrical breakdown in air. An AC signal was applied to the sample by a function generator (HP 8116A), which was amplified by the high voltage amplifier (Trek 609D - 6). The input and the output signals from the Sawyer - Tower circuit were displayed on the screen of a digital oscilloscope (DSO). The $P - E$ loop of the sample can be observed directly on the computer monitor and the data can be extracted from the computer for further analysis.

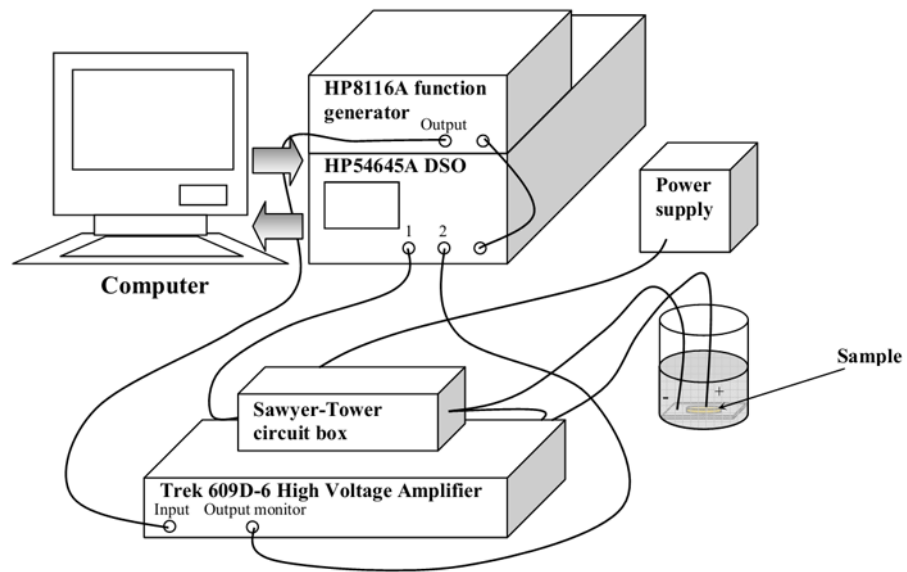


Fig. 2.3 A schematic diagram of the hysteresis measurement.

2.3 Magnetolectric measurement

2.3.1 Experimental set-ups

The set-up for measuring the direct magnetolectric effect is shown schematically, in Fig. 2.4. This consisted of:

(1) A Helmholtz coil which provided an AC magnetic field H_3 . This coil is driven by a dynamic signal analyzer (Ono Sokki CF5220) via a constant-current supply amplifier (AE Techron 7572).

(2) A U-shaped electromagnet (Myltem PEM-8005K) which provides a DC H_{Bias} . This electromagnet was controlled by a DC current supply (Sorensen DHP200-15).

(3) A pick-up coil connected to an integrating fluxmeter (Walker MF-10D) and a Gaussmeter (F. W. Bell 7030). This will monitor the H_3 and H_{Bias} in situ.



(4) A charge amplifier (Kistler 5015A) and an impedance analyzer (Agilent 4294A). From these two equipments, the induced charge (Q_3) in the composite and its capacitance(C) can be acquired.

During the measurement, all quantities mentioned above are recorded by the dynamic signal analyzer and stored in a computer.

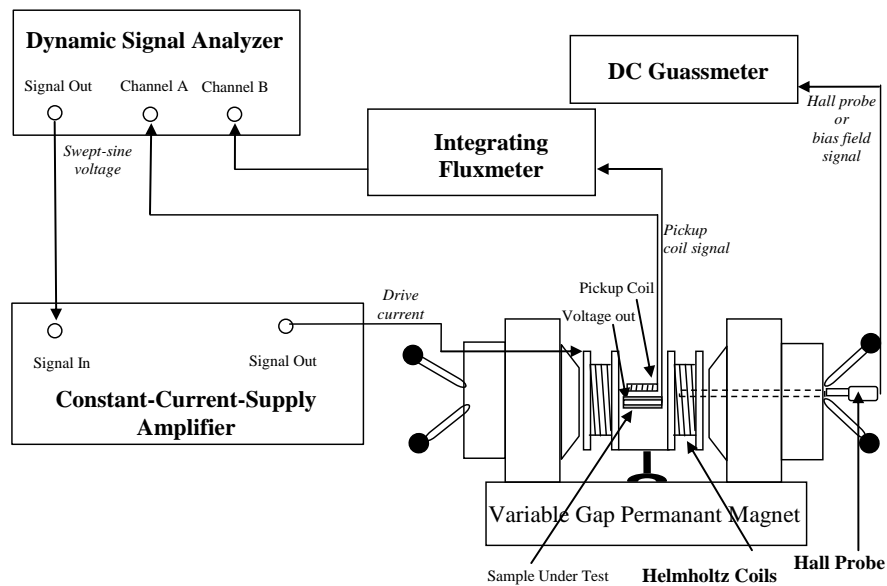


Fig. 2.4 A schematic diagram of the set-ups for magnetoelectric measurement.

2.3.2 Determination of the direct magnetoelectric coefficient

The direct magnetoelectric effect of the fabricated composite was characterized at room temperature and with zero stress bias. The ME voltage(V_3) induced in the composite was measured under different combinations of AC magnetic field strength(H_3), DC magnetic bias level (H_{Bias}), and AC magnetic field frequency(f) in



the ranges of 3×10^{-5} - 10 Oe, 0 - 9 kOe, and 1 - 100 kHz, respectively. V_3 was determined from the measured charges (Q_3) and capacitances (C) of the sample based on the relationship:

$$V_3 = \frac{Q_3}{C} \quad (2-1)$$

The dependence of the ME voltage coefficient ($\alpha_{E,33}$) on both H_{Bias} and f was established from the slope of the corresponding $V_3 - H_3$ plot, i.e.,

$$\alpha_{E,33} = \frac{\partial E_3}{\partial H_3} \quad (2-2)$$

where E_3 is the induced electric field that can be obtained from V_3 and the thickness of the sample.

2.4 X-ray Diffraction (XRD)

X-ray diffraction (XRD) is a well-established non-destructive analytical technique which reveals information about the crystal structure, chemical composition and many other properties of materials. In this Section, a short introduction is given to the technique and the instruments. Detailed introduction is given in Chapter 3.



2.4.1 Principle of XRD measurement techniques

When an incident X-ray beam interacts with the atoms arranged in a periodic manner as shown in Fig. 2.5 (a), the atoms, represented as green spheres in the graph, can be viewed as forming different sets of planes in the crystal (straight lines in Fig. 2.5 (a)).

For a given set of lattice planes with an inter-planar distance of d , the condition for a diffraction (peak) to occur can be simply written as the Bragg's law (Fig. 2.5 (b)), i.e.:

$$2d\sin\theta = n\lambda \quad (2-3)$$

where λ is the wavelength of the X-ray, θ the scattering angle, and n is an integer representing the order of the diffraction peak. The Bragg's law is one of most important laws used for interpreting X-ray diffraction data.

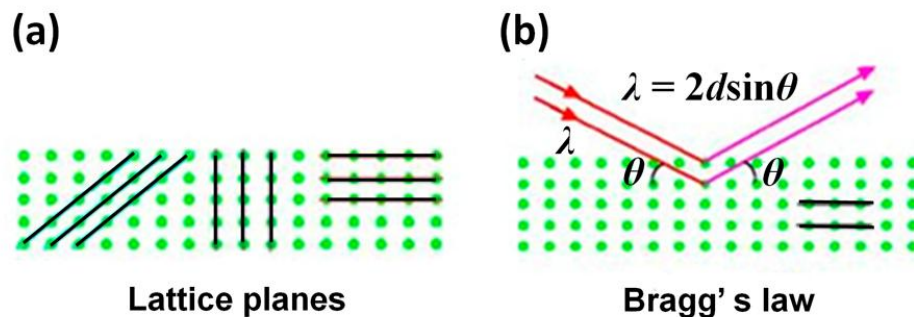


Fig. 2.5 Illustration for the (a) lattice grains and (b) Bragg's law.



2.4.2 The instrument

The X-ray diffraction measurements of the composites were carried out on a Rigaku automated multipurpose Smartlab X-ray diffractometer (XRD: Rigaku Corp., Tokyo, Japan) shown in Fig. 2.6. The X-ray source is a long-fine-focus, ceramic X-ray tube with Cu anode. Normal operating power is 40 kV and 40 mA and Cu $K\alpha_1$ radiation with a wavelength $\lambda = 0.15406$ nm is used. The sample stage supports specimens of a wide variety of shapes and sizes.



Fig. 2.6 The Rigaku automated multipurpose Smartlab X-ray diffractometer.



2.5 Scanning electron microscope

Scanning electron microscope (SEM) is a type of electron microscope to explore the microstructure of materials. It can form images of a sample by scanning it with a beam of electrons. The electrons interact with the atoms that make up the sample producing signals that contain information about the sample's surface topography, composition, and other properties such as electrical conductivity.

2.5.1 General principle

In SEM, the sample is bombarded by a focused beam of electrons. Most incident electrons interact with specimen atoms and are scattered, rather than penetrating the sample. They follow complicated twisting paths through the sample material, losing energy as they interact.

The scattering events are of two types, either elastic or inelastic. In elastic scattering, the electron trajectory changes, but its kinetic energy and velocity remain essentially constant. This is because of the large difference between the mass of the electron and atomic nuclei. Alternatively, in inelastic scattering, the trajectory of the incident electron may be only slightly perturbed, but energy is lost through interaction with the orbital electrons of the atoms in the specimen.

Inelastic interactions produce a number of effects, including secondary electrons (SE), backscattered electrons (BSE), cathodo luminescence (CL), continuum X-ray radiation, characteristic x-ray radiation and phonons (heat).



Different effects can be detected from different interaction volume, which is plotted in Fig. 2.7. This is because beam electrons lose energy during interactions within the sample. Electron energy generally decreases with depth. As a result, if a certain amount of energy is required to produce an effect, it will not be possible to produce it from the deeper portions of the volume.

The degree to which an effect can be observed is controlled by how strongly it is diminished by absorption and scattering in the sample. For example, secondary electrons are produced throughout the interaction volume, but have very low energies and can only escape from a thin layer near the sample's surface. Similarly, soft X-rays, which are absorbed more easily than hard X-rays, will escape more readily from the upper portions of the interaction volume.

2.5.2 Secondary electron image

The most common imaging mode collects low-energy (< 50 eV) secondary electrons that are ejected from the k-orbitals of the specimen atoms by inelastic scattering interactions with beam electrons. Due to their low energy, these electrons originate within a few nanometers from the sample surface.

Secondary electron (SE) images show morphology and topography of a sample. In SE image, steep surfaces and edges tend to be brighter than flat surfaces, which results in images with a well-defined, three-dimensional appearance. Using the signal of secondary electrons image resolution less than 0.5 nm is possible.

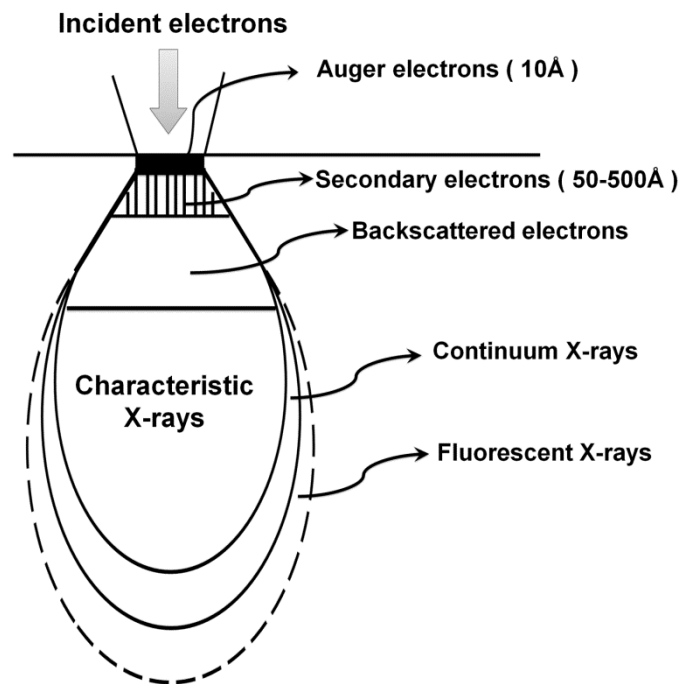


Fig. 2.7 Illustration of interaction volumes for various electron - specimen interactions.

2.5.3 Backscattered electron image

Backscattered electrons (BSE) consist of high-energy electrons that are reflected or back-scattered out of the specimen interaction volume by elastic scattering interactions. Since heavy elements (high atomic number) backscatter electrons more strongly than light elements (low atomic number), and thus appear brighter in the image, BSE are used to detect contrast between areas with different chemical compositions.

Backscattered electrons can also be used to form an electron backscatter diffraction (EBSD) image that can be used to determine the crystallographic structure of the specimen.



2.6 Finite element analysis (FEA)

2.6.1 General principle

The study of physical systems frequently results in partial differential equations which either cannot be solved analytically or lack an exact analytic solution due to the complexity of the boundary conditions or domain. For a realistic and detailed study, a numerical method must be used to solve the problem. The finite element method is often found to be the most adequate. In this thesis, the finite element approach is used to simulate the local electric field, the piezoelectric response of the component in the composite, as well as the coupling effect.

Basically, the finite element method (Zienkiewicz, 1971; Reddy, 1984; Hughes, 1987) consists in a piecewise application of classical vibrational methods to smaller and simpler subdomains (called finite elements) connected to each other in a finite number of points (called nodes). The fundamental principles of the finite element method (displacement) are:

- (1) The continuum is divided into a finite number of elements of geometrically simple shape.
- (2) These elements are connected in a finite number of nodes.
- (3) The unknowns are the displacements of these nodes.
- (4) Polynomial interpolation functions are chosen to describe the unknown displacement field at each point of the elements related to the corresponding field values at the nodes.



(5) The forces applied to the structure are replaced by an equivalent system of forces applied to the nodes.

2.6.2 Modeling of piezoelectric and magnetostrictive problems

Generally, linear piezoelectricity can be described by the following equation:

$$\begin{pmatrix} S \\ D \end{pmatrix} = \begin{pmatrix} s^E & d^t \\ d & \varepsilon^T \end{pmatrix} \begin{pmatrix} T \\ E \end{pmatrix} \quad (2-4)$$

where D is electrical charge displacement, S the strain, T the stress, E the electric field strength, s^E the compliance, d the direct piezoelectric effect, d^t the converse piezoelectric effect, and ε is the permittivity. Since normal piezoelectric materials shows linear response, this formula is accurate enough for calculation.

Oppositely, magnetostriction is often not a linear response, at low values, the strain - magnetic field relation is approximately quadratic, as schematically illustrated in Fig. 2.8. However, in practice, the H -field excitation is often small, so the linear simplification is acceptable. We estimate the magnetostrictive coefficient $d = \Delta\sigma/\Delta H$, as illustrated in Fig. 2.8. Then the constitutive equations for the magnetostriction can be described by:



$$\begin{pmatrix} S \\ B \end{pmatrix} = \begin{pmatrix} s^E & d_m^t \\ d_m & \mu^T \end{pmatrix} \begin{pmatrix} T \\ H \end{pmatrix} \quad (2-5)$$

where B is magnetic flux density, H the magnetic field strength, s^E the compliance, d_m the direct magnetostrictive coefficient, d_m^t the converse magnetostrictive coefficient, and μ^T is the permeability.

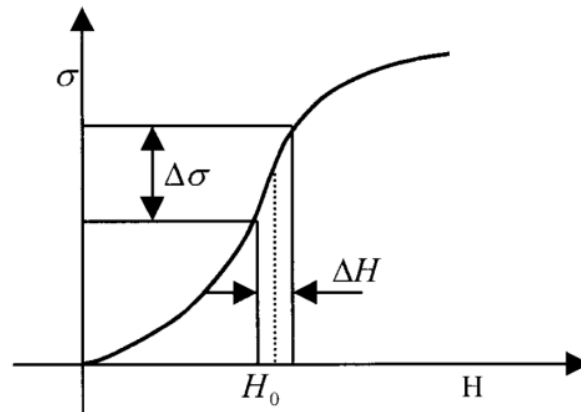


Fig. 2.8 Schematic illustration of determination of magnetoelastic coupling coefficient.

Rigorously, these equations described every single spatial point in the defined geometry of the problem. And the fields must be continuous across the entire volume. Hence the problem is reduced to the finding of solution to these equations under the constraints of continuity. However, except for several accurate methods for solution of specified geometry (rectangular, or sphere, etc.), there are no analytical solution to



these kinds of problem. FEA generally divides the geometry into thousands of simple elements/meshes (ordinarily using tetragonal elements), which can be solved analytically. And the overall solution is to solve all these equations in every element and to simultaneously obey the condition of continuity.

2.6.3 Simulation using COMSOL multi-physics software

COMSOL multi-physics is a software that can be applied in various fields including structural engineering, RF engineering, fluid dynamics and acoustics etc. Numerous scientific research has been published based on the results calculated by COMSOL. The software is considered as a credible solution to FEA problems. The operation of the software generally includes the following steps:

(1) Geometrical modeling: the software provides numerous geometrical modeling tools. 3D tools include blocks, cones, cylinders, spheres and ellipsoids etc. Also, one can exploit the geometrically Boolean operation of union, difference, intersection and so on, to build more complicated geometries.

(2) Physics settings: the ordinary/partial differential equations are internally built in the physics model of the software package. After the geometrical modeling, one should select the corresponding physical model (in our case, model of piezoelectricity, which contains the algorithm for solving Eq. (2-4)), to specify basic equations the problem involved. Material properties must be specified for each geometrically separated region, to provide associative constants (also in Eq. (2-4)). Also, boundary conditions must be added to make the problem solvable. These boundary conditions



will be different on different surfaces, lines and points.

(3) Mesh generation: this process is to divide the whole geometry into small elements where physical properties are assumed to be uniform. The assembly of the small elements is called meshes. Principally, the finer the meshes are generated, the more accurate the result will be, while the lower the speed of solving. COMSOL provides different mesh generating options.

(4) Computing and solution: after the previous 3 steps, the problem can be analyzed after different algorithms. These algorithms are generally different approaches to solve a super large linear matrix equation. The problems can be solved are “stationary” type, “time-dependent” type, “eigenfrequency” type and so on.

(5) Post-processing and visualization: COMSOL also provides post-processing models to present the calculated data graphically. Conventionally, any scalar fields can be displayed by color scales on the geometry built at step 1, vector fields can be displayed by arrows with different colors or lengths.

To visualize the simulation procedure, an example is introduced to display the construction of model and retrieval of results. This example involves a static 3D analysis of an oblate cylinder type piezoelectric actuator, which convert applied voltage to the variation of thickness.

Figure 2.9 shows the operation process of the piezoelectric modeling via COMSOL multi-physics software. A ceramic disc can be drawn through the software. (Fig. 2.9 (a)) The parameters are 10 mm in radius and 2 mm in height, respectively. After the geometrically modeling, Materials and boundary conditions should be specified.



In this example, we set the material to be PZT-4H with constants offered by the software data base. The bottom face is set to be electric ground with potential $V = 0$, and the upper face is set as constant potential $V = 100$ V, which resembles two layers of electrodes for loading of external voltages. Also, we set spatial constraints around the side surface of the cylinder.

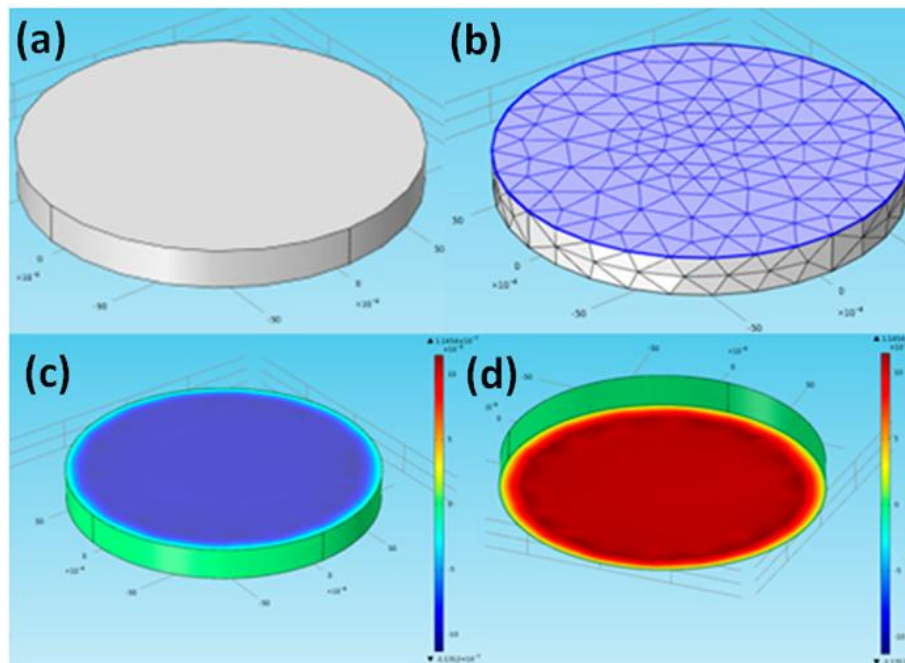


Fig. 2.9 Illustration for the modeling of piezoelectric ceramic through COMSOL multi-physics software. (a) The operation geometric model, (b) the meshes generated in COMSOL by default options, (c) the displacement at the upper surface and (d) the displacement at the bottom surface.

Figure 2.9 (b) shows the meshes generated in default options set by COMSOL, the sizes of unit elements are approximately $0.3 \text{ mm} \times 0.3 \text{ mm} \times 0.2 \text{ mm}$. Figs. 2.19



(c) and 2.19 (d) show the simulation results of the downward displacements and upward displacements. The final results show that the PZT cylinder is “pressed” by the applied voltage. The maximum displacement is $0.114 \mu\text{m}$.

2.7 Summary

A number of advanced techniques were used in the fabrication and characterization of $\text{Pb}(\text{Zr}, \text{Ti})\text{O}_3 - \text{CoFe}_2\text{O}_4$ particulate composites. In this Chapter, we have only demonstrated three typical techniques. In the following Chapters, more discussions on the fabrication and characterization techniques will be given whenever necessary.



CHAPTER 3

Direct observation of lattice coupling in 0 - 3 Type Pb(Zr, Ti)O₃ - CoFe₂O₄ composites

3.1 Introduction

ME effect in composites is a product tensor property of the magnetostrictive effect (magnetic/mechanical effect) and the piezoelectric effect (mechanical/electrical effect). The coupling between the magnetic phase and the piezoelectric phase is realized through elastic interaction at their interface. That is, when a magnetic field is applied to a composite, the magnetic phase changes its shape magnetostrictively. The strain is then passed along to the piezoelectric phase, resulting in an electric polarization. As a result, ME effect in composites is a complex and extrinsic property, depending on the composite microstructure and coupling interaction across the magnetic - piezoelectric interfaces. Composites with different types of connectivity (0 - 3 type, 2 - 2 type and 1 - 3 type) have been developed to improve the coupling effects in ME composites. However, there is still much room for improvement when compared to theoretical predictions. One reason responsible for the variance between experimental data and theoretical predictions could be attributed to the non-ideal elastic coupling at the interface between different components in the composites.

In this Chapter, we perform a direct observation of coupled lattice distortion in 0 - 3 type ME composites using XRD measurements. An in-situ XRD study of the crystalline structure was conducted on particulate PZT - CFO ceramic composite



under a static electric field, and special attention was paid to the characteristic XRD peaks of the piezoelectric phase (PZT) and magnetostrictive phase (CFO). A simple model based on the lattice distortion of both component phases under a static electric field was also proposed to estimate the magnetoelectric coupling coefficient under an ideal condition.

This Chapter is divided into eight sections including the Introduction. Section 3.2 provides a short introduction to X-ray diffraction (XRD) technique, especially its use for analysis of lattice strain. Section 3.3 provides a literature review of prior work on investigation of coupled magnetoelectric effect in microstructure. Sections 3.4 and 3.5 give the experimental procedures, and the structure and morphologies of the composite. Section 3.6 focuses on the XRD study of the coupled ME effect and a detailed discussion of the result. In Section 3.7, a numerical method based on the mechanical coupling between the component phases is proposed to estimate the magnetoelectric effect.

3.2 Investigation of grain lattice by X-ray diffraction

X-ray diffraction (XRD) is a well-established non-destructive analytical technique which reveals information about the crystal structure, chemical composition and many other properties of materials. In our study, the technique of X-ray diffraction (XRD) was employed to characterize the crystalline structure of both components in the composite. In particular, the lattice parameters, and the induced strains in PZT and CFO were determined by means of XRD.



3.2.1 Determination of lattice constant by XRD

Figure 3.1 gives a typical XRD peak. One can see that the peak shapes in XRD pattern are characterized by three factors, including peak position 2θ , peak width (represented by the full width at half maximum, FWHM), and peak intensity (I_{\max}). Among these factors, the peak position 2θ , is important for obtaining information about the lattice parameters as well as uniform strain within the lattice. [144]

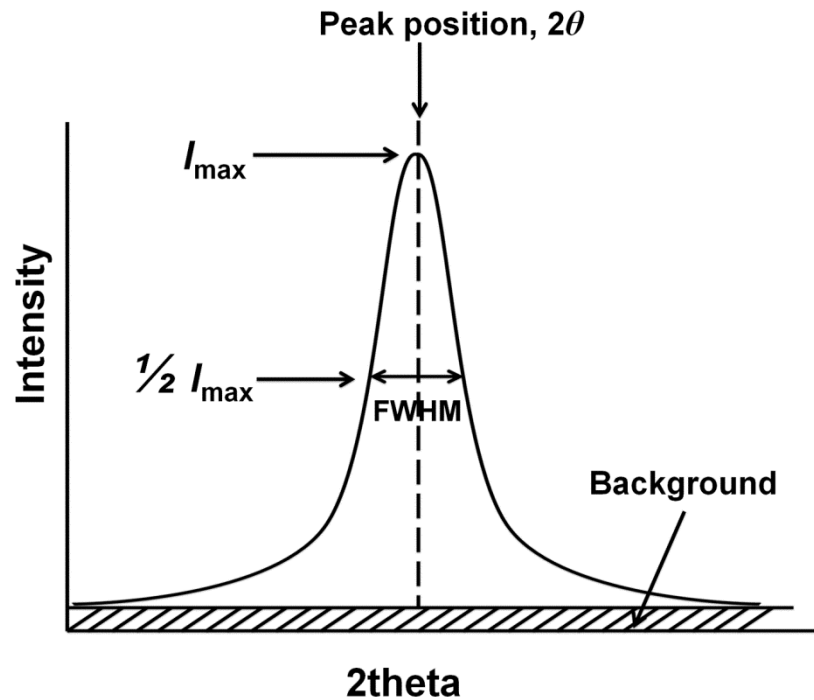


Fig. 3.1 Illustration of a typical peak in XRD patterns.

For the observed $\sin\theta$ value of any peak in an indexed XRD pattern, the unit-cell dimension can be determined by employing the Bragg's equation. For example, for a cubic structure, we have:



$$a = \frac{\lambda \sqrt{h^2 + k^2 + l^2}}{2 \sin \theta} \quad (3-1)$$

To investigate the errors in determining the lattice parameters in this way, we differentiate the Bragg's equation with respect to θ :

$$n\lambda = 2d \sin \theta$$

$$0 = 2 \frac{\Delta d}{\Delta \theta} \sin \theta + 2d \cos \theta \quad (3-2)$$

$$\frac{\Delta d}{d} = -\frac{\cos \theta}{\sin \theta} \Delta \theta = -\cot \theta \Delta \theta$$

For the cubic system, it is evident that $\Delta d/d = \Delta a/a$, hence:

$$\frac{\Delta a}{a} = -\cot \theta \Delta \theta \quad (3-3)$$

Eq. (3-3) shows that, for a given precision of measurement of the diffraction angle $\Delta \theta$, the precision in a is proportional to $\cot \theta$. The error in calculating the lattice parameters with this method tends to a minimum as θ approaches 90° .



3.2.2 Determination of lattice strain by XRD

Stress - strain phenomena are conventionally illustrated by the dimensional changes of a uniform material bar when a tension is applied along its axis. Under such stress the bar is lengthened, and its area of cross section decreases in direct proportion to the applied stress, provided that the bar's elastic limit has not been exceeded. The resultant effect on each individual crystallite in this bar is an extension in the direction parallel to the bar axis and a compression in directions normal thereto. Crystal planes perpendicular to these extensive or compressive forces have their interplanar spacings changed by amounts $\pm\Delta d$, and measurement of this change yields a measure of the elastic strain and thereby of the stress as well.

Figure 3.2 gives two variations in XRD peaks caused by different types of lattice strain in materials. Fig. 3.3 (a) stands for the original crystal grains and corresponding XRD peak without strain. Strain within the lattice can distort the lattice leading to a shift of the d spacing (δd). If the lattice distortion is uniform within the lattice, even expansion or contraction perpendicular to the crystal grains happens, which presents in the XRD peak as a left or right shift to its original position without changing its shape (shown in Fig. 3.3 (b)). The relationship between the strain and the shift of θ (marked as $\delta\theta$) can be obtained by differentiating the Bragg equation with respect to d and θ with λ fixed, i.e.:

$$0 = 2 \times \delta(d) \times \sin\theta + 2 \times d \times \delta(\sin\theta) \quad (3-4)$$



which can be arranged as:

$$(\delta d)/d = \delta \varepsilon = \text{strain} = - \delta(\sin\theta)/\sin\theta = - \cot\theta\delta\theta \quad (3-5)$$

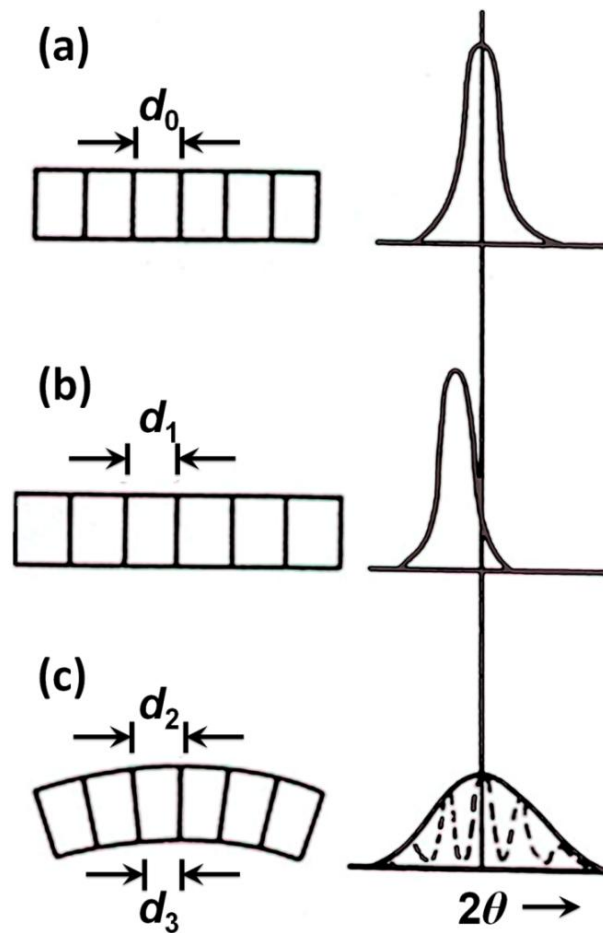


Fig. 3.2 Two types of strain-induced lattice deformation and the corresponding XRD peak. (a) Original lattice without strain, (b) lattice with uniform expansion and (c) lattice with non-uniform deformation.



Apart from the strain given in Fig. 3.2 (b), strain within the lattice may also arise from residual stress and is then non-uniform within the lattice, as shown in Fig. 3.3 (c). This will lead to a range of δd , rather than a single value of “ δd ”. Consequently a small range of the diffraction angle for a given $(h k l)$ is induced, i.e., the $\delta\theta$ can be on either side of the peak position. This will in turn cause overall widening effect in the peak.

In this Chapter, we focused on the strain caused by the piezoelectric effect and the mechanical coupling in the converse magnetoelectric effect. Such strain is caused by a field-induced (for the piezoelectric phase) or stress-induced (for the magnetostrictive phase) expansion or contraction of the lattice, which is sorted into the uniform strain in Fig. 3.2 (b).

3.3 Prior investigations of the coupled magnetoelectric effect

In the literature, a number of studies have been conducted to reveal the stress-induced ME coupling mechanism in microstructure. Two techniques widely used are the Raman spectra and X-ray diffraction (XRD). Li *et al* used Raman scattering to study the magnetic-field-induced stress in $\text{Pb}(\text{Zr}, \text{Ti})\text{O}_3 - \text{CoFe}_2\text{O}_4$ (PZT - CFO) bilayered system and pointed out that the magnetostriction of CFO layer is responsible for the changes in the phonon modes in the PZT - CFO films. X-ray diffraction is also a well-established method for characterizing crystalline properties of materials, including the determination of lattice parameters as well as strain in the lattice. [145] Zheng *et al* used XRD measurement to examine the piezoelectric substrate-induced strain on magnetoresistive manganate films grown on ferroelectric



Pb(Mg, Nb)O₃ - PbTiO₃ substrate, giving direct evidence for the mechanical interaction between the piezoelectric and the magnetic phases in the heterostructures. [146, 147] For example, in Ref [146], Zheng *et al* used XRD to study the substrate-induced strain effect in La_{0.875}Ba_{0.125}MnO₃ (LBMO) thin films grown on ferroelectric single-crystal 0.67Pb(Mg_{1/3}Nb_{2/3})O₃ - 0.33PbTiO₃ (PMN - PT) substrate. Both the strain and resistance of the films were in situ varied by applying an electric field across the PMN - PT substrates. X-ray diffraction analysis (Fig. 3.3) indicates that the variations of strain and resistance result from the induced strain in the PMN - PT substrate due to the ferroelectric polarization or the converse piezoelectric effect. The relationships between the resistance and the induced strain in the LBMO film and PMN - PT substrate were quantitatively analyzed (see Fig. 3.4).

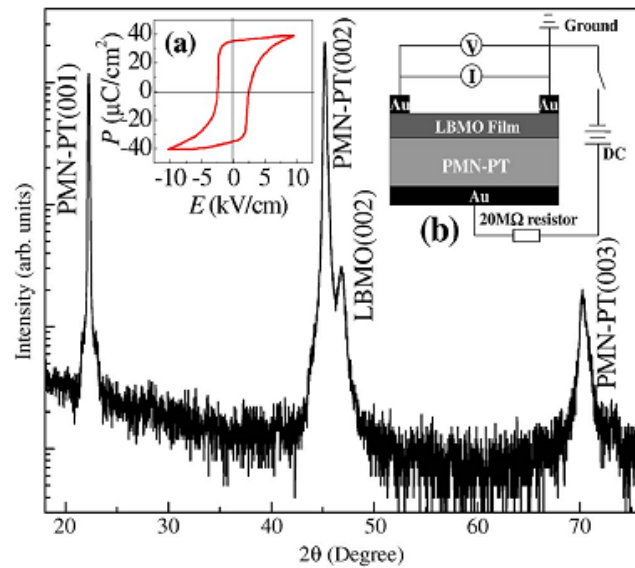


Fig. 3.3 XRD pattern of the LBMO/PMN - PT structure. Insets (a) and (b) are the ferroelectric hysteresis loop of the PMN - PT substrate and the electrical measurement circuit, respectively. [146]

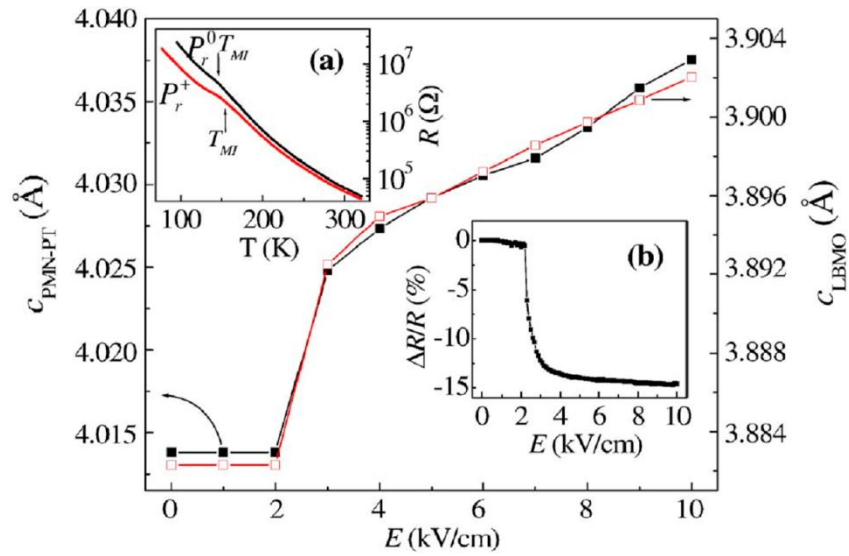


Fig. 3.4 Lattice constant c of the PMN - PT substrate and LBMO film as a function of the electric field. Insets (a) and (b) show the temperature and field dependence of the resistance for the LBMO film, respectively. [146]

Nevertheless, most work on coupling observation was based on a 2 - 2 layered structure. For 0 - 3 type composites (which could provide more room to enhance coupling due to their complex structure and freedom in design), little experimental evidence has been available for revealing how the components in these composites interact with each other in the lattice scale. Having noticed this, our experiment is designed to focus on the 0 - 3 type composites, with lead zirconate titanate as the piezoelectric phase, and cobalt ferrite as the magnetostrictive phase.



3.4 Experimental procedure

3.4.1 Preparation and structural characterization of 0 - 3 type Pb(Zr, Ti)O₃ - CoFe₂O₄ composites

The composites were prepared via traditional ceramic synthesis process from commercially available powders PZT502 (from PKI USA) and CFO (from Aladdin China, sphere, 40 nm). The PZT powder was first mixed with sintering additives and pre-sintered at 600 °C for 2 h before the processed PZT powder was mixed with CFO powder at a weight ratio of 1 : 0.05. This well dispersed mixture was then pressed into disc at a pressure of 12 MPa, and sintered in air at 1050 °C for 2 h. The micro-structure of the sample was examined by transmission electron microscopy (TEM) and XRD.

3.4.2 Poling and piezoelectric measurements

After firing silver electrodes on its both sides, the sample was electrically polarized in its thickness direction in silicone oil under a field of 7 kV/mm at 80 °C. The piezoelectric constant d_{33} was measured using a standard piezo d_{33} meter (model ZJ-3A).

3.4.3 XRD study of the composite under electric field

To perform the XRD study under an electric field, the sample was polished and



thinned down to a thickness of 0.168 mm, coated with thin Au electrodes on both sides using a sputter coater (BAL-TEC SCD 005) at a current of 80 mA for 180 s before it was adhered to a microscope slide by silver paint. Two copper electrodes were fixed on the two edges of the microscope slide. The bottom surface of the sample was electrically connected to one copper electrode via the silver paint, and the upper surface was connected to the other copper electrode using a silver filament (Fig. 3.5). A Keithley 1100 V DC bias sourcemeter (Model 2410) was used to generate a static DC bias. The crystalline structure of the prepared sample under an electric field was then examined by X-ray diffraction using a Rigaku automated multipurpose Smartlab X-ray diffractometer (XRD: Rigaku Corp., Tokyo, Japan).

3.5 Structures and morphology of the composites

3.5.1 Crystal structure of CFO, PZT and 0 - 3 type PZT - CFO composites

The crystal structure of the sample has been verified by the XRD patterns as shown in Fig. 3.6. Figs. 3.6 (a) and 3.6 (b) show the XRD patterns of pure PZT and CFO ceramics sintered from the same raw material and sintering method which can be characterized as pure PZT perovskite structure (PDF # 33 - 0784) and CFO spinel structure (PDF # 03 - 0864), respectively. The pattern of PZT - CFO composites in Fig. 3.6 (c) is found to be a combination of these two sets of XRD patterns. To show CFO's peaks (marked with hollow square) clearly, the intensity in Fig. 3.6 (c) is presented in log scale.

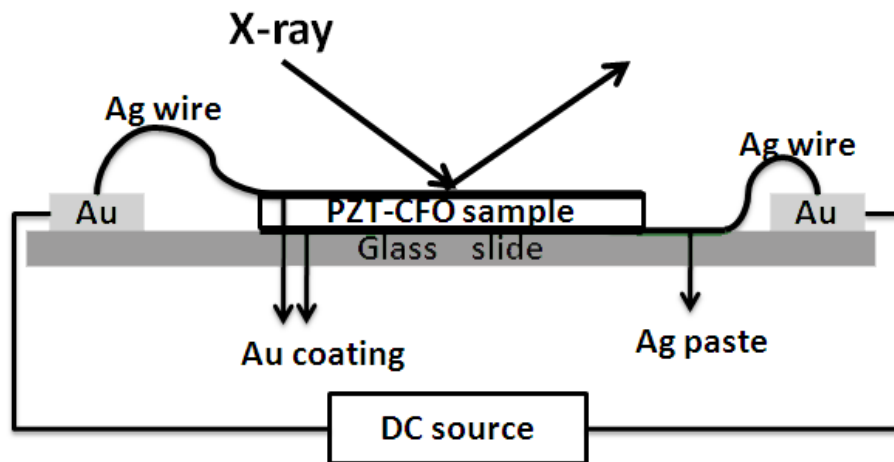


Fig. 3.5 Illustration of the sample used for XRD measurement.

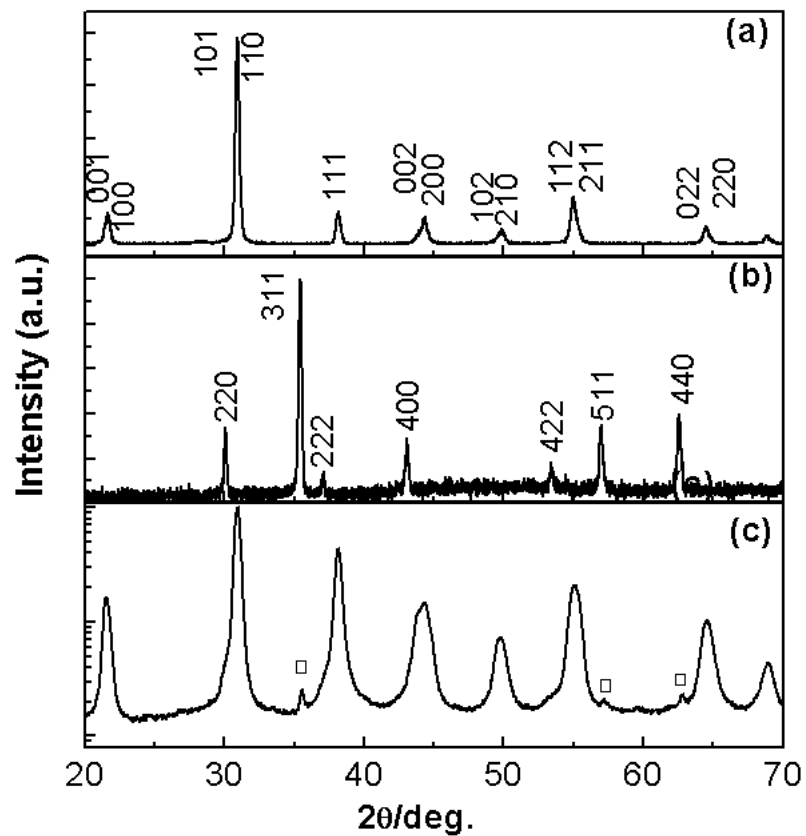


Fig. 3.6 XRD patterns of (a) PZT, (b) CFO and (c) PZT - CFO ceramics.



3.5.2 Microstructure of 0 - 3 type PZT - CFO composite

Figure 3.7 shows TEM images of the sample. According to the EDS-mapping analysis of the random local area in PZT - CFO ceramics, CFO grains are distributed uniformly in PZT ceramics, as indicated by the white arrow (the EDS mapping data is not shown here). Fig. 3.7 (b) and the inset of Fig. 3.7 (a) show the HRTEM image and SAED pattern in the thin area of the complex ceramics.

The single crystalline diffraction pattern belongs to the PZT phase, corresponding to the (011) and (200) planes, respectively, while the polycrystalline diffraction ring belongs to the CFO phase, corresponding to the (110) and (311) planes, respectively. In addition, from the HRTEM image, the two phases show a clear grain boundary (as shown by the white circle), suggesting that the CFO phase contacts the PZT phase directly without a second phase between them.

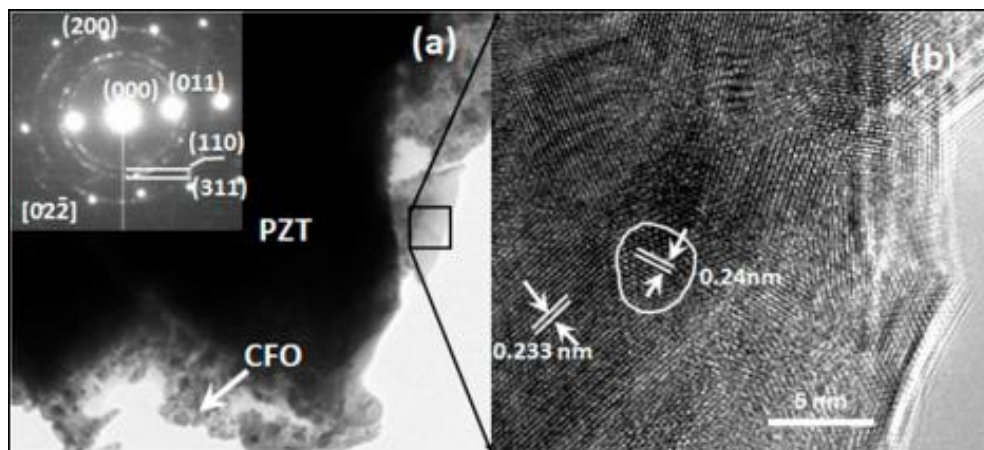


Fig. 3.7 TEM images of the PZT - CFO ceramic at (a) low and (b) high magnification. The inset of (a) is the corresponding SAED pattern.



3.6 XRD study of the converse magnetoelectric effect

3.6.1 Experiments

The in-situ XRD study for observation of lattice coupling was conducted. In the measurement, a very slow scan ($0.1^\circ/\text{min}$) was performed within the 2θ range of 20° to 70° . The XRD patterns of the sample without a DC bias, under a DC bias (1100 V), and after removing the bias (DC off) were scanned in sequence. Each scanning started after keeping the corresponding state for 30 minutes. During the measurement, both the X-ray generator and the detector rotated at half of the diffraction angle θ , while the sample was kept still in the sample holder (see Fig. 3.8). This could ensure that all the observed crystal planes were parallel to the top surface of the sample. Consequently, the calculated lattice deformation based on the shift of the XRD patterns is along the direction normal to the sample surface.

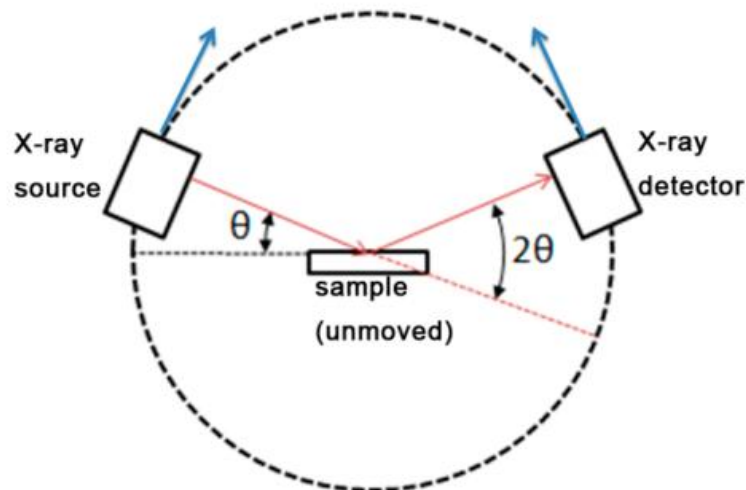


Fig. 3.8 Illustration of the $\theta - 2\theta$ scan used in the measurement.



3.6.2 Results and discussions

Figure 3.9 (a) presents the diffraction profiles during the measurement with the intensity in log scale. Two typical peaks, PZT's (211) peak and CFO's (511) peak, are selected and shown in Figs. 3.9 (b) and 3.9 (c) to present a clearer view (in normal scale). According to Fig. 3.9 (b), the (211) peak of PZT is located at 55.08° initially before dropping to 55.03° at $V = 1100$ V, implying a strain induced by the converse piezoelectric effect within its lattice. After the electric field is removed, the peak returns to its original position at 55.08° , indicating the electrical field-induced lattice distortion is revertible. Accompanying the change in PZT's grain lattice, the (511) peak of CFO shows similar variation trends under an electric field (see Fig. 3.9 (c)), with its peak position fitted as 57.17° ($V = 0$), 57.08° ($V = 1100$ V), and 57.15° (DC off), respectively. According to Bragg's law, the strain perpendicular to the corresponding crystal plane ($h k l$) can be calculated as:

$$S_{hkl} = \frac{\Delta d_{hkl}}{d_{hkl}} = -\cot \theta \cdot \Delta \theta \quad (3-6)$$

where θ and $\Delta \theta$ can be derived from the XRD pattern, d_{hkl} the lattice space of the plane ($h k l$), Δd_{hkl} the change in the lattice space, and S_{hkl} is the strain along the direction of $[h k l]$. Based on Eq. (3-7), in our sample, the strain within PZT along the [211] direction is 8.37×10^{-4} and the induced strain within CFO along the [511] direction is 6.40×10^{-4} . As mentioned before, the calculated strains of the two phases are both in the direction normal to the sample's top surface.

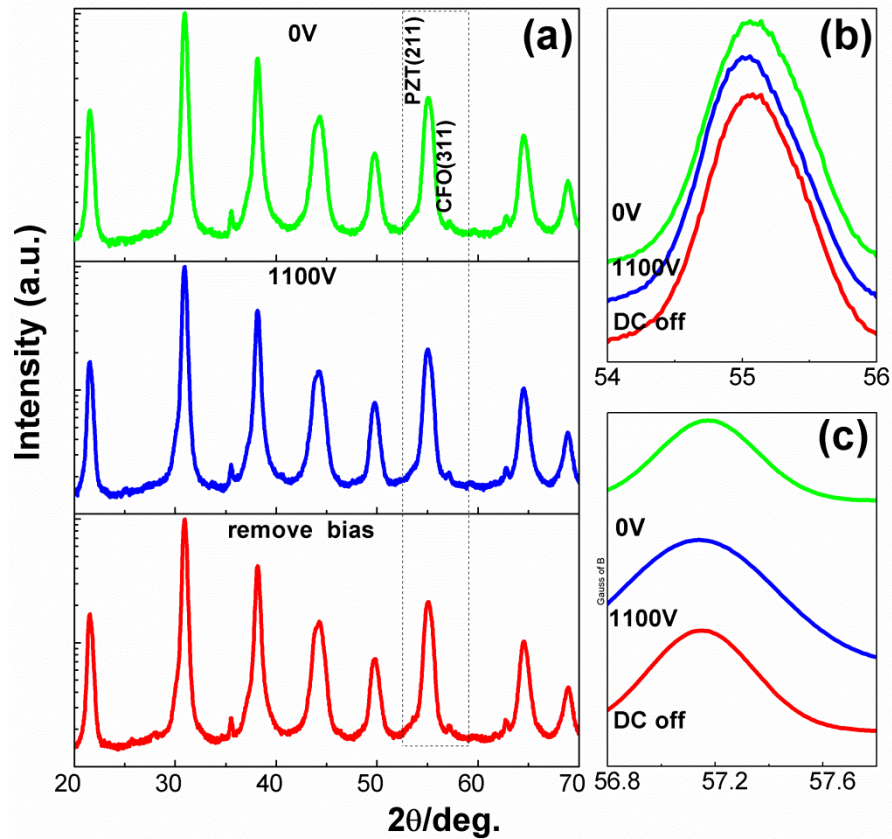


Fig. 3.9 XRD patterns of PZT - CFO ceramic composite during the measurement. (a) 20° - 70° scan, (b) PZT (211) peak and (c) CFO (511) peak.

This strain within PZT observed in the XRD pattern is in good accordance with that calculated from the converse piezoelectric effect (11.98×10^{-4}) via the piezoelectric equation below:

$$S_3 = d_{33}E \quad (3-7)$$



where S_3 is the induced strain in the direction normal to the sample's surface, E the electric field which can be calculated with the applied DC bias V_3 and the thickness of the sample t , and d_{33} is measured as 183 pC/N for our 0-3 type PZT - 0.05CFO composite.

To verify the calculated strain in CFO, we suppose two simple connecting modes of PZT and CFO phases, series connection (Maxwell - Wagner two-layer Model) and parallel connection (or Rheuss model) in Fig. 3.10, to estimate the strains of them. In the parallel connection, the strain of the two phases is equal. That is:

$$\frac{S_{\text{CFO}}}{S_{\text{PZT}}} = 1 \quad (3-8)$$

In the series connection, the stress of the two phases equals. According to Hooke's law, we have:

$$\frac{S_{\text{CFO}}}{S_{\text{PZT}}} = \frac{E_{\text{PZT}}}{E_{\text{CFO}}} = 0.41 \quad (3-9)$$

where E is the Young's modulus ($E_{\text{CFO}} = 17.34 \times 10^{10}$ Pa, $E_{\text{PZT}} = 7.1 \times 10^{10}$ Pa), and S is the strain.

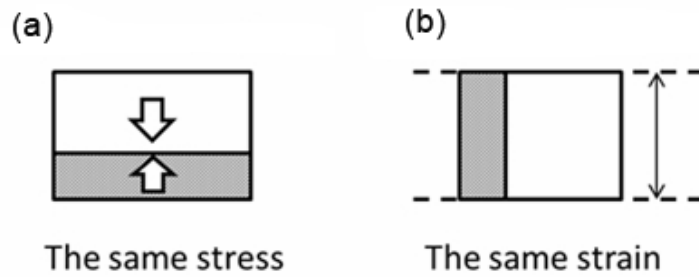


Fig. 3.10 Two connection modes. (a) series connection and (b) parallel connection.

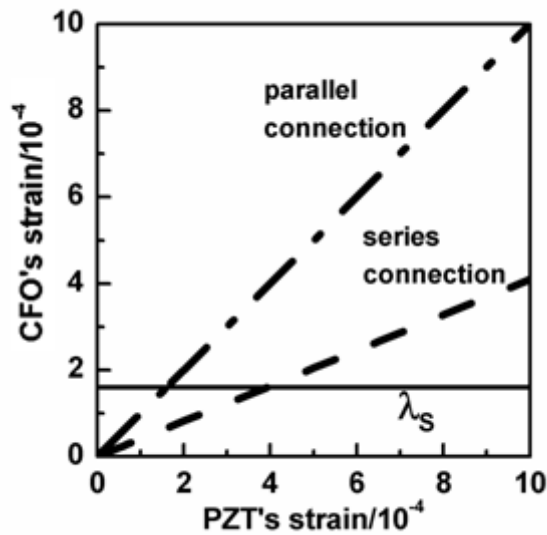


Fig. 3.11 The relationship between CFO's strain and PZT's strain under ideal series connection and parallel connection.

The relationship between CFO's strain and PZT's strain under ideal series and parallel connection is given in Fig. 3.11. What attracts special attention is that when the strain within CFO is larger than its saturated magnetostriction, λ_s , its magnetization will not increase though the strain increases. In a real 0 - 3 type composite sys-



tem, the two component phases are in combined hybrid connection of parallel and series, and the ratio of strain in CFO and PZT should be between 0.41 and 1. This is in good agreement with our sample ($S_{\text{CFO}} : S_{\text{PZT}} = 0.77$).

3.7 Derivation of magnetoelectric coefficient based on coupled lattice strain

3.7.1 Strain-field relationship in PZT and CFO

Based on the coupled lattice strain of the components in the composite, the ME coupling coefficient can be estimated. First we should begin with a universal condition. For a PZT - CFO ME composite, when a magnetic field, H , is applied along its poling direction, the magnetostrictive strain along the direction of H within CFO is:

$$S_{\text{CFO}} = \frac{3}{2} \lambda_s \left(\frac{M}{M_s} \right)^2 = \frac{3}{2} \lambda_s \left(\frac{\chi_m H}{M_s} \right)^2 \quad (3-10)$$

where λ_s is the saturated magnetostrictive constant, M the magnetization, M_s the volume saturated magnetization, χ_m the magnetic susceptibility (this value is not a constant because CFO is ferrimagnetic) and H is the magnetic field intensity. Eq. (3-10) is only suitable for a condition when the magnetostriction does not exceed the saturated magnetostriction, otherwise, the magnetization should be equal to the saturated value and the derivative should be zero. The strain in CFO will cause a coupled strain, S_{PZT} , within PZT through mechanical interaction. S_{PZT} is in the same direction as



S_{CFO} , and its value follows the piezoelectric equation:

$$S_{\text{PZT}} = d_{33}E \quad (3-11)$$

where E is the piezoelectric-induced electric field along the poling direction.

3.7.2 Estimation of the magnetoelectric coefficient in the PZT - CFO composite: a universal condition

To estimate the ME coupling coefficient, we assume two simple connecting modes of PZT and CFO phases: parallel connection and series connection.

When the two phases are in parallel connection, we have $S_{\text{PZT}} = S_{\text{CFO}}$, and the coupling coefficient can be estimated as:

$$dE / dH = \frac{3\lambda_s \chi_m^2 H}{d_{33} M_s^2} \quad (3-12)$$

When they are in series connection, we have $S_{\text{PZT}} E_{\text{PZT}} = S_{\text{CFO}} E_{\text{CFO}}$ and the coupling coefficient is:



$$\frac{dE}{dH} = \frac{3\lambda_s \chi_m^2 H E_{\text{CFO}}}{d_{33} M_s^2 E_{\text{PZT}}} \quad (3-13)$$

where E is the Young's modulus ($E_{\text{CFO}} = 173.4$ GPa, $E_{\text{PZT}} = 71$ GPa). In general, the incomplete coupling of two components in a real material system could be caused by defects, loss and random orientations of the grains and etc. Therefore a coupling factor k ($0 \leq |k| \leq 1$) should be added into Eqs. (3-12) and (3-13) to describe a real composite system, such as:

$$\left. \frac{dE}{dH} \right|_{\text{real}} = k \left. \frac{dE}{dH} \right|_{\text{theory}} \quad (3-14)$$

In Eq. (3-14), the theoretical values should be calculated with Eqs. (3-12) and (3-13). Here, we use Eqs. (3-12) and (3-13) to estimate the minimum and maximum values of ME coefficient under the condition that CFO has not achieved its saturated magnetostriction. When the magnetostrictive phase becomes saturated, a further increase in the magnetic field should not be able to excite a larger strain within CFO, and the electric output will remain constant despite an increase in input H , resulting in a sharp fall of the coupling coefficient to zero. Also, if there is strong coupling around the particles, this value should be multiplied by the volume fraction of distorted zones which can be estimated with the volume fraction of CFO.



3.7.3 Estimation of the magnetoelectric coefficient in the 0 - 3 type PZT - CFO composite

For a PZT - 0.05CFO composite, we have $f_{\text{CFO}} = 7.1\%$ (volume percentage), $\lambda_s = 110 \times 10^{-6}$, $\chi_m \approx 0.37$ (this value is calculated with the constants supplied in Ref [17]), $M_s = 4.13 \times 10^5$ A/m (this value can be calculated by multiplying the density and the mass saturate magnetization) for CFO, and $d_{33} = 183$ pC/N for the PZT - 0.05CFO composite. Applying these material parameters into Eqs. (3-12) and (3-13), the relationship between the coupling coefficient and the applied magnetic field under ideal series connection and parallel connection can be inferred as shown in Fig. 3.11. It can be seen that for a composite with fixed composition under the same magnetic field, a series connection mode favors a larger ME coupling coefficient than that of a parallel connection mode.

In our 0 - 3 type PZT - CFO sample, the ratio between S_{CFO} and S_{PZT} can be estimated with the XRD result ($S_{\text{CFO}} : S_{\text{PZT}} = 0.77$), then we get:

$$dE / dH = \frac{3\lambda_s \chi_m^2 H}{0.77 d_{33} M_s^2} \quad (3-15).$$

The calculated results are also plotted in Fig. 3.12. Eq. (3-15) is also an ideal condition, which should be corrected with Eq. (3-14) in order to describe a real material system. We managed to measure the ME coefficient of our sample under a wide range of electric and magnetic fields. It was found that the coupling effect is depen-



dent on test frequency. When under a pseudo-static field condition, the coefficient for the sample is in the order of tens of mV/cm-Oe, which matches well with theoretical estimation if the microstructural complexity of the real sample is taken into consideration. This estimation is also consistent with most of the literature data.

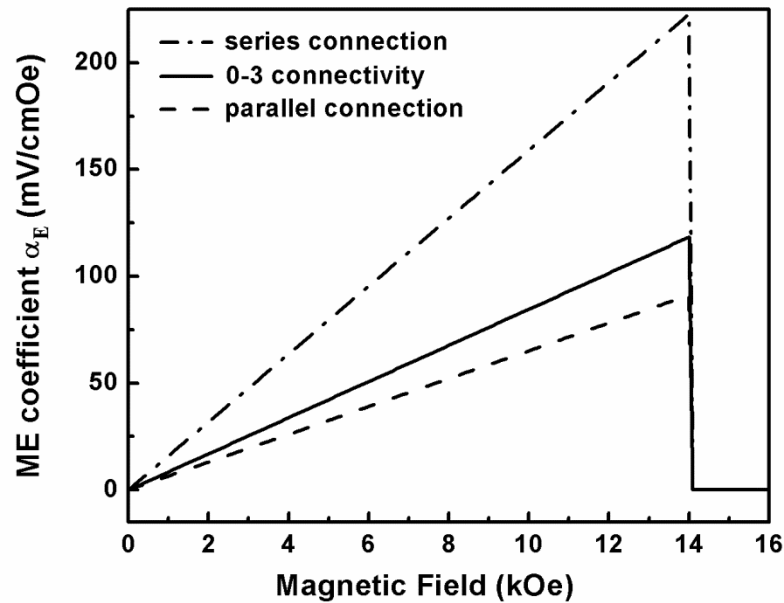


Fig. 3.12 Calculated relationship between ME coupling coefficient and the magnetic field under a static DC bias for PZT - CFO composite with ideal parallel connection, series connection and 0 - 3 type connectivity.

It should be noted that the relationship between the coupling coefficient and the DC magnetic bias is linear in Fig. 3.12. This is under an ideal condition that in all the regions within the composites, the strain ratio between PZT and CFO is of a consistent value. However, in real materials, the strain ratio between these two phases varies everywhere in the composites. This will cause the α_E-H_{DC} curve to be a slow in-



creased into the maximum value, followed by a slow drop to zero in real materials.

3.8 Summary

To summarize, we have investigated the crystalline structure of PZT - CFO particulate composites via XRD measurement and studied the lattice parameter of both components under electric field. The results are outlined as below:

(1) PZT - CFO particulate composites were prepared by conventional ceramic sintering process. According to the microstructure and XRD characterization under no external field, the composites are of high crystalline quality.

(2) When applying a static electric field to the composites, coupled distortion in crystal lattice of the components was observed. The change in lattice parameter under external field gives direct evidence for the mechanical interaction between these two phases. Such finding is the first observed evidence about coupling in 0 - 3 type magnetoelectric composites in the grain lattice scale.

(3) A correlation between lattice distortion and the magnetoelectric coupling effect has been established. Simple models were proposed to estimate the ME coupling coefficient based on the mechanical interaction between CFO and PZT under ideal cases.



CHAPTER 4

Magnetolectric coefficient vs. microstructures in piezoelectric/magnetostrictive composites: A numerical approach

4.1 Introduction

In Chapter 3, we observed that lattice distortion happened when the ME composite was placed under an electric field, which gave a direct evidence about the long-existing assumption that the magnetolectric effect in composites was based on the mechanical interaction between the components. In this Chapter, we try to develop a numerical approach based on finite element analysis method to estimate the magnetolectric effect in any given structures. The core of this approach lies in the mechanical coupling between the piezoelectric phase and the magnetostrictive phase at their interface, and the commercial software COMSOL 3.5a is employed to simulate their interaction. Besides, we develop a method to evaluate the coupling efficiency in composite materials. This method relates the lattice coincidence to the coupling efficiency, and explains existing experimental results in the literature reasonably.

Before the analysis, we need to give a brief introduction of the theoretical work in the literature. There have been continuous efforts to establish the relationship between ME property and composite structure. For example, Harshe and Newnham presented a way to derive the coefficient by assuming a relatively simple cube model, in which the 0 - 3 particulate composites were considered as consisting of small



cubes, and then solved the fields in one cube for which the boundary value problem involved is tractable; [128, 148] Srinivasan *et al* developed a theoretical model for ME coupling in layered magnetostrictive/piezoelectric samples; [46, 70, 83] Bichurin and Petrov developed a generalized effective medium method for calculating the composite ME effect by introducing an interface coupling parameter k for characterizing actual bonding conditions at the interface; [149] Dong *et al* calculated the ME coupling in the dynamic cases with equivalent circuit model; [150] and Nan *et al* gave a model based on Green's function method. [151 - 154]

Apart from these analytical methods, some indirect simulation methods based on commercial software were also introduced to analyze ME composites. For example, Liu *et al* noticed the fact that the constitutive equations of magnetostriction and piezoelectric effect are identical. They used two groups of piezoelectric models (one of which is replaced by the magnetic phase) to analyze the ME effect at resonant frequencies. [155] However, this method is only restricted to simple structures.

Having noticed that, we herein proposed a numerical approach through which the ME coefficient of any given ME system can be predicted (stated in Section 4.2). This approach is based on finite-element analysis method. With this method, the electric response of a composite to an applied magnetic field can be calculated directly, thus giving a clear relationship between output electric field and input magnetic field. Two simple examples are also given to explain the method (Section 4.3). In Section 4.4, we focus on the coupling factor (k_c), the parameter describing the ME interfacial coupling efficiency, which has been discussed in the literature but still lacks an accurate physical understanding. We propose an evaluation method to esti-



mate the value of the coupling factor k_c for composites with any given structures, which explains the existing experimental results reasonably.

4.2 Theory and simulation method

4.2.1 General consideration

The ME effect in composites is generally believed to be achieved through mechanical coupling. That is, the ME coefficient, α , can be expressed as:

$$\alpha = \frac{\partial P}{\partial H} = k_c \frac{\partial P}{\partial S} \frac{\partial S}{\partial H} = k_c e^p e^m \quad (4-1)$$

where H is the externally applied magnetic field, S the mechanical strain exhibited at interface of the two component phases, P the resulting electrical polarization within the piezoelectric phase, e^m and e^p the piezomagnetic and piezoelectric coefficient, respectively, and k_c is defined as the coupling factor describing the elastic coupling between the two constituent phases. In our simulation, we use the magnitude of output voltage (V) to calculate the polarization (P).

4.2.2 Modeling the magnetostrictive effect

The magnetostrictive effect is a sub-problem in ME effect. To the best of our knowledge, in present commercial finite element analysis software, there is no indi-



vidual component to express the magnetostrictive effect. The existing simulations of magnetoelectric effect usually use the linear piezoelectric component in the software to stand for the magnetostrictive effect. Such substitution limit the modeling of ME effect only to composites with simple structures. To express the magnetostrictive effect in complex structures, we need to include it into the software. Our method is given below.

For different kinds of materials, suitable equations should be selected. In magnetostrictive materials, the strain induced by H field can be expressed as:

$$\lambda = dH \quad (4-2)$$

where λ is the strain along the magnetic field, and d is called piezomagnetic strain coefficient. But in reality, the strain and magnetic field has no linear dependence. In our simulation, the magnetic phases are of multi-domains, the magnetic moment orient randomly. In this case, we follow Chikazumi's approach, then the strain along any directions i should be: [156]

$$\lambda_i = \frac{3}{2} \lambda_s \left[\left(\frac{M}{M_s} \right)^2 - \frac{1}{3} \right] \quad (4-3)$$

Here λ_s is the magnetostrictive constant, M the magnetization, and M_s is the saturated magnetization. The negative "1/3" means that the magnetic moments are



randomly oriented in the material when no magnetic fields applied. In our simulation, we don't use "1/3" as we assume the pre-stress is sufficient to align the magnetic moments perpendicular to the direction of magnetization from the beginning. [157]

When the ME composites is placed in an external magnetic field, the two phases behaves according to the magnetostrictive and piezoelectric effect respectively. If physical constraint (e.g., mechanical clamping) exists, the two phases will mechanically interact with each other at the phase boundary till self-consistent. Based on this, our simulation includes not only the two respective effects described in Eq. (4-1), but also a self-consistent method, which means that the magnetic field, deformations and electric field should balance each other. The self-consistent solving process is described in Fig. 4.1, which is expanded from Mudivarthi's sketches. [158] The final solution should pass all 3 convergent tests.

4.2.3 Numerical approach

The software COMSOL (version 3.5a) is employed in simulation. We expand a magnetostriction example supplied by the COMSOL group to solve the ME effect. COMSOL cannot simulate magnetoelectric or magnetostriction directly, so the "multiphysics mode" of this software is used to do it. As shown in Fig. 4.1, three application modes should be added into this model: magnetic analysis, solid analysis, and piezoelectric analysis, among them the first two are for magnetostriction simulation.

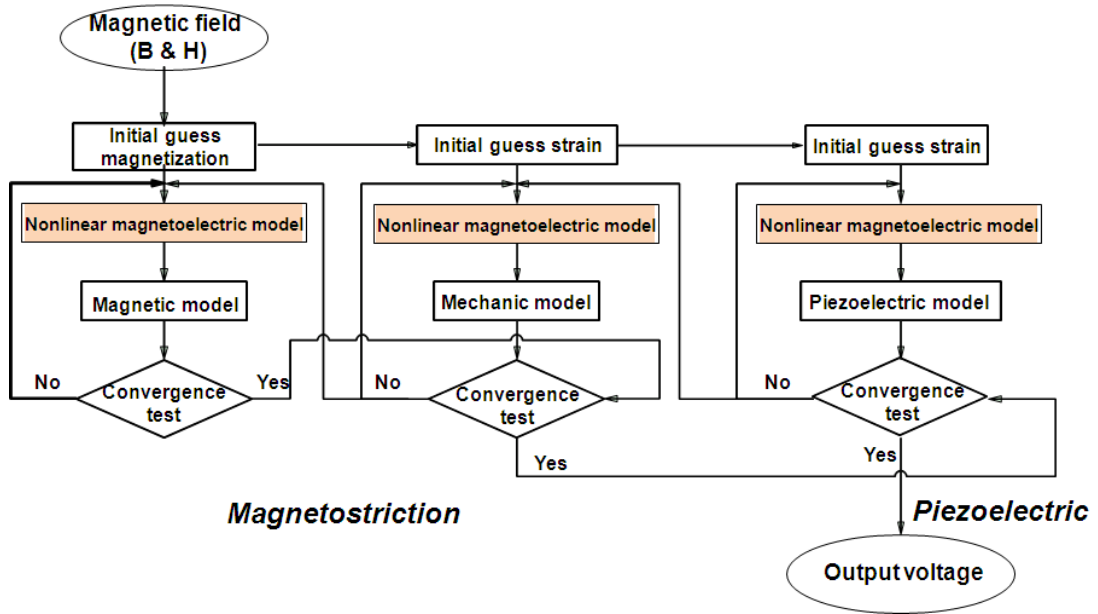


Fig. 4.1 The process of the self-consistent process.

4.2.4 Simulation process

The simulation process is described as follow:

(1) As we only simulate the static state of the ME composites, at the beginning, three static modes should be added into a blank COMSOL project: “magnetostatics - no currents” (which is in the AC/DC module group), “solid stress - strain - static analysis” (which is in the structure mechanic module group), and “piezo solid - static analysis” (which is also in the structure mechanic module group, and the piezoelectric effect sub group).

(2) When designing the structures for simulation, a big bulk shape which is corresponding to the air in the environment which is used to offset the boundary effect should be added to cover the whole structure usually. Then the whole structure can



be separated into three kinds of subdomains: magnetic phase, piezoelectric phase, and air phase. The three application modes should be active or not in different subdomains after designing: the “piezo solid mode” must be active in subdomains which stand for piezoelectric phases, but it should not be active in other domains. The “solid stress - strain mode” must be active in magnetic domains, but not for others. The “magnetostatics mode” is different; sometimes this mode should be active in all domains, as the magnetic field exists everywhere usually.

(3) In the “magnetostatics mode”, the relationship \mathbf{B} vs. \mathbf{H} (bold letters mean vector) is the most important property. Simply, the following two formulas are commonly used:

$$\mathbf{B} = \mu_0 \mu_r \mathbf{H} \quad (4-4)$$

$$\mathbf{B} = f(|\mathbf{H}|) \mathbf{e}_H \quad (4-5)$$

Eq. (4-4) is very basic and can be used in most of nonmagnetic phases (air and piezoelectric phases in this model). In Eq. (4-4), \mathbf{e}_H presents the unit vector along the \mathbf{H} field, this formula is often used for magnetic phases, as the magnetization (\mathbf{M}) of most of the magnetostrictive materials is nonlinear to \mathbf{H} field. This relation can be taken from the experimental data, and be set in “functions” in COMSOL options.

(4) In the “solid stress - strain mode”, the Young’s modulus, Poisson’s ratio, and density should be typed in. Also, the strains root in the magnetostriction must be set



somewhere, because this is the key to combine magnetic and mechanics into magnetostriction. In this project we follow COMSOL group's advice, [157] and set the strains as initial value in this mode.

(5) In the “piezo solid mode”, the piezoelectric tensor and mechanical properties are needed. Sometimes to import them from the materials library in COMSOL and add modification is enough.

(6) Suitable boundary conditions which should be corresponding to the experiments should also be set for each mode. Static magnetic field can be obtained by setting the magnetic potential in magnetic mode boundary conditions of air environment. After solving the model, the boundary integration (COMSOL provides this function) of electric potential on the top surface will be calculated, to get the average value of the voltage.

(7) The “nonlinear solving method” should be appointed as this is a nonlinear and self-consistent problem.

4.3 Results and discussions

To verify the feasibility and accuracy of our method, we use two typical structures in ME composites to explain the modeling process of our method. In the two composites, we use CoFe_2O_4 (CFO) as the magnetostrictive phase and PZT-5H as the piezoelectric phase.



4.3.1 1 - 3 composite

As shown in Fig. 4.2 (a), the 1 - 3 type ME composite is structured with 9 piezoelectric rods (painted in pink, cylindrical rods with radius of 0.1 cm) arrays embedded in a magnetic cubic matrix. The size of the magnetic cube is set as $1 \times 1 \times 1 \text{ cm}^3$, and the distance between the nearest two piezoelectric rods is 0.25 cm. The volume percentage of the piezoelectric phase in this model is 28 %. All the PZT-5H rods are poled along the z axial direction. Mechanical and electric boundaries are set to both the bottom and top surfaces of the sample. The bottom surface is fixed and grounded, while the top surface is fixed with a free electric boundary. In simulation, we apply a H field ($0 \sim 4 \times 10^5 \text{ A/m}$) perpendicular to the top and bottom surfaces of the composites, and a gradient distribution of electric potential can be observed from within the piezoelectric rods, which described the excited electric polarization by H . Fig. 4.2 (b) gives the distribution of electric potential within the matrix at a saturated magnetization, and the corresponding displacement of each mass point within the magnetic phase (which performs the level of deformation) is shown in Fig. 4.2 (c). The deformations inside the piezoelectric rods are almost symmetric, the upper half and the lower half press to each other, and the center almost does not displace. The deformations of magnetic phase are focused near the boundaries inside the cube; they press the piezoelectric rods to produce the electric field inside them.

The averaged electric potential output is estimated by integrating the electric potential on the top surface. From this, the electric field output and the magnetoelectric coefficient can also be derived. Fig. 4.2 (d) gives the electric field output at different magnetic fields, and Fig. 4.2 (e) gives the corresponding magnetoelectric coef-



ficients (dE/dH). In both figures, the magnetoelectric response shows a great dependence on the magnetic field, which is dominated by the bias-dependent magnetostriction. In the low field range, dE/dH increases approximately linearly with the increasing H field, due to the increasing magnetostriction as described in Eq. (4-5). At high magnetic field, the magnetostriction becomes saturated producing a nearly constant electric field in the PZT-5H rod, thereby decreasing the value of dE/dH . This variation trend given in Fig. 4.2 (e) is in good accordance with those reported in the literature for magnetoelectric composites. [94,159]

The maximum ME coefficient of this composite is found at $H = 2.25$ kOe, with $dE/dH = 70$ mV/cm·Oe. According to the experimental results reported in 1 - 3 type PZT - Terfenol-D/epoxy composites[159], the largest ME coefficient in 1 - 3 type PZT/Terfenol-D composites was 280 mV/cm·Oe at 2 kOe for the sample with PZT's volume fraction as 0.12. The magnetoelectric coefficient obtained in our simulation is comparable to that reported in literature when taking the CFO's relatively small magnetostriction ($\lambda_{s, \text{Terfenol-D}} = 1080 \times 10^{-6}$, $\lambda_{s, \text{CFO}} = -110 \times 10^{-6}$) into account.

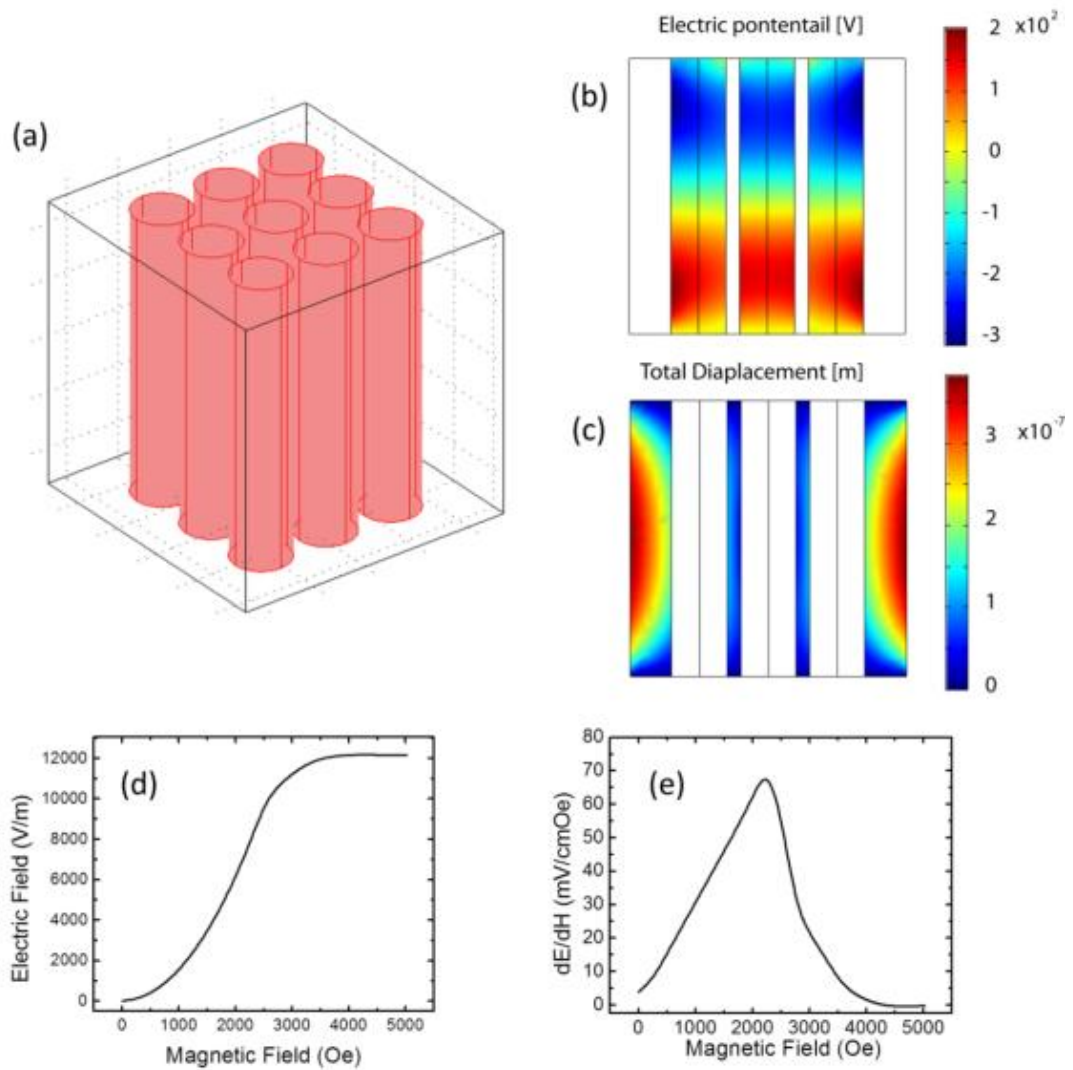


Fig. 4.2 Simulation results for the 1 - 3 type PZT - CFO composite. (a) The geometric construction of the structure; (b) The distribution of electric potential, and the slice is along the center of the structure; (c) The total displacement of CFO matrix; (d) Output electric field vs. input magnetic field; (e) dE/dH vs. input magnetic field.

4.3.2 0 - 3 composite

The other example is a 0 - 3 type composite with CFO particles randomly dispersed in PZT-5H particles, which is a typical ME ceramics synthesized by direct



mechanical mixing of the two-phase powders. We simplify such a structure by a model with 125 CFO particles (sphere, with radius of 0.062 cm, and the volume about 0.001 cm^3) randomly embedded in the PZT-5H matrix (cubic, with the edge length of 1 cm). Accordingly, the volume percentage of the magnetic phase in this model is 12.5 %, which is also the most commonly used volume fraction in experiments. The magnetic field range and the boundary conditions are the same as the previous example.

To simulate the random distribution of the magnetic particles in a co-fired ceramic sample, a Monte - Carlo method is introduced to generate random coordinates of the particles. Such a generation and solving process should be repeated for hundreds of times at least, and the averaged value is used to describe the property of the material.

Fig. 4.3 (a) shows the particle distribution generated in one of the simulations. The electric potential distribution and the deformations within the PZT-5H matrix are shown in Figs.4.3 (b) and (c), respectively. From them we are informed that, the top and bottom near the particles should be the key regions in this 0 - 3 composite system. As shown in Figs.4.3 (b) and (c), the electric potential and the deformations change sharply near the top and bottom of the particles, which is reasonable because of the sharp deformations there. Also, from Fig. 4.3 (d) which shows the deformations of the particles near the center slice, we know that the deformations inside the particles are also sharp on the top and bottom sections.

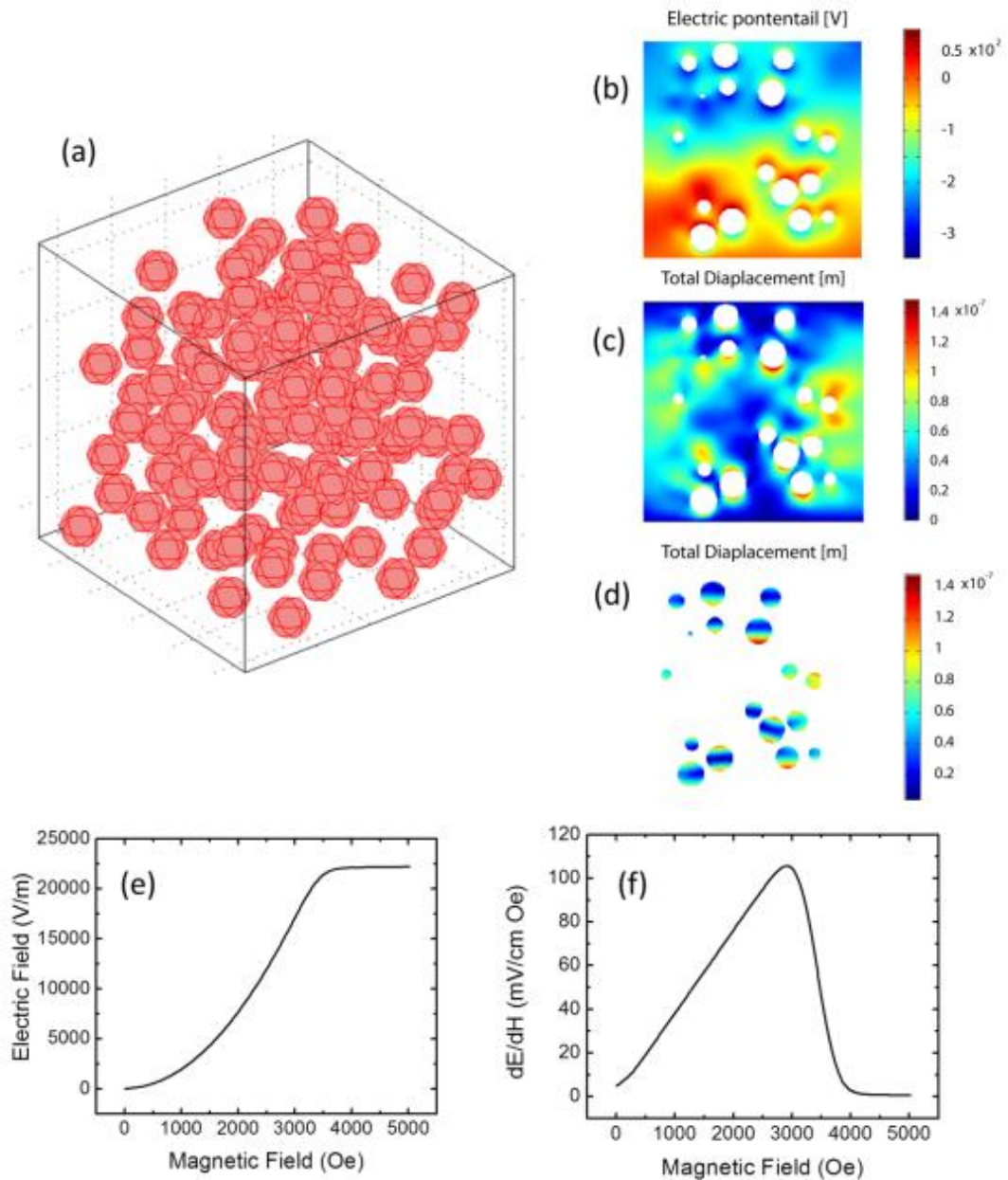


Fig. 4.3 Simulation results for the 0 - 3 type PZT - CFO composite. (a) The particles distribute in the matrix randomly, and the figure gives the result in one of the simulations; (b) The distribution of electric potential on center of the slice of piezoelectric solid in one of the simulations; (c) The total displacement of piezoelectric matrix; (d) The total displacement of magnetic particles; (e) Output electric field vs. input magnetic field; (f) dE/dH vs. input magnetic field.



After repeating the simulation for hundreds of times, we get the field dependence of averaged E and averaged dE/dH in Figs. 4.3 (e) and 4.3 (f). Both curves have similar variation trends as those in 1 - 3 type composites. This field-dependent magnetoelectricity is also in good accordance with literature. The maximum magnetoelectric coefficient in the 0 - 3 type model is 105 mV/cm·Oe at $H = 3$ kOe. According to the literature, the low-frequency ME coefficients of the sintered 0 - 3 composite ceramics vary from about 10 to 100 mV/cm·Oe depending on compositions, powders used, and processing. [115, 160 - 167] Our model deals with an ideal condition and is thus reasonable.

4.3.3 A short discussion

In this Section, we give a theoretical explanation about the variation trends in the $\alpha_E - H$ relationship in ME composites.

As stated in Eq. (4-3), the magnetostrictive strain λ is a function of the magnetization M . It should be noted that the strain obtained by Eq. (4-3) is an averaged value. When the strain calculated via this equation is minus, the actual magnetostriction is zero in the real material. On the other hand, as the magnetization M has a value no larger than the saturated magnetization M_s , the maximum magnetostrictive strain is 1. To summarize, the magnetostriction (λ) in real material values in the range of $\lambda \in [0, 1]$.

In order to get the magnetostriction in the magnetic materials, we will discuss the magnetization M first. Generally, in linear material, we have:



$$\vec{B} = \mu_0 \mu_r \vec{H} \quad (4-6)$$

In the magnetoelectric composites, the piezoelectric phase can be considered with a relative permeability of 1, and the influence of magnetic field on its behavior can be omitted.

During the measurement of magnetoelectric coefficient, a magnetic field is applied to the composite. According to the magnetic hysteresis loop ($M - H$ loop), the $M - H$ relationship can be expressed as:

$$M = \begin{cases} M_r + \frac{M_s - M_r}{H_s} H & (H < H_s) \\ M_s & (H \geq H_s) \end{cases} \quad (4-7)$$

Taking Eq. (4-7) into Eq. (4-3), the magnetization can be obtained as:

$$\lambda_i = \frac{3}{2} \lambda_s \left[\left(\frac{M_r}{M_s} + \frac{M_s - M_r}{M_s H_s} H \right)^2 - \frac{1}{3} \right] \quad (4-8)$$

From Eq. (4-8), one can get a conclusion that the strain of the magnetic phase (λ) is a quadratic function of the magnetic bias (H). As discussed in Chapter 3, the strain of the piezoelectric phase (poled) is proportional to the strain of the magnetic phase, and the excited electric field by the piezoelectric phase is also proportional to its



strain. Then we can get a conclusion that the induced electric field (E) is proportional to the strain of the magnetic phase. Suppose the coefficient of this proportionality is t , we have:

$$E = k\lambda_i = \begin{cases} 0 & 0 \leq H < \sqrt{c/a} - b \\ a(H+b)^2 - c & \sqrt{c/a} - b \leq H < H_s \\ k\lambda_s & H \geq H_s \end{cases} \quad (4-9)$$

It should be noted that when the electric field calculated via Eq. (4-9) is minus, the real field intensity should be zero. One can see that as the magnetic field increases, the induced electric field by the ME composite increases first, and then keeps at a constant value when the applied magnetic field (H) exceeds the saturated field (H_m). While in the ME measurement, the magnetoelectric coefficient (α_E) is the derivative of Eq. (4-9). So we can expect the measured α_E to start from zero first, and then increase linearly with the increase of H . After reaching its maximum value at H_m , the value of α_E will decrease sharply though H continues to increase. As the real material are non-uniform in microstructure (i.e., H_m varies in local regions of the magnetic phase), the falling part of the $\alpha_E - H$ curve turns to be with a small gradient, which is common in the experimental results. [e.g., Fig. 1.10]



4.4 Evaluating the coupling efficiency

In the qualitative expression of ME effect (see Eq. (1-4)), an interfacial coupling factor, k_c , is used to define the coupling efficiency between the magnetic and piezoelectric phases. For a given material system with fixed piezoelectric and magnetostrictive properties (expressed in the form of $\frac{\partial P}{\partial S}$ and $\frac{\partial S}{\partial H}$), the value of k_c is a key factor determining the ME coefficient α . Former researchers have tried to reveal the relationship between interfacial coupling factor k_c and the selection of the piezoelectric/magnetostrictive phases through experiments. [46, 70, 110] The result showed that NiFe_2O_4 provides an ideal interfacial coupling with PZT ($k_c = 1$); while $\text{La}_{0.7}\text{Sr}_{0.3}\text{MnO}_3$, $\text{La}_{0.7}\text{Ca}_{0.3}\text{MnO}_3$, and CoFe_2O_4 exhibit poor coupling ($k_c \leq 0.1$). This work provide an evidence that the coupling factor k_c is relevant to the selected material in the composites, while it still cannot explain the fact that with the same component, 2 - 2 type composites exhibited a much larger coupling coefficient than 0 - 3 type composites.

In this Section, we give a universal method to evaluate the interfacial coupling factor, k_c , between any two components in ME composites. This method is also applicable to describe any binary composite systems in which the coupling is realized by mechanical interaction at the interface.

4.4.1 Lattice coupling at the interface

As mentioned before, the magnetic - electric energy transfer is realized through



the mechanical interaction at its component interfaces. The efficiency of mechanical energy transfer at the interface will influence the coupling coefficient directly. To investigate the interfacial mechanical energy transfer efficiency, we will consider one single interface between any two lattices first.

Fig. 4.4 gives three kinds of typical interfaces in composites. In an ideal condition shown in Fig. 4.4 (a), the two lattices are of the same orientation and lattice parameter at the interface. This makes the two phases act like one single body from the view of mechanical interaction. Then the strain can transfer from one phase to the other at the efficiency of 100 % and no energy loss happens. When the two phases are of different lattice parameters (i.e., a size mismatch exists, like Fig. 4.4 (b)) or of different lattice orientations (i.e., orientation mismatch exists, like Fig. 4.4 (c)) at the interface, the two phases have to distort their lattices at the interfacial regions in order to suit each other. In the process of lattice distortion, the lattice grains slip across each other and energy dissipates in the form of frictional heat. Consequently, the coupling between the phases is expected to be extremely strong in Fig. 4.4 (a) as no energy loses, while weak in Figs. 4.4 (b) and (c) due to energy dissipation.

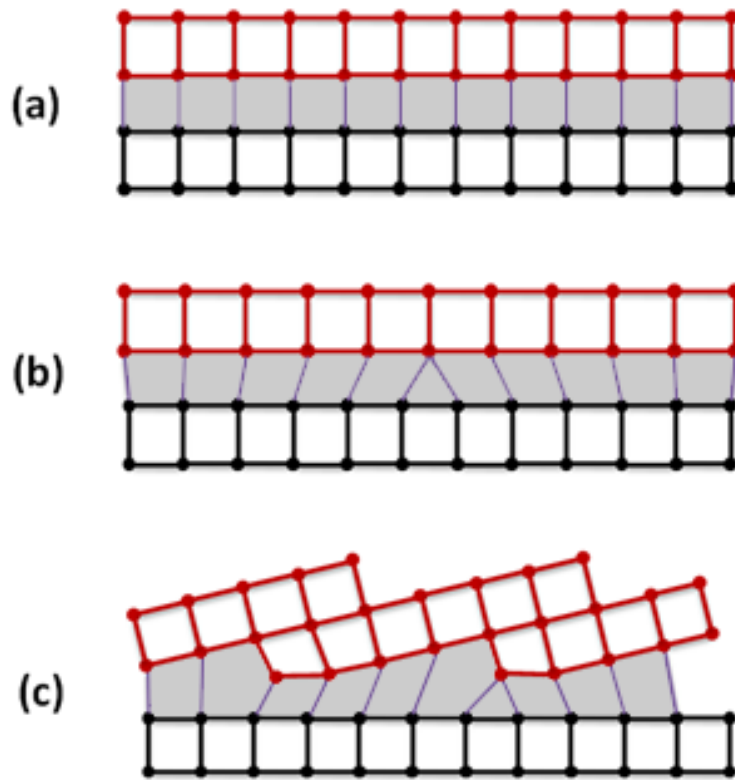


Fig. 4.4 Lattice coupling models at the interface.

4.4.2 Coupling efficiency in two sets of lattices

The coupling efficiency in any two sets of lattices with varied lattice parameter and orientations can be evaluated by the coincidence of lattice sites (marked as e), which can be identified to the intersection area of two lattice functions.

Simply, we first consider the 1D composite. According to the probability theory, the positions of lattice sites are broadening with normal distribution, which can be expressed as [168] :



$$f(x) = \sum_i \frac{1}{\sigma\sqrt{2\pi}} e^{-\frac{(x-u_i)^2}{2\sigma^2}} \quad (4-10)$$

where u_i is the expectation, and σ is the standard deviation. Then for any two sets of 1D lattices with their lattice functions marked as f_1 and f_2 respectively, the coincidence, e , can be obtained:

$$e = \lim_{S \rightarrow \infty} \frac{1}{S} \iint_S \min(f_1(x), f_2(x)) dx \quad (4-11)$$

where S means the contacting area. As the integrations of f_1 and f_2 are infinite, the result is divided by the contacting area to make it a finite value.

Fig. 4.5 gives a schematic explanation about the lattice coincidence. In Fig. 4.5 (a), the two lattices are of the same arrangement with equal distribution function, i.e., $f_1 = f_2$. Consequently, the lattice coincidence, e , achieves a value of 100 %, indicating large coupling efficiency between the components. As a contrast, in Fig. 4.5 (b), the two phases has varied lattice parameters, inducing a small coincidence area in their lattice functions, i.e., $e \ll 1$. As a result, small coupling coefficient can be expected.

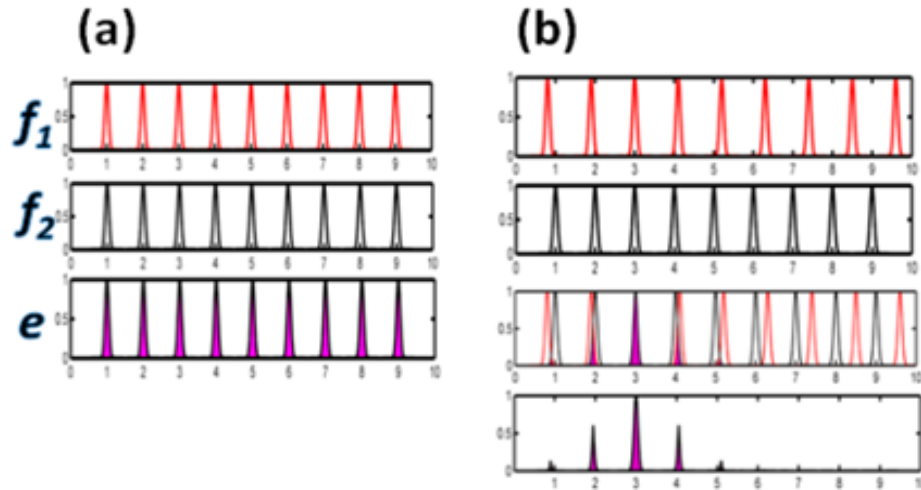


Fig. 4.5 Lattice coupling between two sets of 1D lattices.

Similarly, we can also obtain the lattice function (f) and lattice coincidence (e) between given 2D and 3D lattices. That is:

For 2D lattices, [168]

$$f(x) = \sum_{\substack{\text{Lattice} \\ \text{Sum}}} \frac{1}{\sigma^2 2\pi} \exp \left[\frac{(x-x_i)^2 + (y-y_i)^2}{-2\sigma^2} \right] \quad (4-12)$$

$$e(f_1, f_2) = Z \lim_{S \rightarrow \infty} \frac{1}{S} \iint_s \min[f_1(x), f_2(x)] dx \quad (4-13)$$

where we introduce Z as the uniform factor which makes the value of e on the closed packed surface equals to 1 and can be calculated first of all.

For 3D lattices, considering one unit cell only contains one lattice site, the func-



tion f can be expressed as a 3D normal distribution [168]:

$$f(\vec{r}) = \sum_{\substack{i \\ \text{in crystal}}} \frac{1}{\sigma^3 (2\pi)^{3/2}} \exp\left(-\frac{\|\mathbf{r} - \mathbf{u}_i\|^2}{2\sigma^2}\right) \quad (4-14)$$

$$e(f_1, f_2) = Z \lim_{S \rightarrow \infty} \frac{1}{S} \iint_S \min[f_1(x), f_2(x)] dx \quad (4-15)$$

where $\mathbf{r} = (x, y, z)$ means the coordinate vector of one point, and \mathbf{u}_i is coordinate vectors describing the positions of lattice sites.

4.4.3 Coupling efficiency in polycrystalline materials

In Section 4.4.2, we obtain the lattice function and lattice coincidence between two sets of lattices. In this Section, we will discuss the coupling efficiency between two polycrystalline materials, such as ceramics. In such materials, the grains are in random orientations. The composite can be considered as a structure with two kinds of lattices distributed randomly in large number.

The orientation of one single grain can be described by a sets of Euler angles, marked as α , β and γ , which stands for the rotation angle around the axis of z , x , and z respectively. More specifically, a rectangular Cartesian coordinate system is first rotated by α about the z axis, then it is rotated by β about the x axis, and finally it is



rotated by γ about the z axis. The valid ranges for α and γ are both $(0, 2\pi]$ and that for β is $(0, \pi]$. The rotation matrix, R , can be expressed as:

$$R = \begin{pmatrix} \cos \gamma & \sin \gamma & 0 \\ -\sin \gamma & \cos \gamma & 0 \\ 0 & 0 & 1 \end{pmatrix} \begin{pmatrix} 1 & 0 & 0 \\ 0 & \cos \beta & \sin \beta \\ 0 & -\sin \beta & \cos \beta \end{pmatrix} \begin{pmatrix} \cos \alpha & \sin \alpha & 0 \\ -\sin \alpha & \cos \alpha & 0 \\ 0 & 0 & 1 \end{pmatrix}$$
$$= \begin{pmatrix} \cos \alpha \cos \gamma - \cos \beta \sin \alpha \sin \gamma & \sin \alpha \cos \gamma + \cos \beta \cos \alpha \sin \gamma & \sin \beta \sin \gamma \\ -\cos \alpha \sin \gamma - \cos \beta \sin \alpha \sin \gamma & -\sin \alpha \sin \gamma + \cos \beta \cos \alpha \sin \gamma & \sin \beta \cos \gamma \\ \sin \beta \sin \alpha & -\sin \beta \cos \alpha & \cos \beta \end{pmatrix}$$

(4-16)

Then for a given lattice point with its coordinate \mathbf{r} in the lattice, we have its new coordinate \mathbf{r}' after rotating, i.e.,

$$\mathbf{r}' = R\mathbf{r} \quad (4-17)$$

Consequently, the new lattice function and the lattice coincidence can be obtained, both of which are a function of the three rotation angles (α , β , and γ). We mark them as $f(\mathbf{r}, \alpha, \beta, \gamma)$ and $e_{f1, f2}(\alpha_1, \beta_1, \gamma_1, \alpha_2, \beta_2, \gamma_2)$.

Collecting all orientations in the space of Euler angles, the averaged coincidence in the whole polycrystalline material, E , can be obtained:



$$E = \frac{1}{64\pi^4} \int_0^{2\pi} \int_0^\pi \int_0^{2\pi} \int_0^{2\pi} \int_0^\pi \int_0^{2\pi} e(\alpha_1, \beta_1, \gamma_1, \alpha_2, \beta_2, \gamma_2) \sin \beta_1 \sin \beta_2 d\alpha_1 d\beta_1 d\gamma_1 d\alpha_2 d\beta_2 d\gamma_2$$

(4-18)

where two sine functions in integrand are the measures of Euler angles, and $1/64\pi^4$ is the normalized factor of the two groups of Euler angles (The normalized factor of one group of Euler angle is $1/8\pi^2$). Based on Eq. (4-18), the averaged coincidence of 0 - 3 type PZT - ferrite ME composites can be calculated as $E_{\text{ceram}} \approx 0.0231$ (σ is set as 10 % of the lattice parameter in the calculation). This indicates a small coupling efficiency of 0 - 3 connectivity,

To summarize, a method to evaluate the coupling efficiency between given lattices are provided in this Section. Through this method, we evaluated the coupling efficiency of 0 - 3 type ceramic composites. The result showed that the small coincidence caused by random lattice orientation is the reason accounting for the low coupling coefficient in particulate composites.

4.5 Summary

A self-consistent numerical method to simulate the static response of ME composites has been developed. With this method, the relations between output electric field and input magnetic field can be simulated directly. Two examples with typical 1 - 3 and 0 - 3 type structures were given, and the simulated results, including both ME



coefficients and its dependence on the magnetic fields, is in good agreement with the reported experimental results in the literature. This method is also applicable to simulate the static ME response for composites with any designed structures.

Besides, a method is developed to evaluate the coupling efficiency of given composite systems. By taking the influence of random grain orientation and lattice matching into account, this theoretical method explains the existing experiment result of ME coupling effect reasonably.



CHAPTER 5

Study on the influence of microstructural inhomogeneity on magnetoelectric effect

5.1 Introduction

Previous researchers have tried to investigate the relationship between microstructural inhomogeneity (such as porosity, grain size, etc.) and ME coupling properties. These studies mostly focused on the microstructural morphology of the composite, while little attention is paid to the microstructural material performance of the composites.

Take the piezoelectric component as an example. Its piezoelectric behavior is highly dependent on the poling voltage and working field. At the same time, the components in ME composites are mostly of distinctive electric properties, which induces distorted internal electric field upon a given electric field. Such electrical field non-uniformity may affect the performance of the composite, which is not discussed in detail in the literature.

In this Chapter, we will take 0 - 3 type $\text{Pb}(\text{Zr}, \text{Ti})\text{O}_3 - \text{CoFe}_2\text{O}_4$ composites as an example, and start from the local electric field within the composites. The internal field within the piezoelectric phase under an external field was studied via the finite element analysis method in Section 5.3. And then, the influence of inhomogeneous internal field on the poling process (Section 5.4) and the converse magnetoelectric effect (Section 5.5) are studied.



5.1.1 Electric-field-related process in 0 - 3 type ME composites

The preparation and application of ME composites is closely related to electric field. Two process includes:

(1) Electric poling. During this process, the (heated) composite is placed under a high DC electric field (E_{poling} , mostly in the order of \sim kV/mm), so that the electric dipoles can be forced to align in the same direction. When the electric field is removed, the dipoles remain fairly aligned, although there will still be some element of random direction. [167, 169 - 170] The illustration of the state of electric dipoles before, during and after poling is shown in Fig. 5.1.

(2) Application of CME (converse magnetolectric) effect. In this case, the composite is supposed to work under external electric field (E_{apply} , mostly containing an AC component).

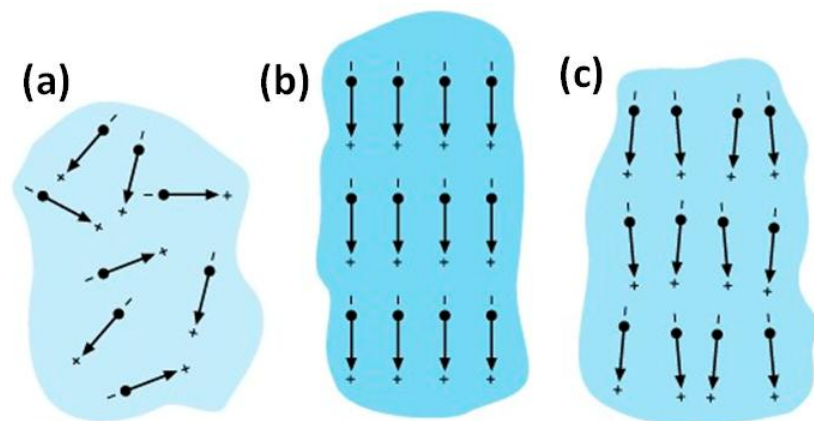


Fig. 5.1 The electric dipoles in piezoelectric material. (a) Before (ferroelectric ceramic), (b) during and (c) after poling (piezoelectric ceramic).



5.1.2 Previous solution to the inhomogeneous microstructural property

The inhomogeneous microstructural electric field is caused by the low resistivity of the magnetic phase. As discussed in Chapter 1, possible conductive percolation path formed by these conducting magnetic particles makes it difficult to polarize the composites and causes the charges developed in the piezoelectric phase to leak through the path. Though the electric breakdown of the composites under electric field could be avoided to some extent by decreasing the magnetic phase content or microstructural modification [171 - 173], the inhomogeneous internal electric field may still give rise to inhomogeneous piezoelectric property throughout the composites via the poling process.

Such inhomogeneous material property has been included into some previous theoretical predictions of magnetoelectric effect, mostly using an averaged method. For example, Nan developed the Green's function technique [33, 174] and derived the effective properties of the composites, defined in terms of averaged fields. All effective properties of the composites could be obtained by this approach. Although these methods using effective properties worked efficiently in predicting magnetoelectric effect, there still lacks a specific discussion about the influence of inhomogeneous material property on the magnetoelectric coupling effect.

5.2 The inhomogeneous electric field in 0 - 3 type composites

In this Section, we develop a unit model to analyze the inhomogeneous microstructural electric field within 0 - 3 type composite theoretically.



5.2.1 Origin of the inhomogeneous electric field in ME composites

First, we consider the electric field distribution in two types of composites under applied voltage, as illustrated in Fig. 5.2. The first type is the composite containing no conductive particles, with its local field intensity and direction shown in Figs. 5.2 (a) and 5.2 (c), respectively. Like any single-phase insulating materials, a uniform electric field (including intensity and direction) is found throughout this composite. As a contrast, if there are some dispersed conductive particles within the composite as shown in Figs. 5.2 (b) and 5.2 (d). The local electric field will be distorted dramatically around these particles, and inhomogeneity is induced in both local field intensity and direction. Obviously, the ME composites is a composite system sorted into the second type in Fig. 5.2 due to the distinctive electric properties of its components.

Table 5-1 gives the electrical resistivity of frequently used materials in ME composites. The piezoelectric phases, PZT [175 - 177] and PVDF [178] are non-conducting materials, with their resistivity as large as $10^{12} \sim 10^{14} \Omega\cdot\text{cm}$ (in order). However, the magnetostrictive phase behaves totally different.

The magnetostrictive alloy Terfenol-D ($\text{Tb}_{0.3}\text{Dy}_{0.7}\text{Fe}_{2-x}$, $x = 0.05 - 0.10$) [179, 180] is electrically conductive with its resistivity as small as $\sim 10^{-6} \Omega\cdot\text{cm}$.

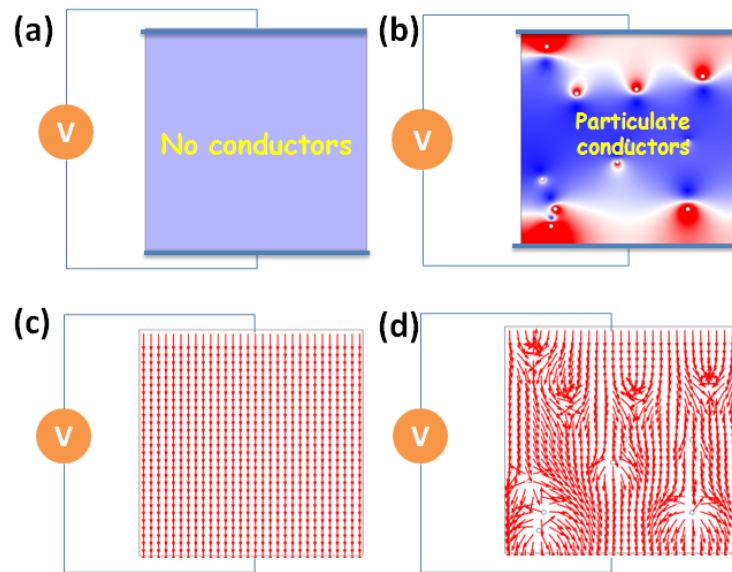


Fig. 5.2 Illustration of the inhomogeneous electric field. (a) Electric field intensity within composites with no conducting particles, (b) electric field intensity within composites with conducting particles, (c) electric field direction within composites with no conducting particles and (d) electric field direction within composites with conducting particles. The grey levels in figures (a) and (b) stand for the value of local field intensity. The arrows in figures (c) and (d) stand for the direction of local field.

The other group of magnetostrictive material listed, ferrites (represented by CFO), is widely used as the magnetic phase in 0 - 3 type ME ceramic composites. According to Ref. [181] and [182], it is a semiconducting material with its conductivity highly sensitive to composition, temperature and electric field (DC, AC, or frequency). For example, the recognized resistivity for pure CFO is about $10^8 \sim 10^{10}$ Ω -cm under a DC field, which decreases to about $10^4 \sim 10^6$ Ω -cm under a high frequency AC field (in order). Although the resistivity of CFO varies under different working environments, it can still be considered as a relatively conductive material



when compared to PZT. This difference in electrical resistivity between the components is the reason that accounts for the inhomogeneous internal electric field and piezoelectric performance within the composite.

Table 5-1 Resistivity of typical components in ME composites.

Components	Materials	Resistivity($\Omega \cdot \text{cm}$)
Piezoelectric	PZT	$10^{12} \sim 10^{13}$ [175 - 177]
	PVDF	10^{14} [178]
Magnetostrictive	Terfenol-D	$(57 \sim 64) \times 10^{-6}$ [179, 180]
	Cobalt Ferrite	$10^1 \sim 10^8$ [181, 182]

5.2.2 Materials and models to study the inhomogeneous electric field

To evaluate the influence of such inhomogeneity of local electric field, we consider a 0 - 3 type PZT - CFO composite with well-isolated magnetic particles. Then we pick a unit model from the composite (Fig. 5.3 (a)), in which both particles are simplified as cubic with their centers at the origin point (0, 0, 0). The size of the unit cube is set as $1 \times 1 \times 1 \text{ cm}^3$ ($L = 1 \text{ cm}$), and the side length (D) of the ferrite is tunable to realize different volume percentages of the ferrite (f_{CFO}). For example, when $D = 0.5$, $f_{\text{CFO}} = 12.5 \%$, and when $D = 0.6$, $f_{\text{CFO}} = 21.6 \%$. The poling direction of the unit model is along the z axis. Under a DC bias of 5 kV/cm in the z direction (realized by applying a voltage $V = 5 \text{ kV}$ on the plane $z = -0.5$ and grounding the plane $z = 0.5$),



the local electric field within the composite structure is obtained by employing finite element analysis based on the COMSOL multiphysics software and applying the conductive media DC static simulation of the electromagnetics application modes. The electrical resistivity of the components we use is $1 \times 10^6 \Omega \cdot \text{cm}$ for CFO, and $1 \times 10^{12} \Omega \cdot \text{cm}$ for PZT.

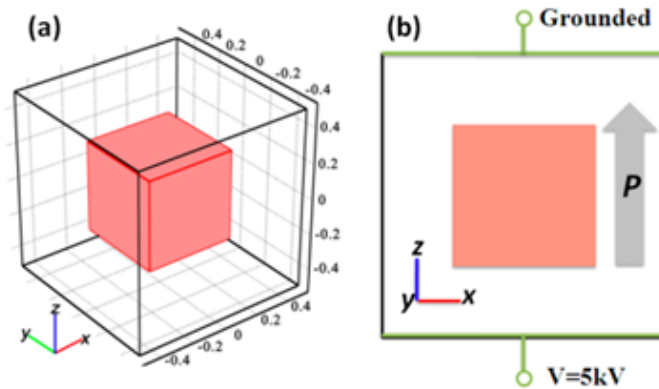


Fig. 5.3 Illustration for the unit model of 0 - 3 type composite.

5.2.3 Electric field distribution

Consider the composite containing 12.5 % CFO ($D = 0.5$). The electric field is found to have different variation trends in the slices with CFO ($x \leq 0.25$) and without CFO ($x > 0.25$). Two typical slices from these two groups with coordinates $x = 0.1$ and $x = 0.3$ (marked in Fig. 5.4 (b)) are selected, with their local electric field along the z direction presented in Figs. 5.4 (c) and 5.4 (d). One can find a large inhomogeneity in the electric field. In the slice planes containing CFO (i.e. $x = x_0, x_0 \leq 0.25$),



the upper limit of electric field is about two times larger than those in the planes without CFO ($x = x_0, x_0 \geq 0.3$). For example, although the applied field is fixed at 5 kV/cm, the local electric field within PZT varies from -0.111 to 18.906 kV/cm in the slice $x = 0.1$, and from 0.931 to 8.413 kV/cm in the slice $x = 0.3$. Such inhomogeneity is more obvious around the boundary areas between the two phases.

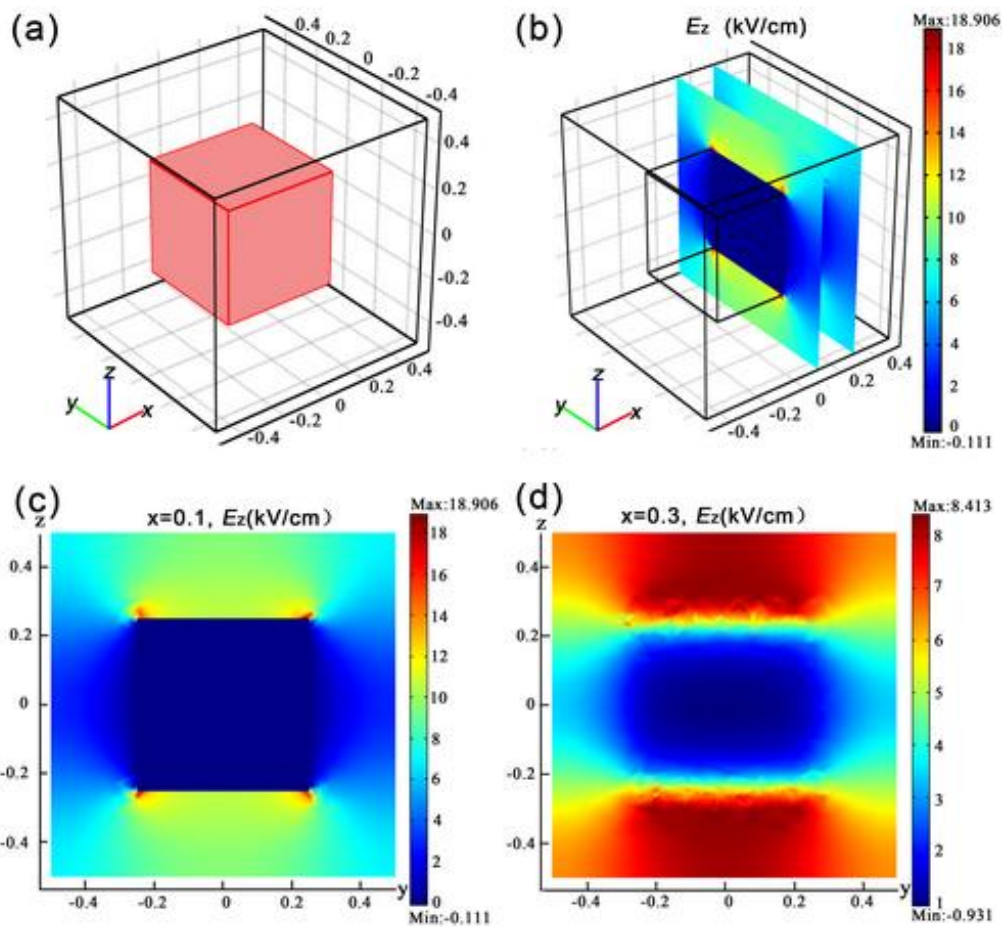


Fig. 5.4 Distribution of local electric field in the unit model. (a) Schematic diagram of the unit model, (b) two slices selected, (c) local electric field along z direction (E_z) in the slice $x = 0.1$ and (d) local electric field along z direction (E_z) in the slice $x = 0.3$.



5.3 The inhomogeneous electric field vs. piezoelectric poling

5.3.1 Introduction to piezoelectric poling

Potential piezoelectric materials can be forced to be piezoelectric by a process called poling. This process can only be carried out at temperatures below the Curie point (T_c). Piezo crystallites are centro-symmetric cubic (isotropic, see Fig. 5.5 (a)) above T_c and exhibit tetragonal symmetry (anisotropic structure, see Fig. 5.5 (b)) below T_c . In perovskite structures the dipole is created by movement of the central ion in the structure (usually a large metal ion). Above T_c , they lose the piezoelectric properties.

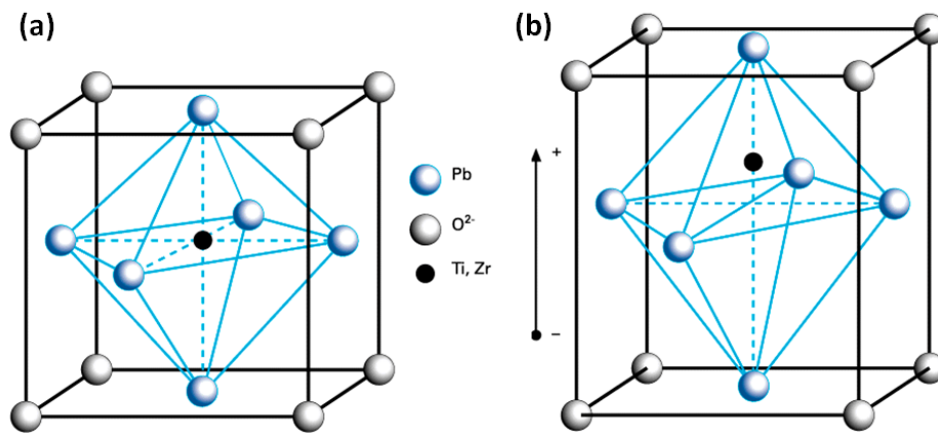


Fig. 5.5 Piezoelectric elementary cell (a) above and (b) below the Curie point (T_c).

The process of poling involves aligning all of these individual dipole moments, so that they all point in the same general direction. This is accomplished by putting the crystal in a constant electric field to force the dipoles to align. In the electric field



each dipole will feel a torque if it is not parallel to the field lines produced, and so is turned to that direction. When the electric field is removed, the dipoles remain fairly aligned, although there will still be some element of random direction.

When an electric voltage is applied to a poled piezoelectric material, the domains increase their alignment proportional to the voltage. The result is a change in dimensions (expansion or contraction) of the piezoelectric material.

5.3.2 Inhomogenous poling efficiency within 0 - 3 type composites

The performance of piezoelectric materials is closely related to their poling electric field (E_{poling}). Fig. 5.6 gives the d_{33} - E_{poling} relationship of $\text{Pb}_{0.99}[\text{Zr}_{0.45}\text{Ti}_{0.47}(\text{Ni}_{0.33}\text{Sb}_{0.67})_{0.08}]\text{O}_3$ in Ref. [170]. It can be found that, as the poling electric field increases, the piezoelectric coefficient increases linearly first, and then kept at a constant value when the poling field is large enough. One can get a conclusion that when the poling field is large enough exceeding a certain value, the composites will be fully poled. Otherwise, the poling will be insufficient with a lower piezoelectric coefficient.

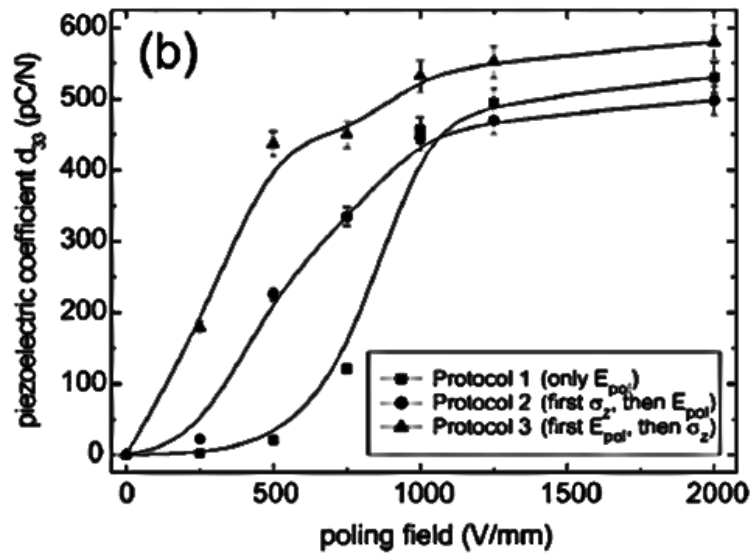


Fig. 5.6 The relationship between poling field and piezoelectric effect. [170]

However, full poling is very difficult for 0 - 3 type ME composite. This is due to two reasons:

- (1) The electric field cannot be large enough because of electric leakage.
- (2) Even if the electric field is large enough, its direction will be dramatically distorted in microstructure. This will cause the dipoles difficult to align in a consistent direction throughout the whole composite.

The effect of poling is hard to simulate as the field distribution is complex within the composites. But as the overall aligning is severely disturbed by the conducting CFO particles, it can be expected that the piezoelectric effect will be consequently weakened.



5.4 The inhomogeneous electric field vs. local d_{33} upon application

In converse magnetoelectric effect, the ME composites are supposed to work under electric field. As piezoelectricity is a field-dependent property. The non-uniform local field under application will cause inhomogeneity in the microstructural piezoelectric property. Such effect became more obvious when there is a large DC bias existing. In this Section, we will discuss this condition.

5.4.1 Introduction to the non-linear piezoelectric effect

Piezoelectricity is highly sensitive to the working electric field. According to the nonlinearity response theory, [182 - 184] the $d_{33} - E$ relationship for PZT ceramics is complex, depending on AC or DC field, amplitude and frequency of the electric field.

To describe the inhomogeneity in microstructural piezoelectric effect, we will discuss the condition that the working electric field contains a DC component of 5kV/cm (in consistent with Section 5.2). Our assumption of the $d_{33} - E$ relationship in PZT is based on ref [185], in which PZT was supposed to exhibit a d_{33} of 200 pC/N at very low ($E \sim 0$) DC field. When the electric field increases to 5, 10, and 20 kV/cm, the d_{33} decreases to 175, 150, 100 pC/N, respectively. Then based on the local electric field given in Fig. 5.3, the inhomogeneous piezoelectric property (described as d_{33}) can be derived as shown in Fig. 5.7. One can see that the piezoelectric effect varies in microstructure. It should be noted that this is a rough assumption describing the variation trends in the relationship between d_{33} and E . In real piezoelec-



tric material, the electric field dependence of d_{33} is more complex.

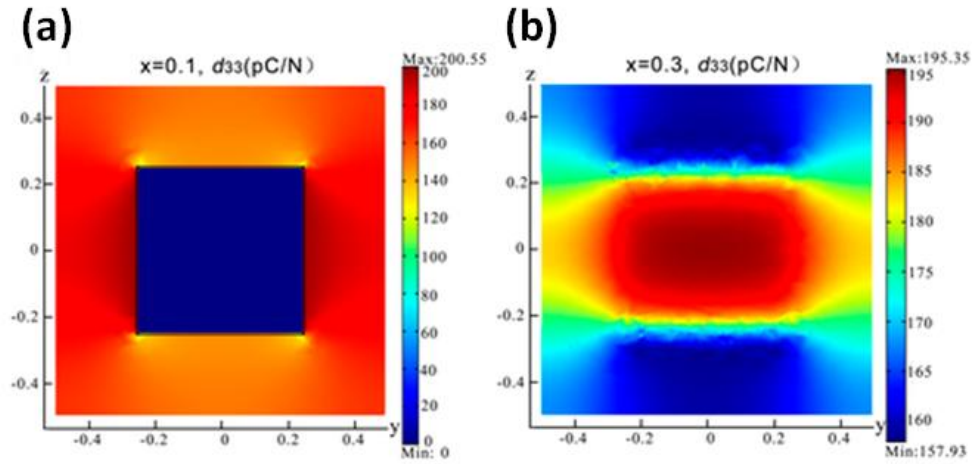


Fig. 5.7 Distribution of local piezoelectric property (d_{33}) in (a) the slice $x = 0.1$ and (b) the slice $x = 0.3$.

5.4.2 Averaged d_{33}

To evaluate the effect of inhomogeneous local piezoelectric property on PZT's macroscopic performance, we divide the unit model into a number of thin cylinders with their axis along the line $x = x_0, y = y_0$ ($x_0, y_0 \in [-0.5, 0.5]$). If the cylinders are thin enough and the deformation along the z axis is continuous within the unit model, we can neglect mechanical interaction along the z axis between neighboring cylinders. Then the average d_{33} (marked as $d_{33, \text{average}}$) within each cylinder can be estimated via the inner electrode method. For each cylinder, suppose an electric voltage V_3 is applied to it. Consequently a macroscopic piezoelectric-induced strain, S_3 , is excited along the same direction. Then we put $(N - 1)$ equidistant parallel inner electrodes



within it imaginarily, with each of them perpendicular to the applied field. These imaginary electrodes divide the cylinder into N isometric segments, each with a side length, $1/N$, along the z direction. Suppose N_{PZT} of the segments are made of PZT phase, and the other $(N - N_{PZT})$ segments are made of CFO phase. Then, for the i th PZT segment ($i \in [1, N_{PZT}]$), its displacement, ΔL_i , can be calculated as:

$$\Delta L_i = S_{3,i} \frac{1}{N} = (d_{31,i} E_{1,i} + d_{32,i} E_{2,i} + d_{33,i} E_{3,i}) \frac{1}{N} \quad (5-1)$$

where $S_{3,i}$ is its strain along the z direction, $d_{33,i}$, $d_{31,i}$, and $d_{32,i}$ are components of its local piezoelectric coefficient and $E_{1,i}$, $E_{2,i}$, $E_{3,i}$ are the projections of local electric field along the x , y and z directions within the segment, respectively. As $E_{1,i}$ and $E_{2,i}$ can be neglected when compared to $E_{3,i}$, this equation can be simplified as:

$$\Delta L_i = S_{3,i} \frac{1}{N} = (d_{33,i} E_{3,i}) \frac{1}{N} \quad (5-2)$$

Accordingly, the averaged d_{33} along this line can be calculated as:

$$d_{33,average} = \frac{S_3}{E_3} = \frac{1}{N} \sum_{i=1}^{N_{PZT}} (d_{33,i} E_{3,i}) \quad (5-3)$$



In Eq. (5-4), V_3 is the applied electric voltage. $E_{3,i}$ and $d_{33,i}$ are the local electric field and local piezoelectric coefficient, respectively. When $N \rightarrow \infty$, Eq. (5-3) can be modified to integration along the z axis:

$$d_{33, \text{average}}(x_0, y_0) = \frac{\int_0^L d_{33}(z) E_3(z) dz}{LV_3} \quad (5-4)$$

Based on Eq. (5-4), the relationship between $d_{33, \text{average}}$ and the position of the cylinder can be obtained. We normalized the obtained piezoelectric coefficient by dividing the calculated $d_{33, \text{average}}$ by $d_{33, 0}$ (the piezoelectric coefficient under zero fields). And the relationship between the $d_{33, \text{average}}/d_{33, 0}$ value and the position (x, y) for the PZT - CFO unit model ($f_{\text{CFO}} = 12.5\%$) is plotted in Fig. 5.8 (a). The height (z -coordinate) of each black spot (x_0, y_0) stands for the value of $d_{33, \text{average}}$ within the cylinder specified by the axis $x = x_0, y = y_0$. The $d_{33, \text{average}}/d_{33, 0}$ value in the whole composite is found to vary greatly ranging from 0.82 to 0.99, indicating that the efficient piezoelectric coefficient is smaller than its supposed value corresponding to the externally applied field (i.e., $E_{\text{apply}} = 5$ kV/cm). Fig. 5.8 (b) shows the relationship between $d_{33, \text{average}}/d_{33, 0}$ value and y in the slices $x = 0.1, 0.2, 0.3, 0.4$ and 0.5 cm. It can be found that the cylinders containing the CFO phase ($x \leq 0.25, y \leq 0.25$) exhibit a relatively smaller $d_{33, \text{average}}/d_{33, 0}$ value (0.8 - 0.91) than those without CFO (0.94 - 0.99). And the averaged d_{33} was weakened to a great extent in the boundary region (around the CFO particle) between the component phases.

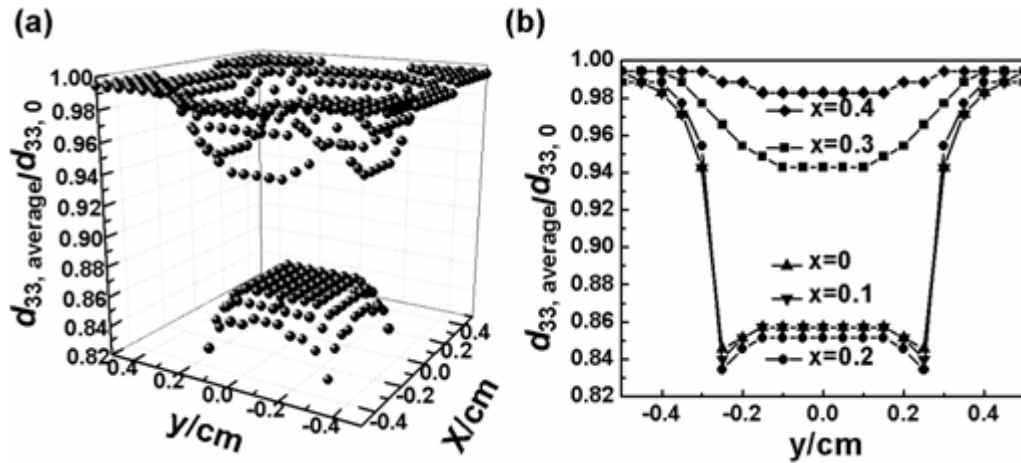


Fig. 5.8 The $d_{33, \text{average}}/d_{33, 0}$ value in the unit-cell model.

5.4.3 Relationship between CFO's volume fraction and the averaged d_{33}

Composites with different volume percentages of CFO (f_{CFO}) are also analyzed with the same method by changing the dimensions of the CFO cube. Fig. 5.9 gives the relationship between the $d_{33, \text{average}}/d_{33, 0}$ value and the position of the cylinder for the composites with $f_{\text{CFO}} = 12.5\%$, $f_{\text{CFO}} = 21.6\%$ and $f_{\text{CFO}} = 34.3\%$. The horizontal ordinate, $(x^2 + y^2)^{1/2}$, refers to the distance between the specified cylinder and the center of CFO phase (i.e., the origin of the coordinate in our model). In all the three composites, the cylinders marked with their axis coordinates are categorized into two groups depending on whether there is CFO containing in them (solid spot) or not (hollow spot). Similar variation trends are found in these two groups for composites with different volume percentages of CFO. For the cylinders containing CFO, as the distance from the center increases, the $d_{33, \text{average}}/d_{33, 0}$ value keeps constant first, and then decreases gradually to its minima around the corner of the CFO grain. For the cylinders without CFO, as the distance from the center increases, the $d_{33, \text{average}}/d_{33, 0}$



value increases gradually to its maximum first, and then kept constant when it is far from the CFO phase. The $d_{33, \text{average}}/d_{33, 0}$ value is also highly dependent on CFO's volume percentages. A rapid decrease is observed in it with the increase of CFO's content. Such a decrease is especially negligible in the cylinders containing CFO. For example, when f_{CFO} increases from 12.5 % to 34.3 %, the $d_{33, \text{average}}/d_{33, 0}$ value decreases from 0.82 - 0.86 to 0.63 - 0.67 for the cylinders containing CFO. Also, all of its values are below 1, indicating an overall decrease in the piezoelectric property of the composites.

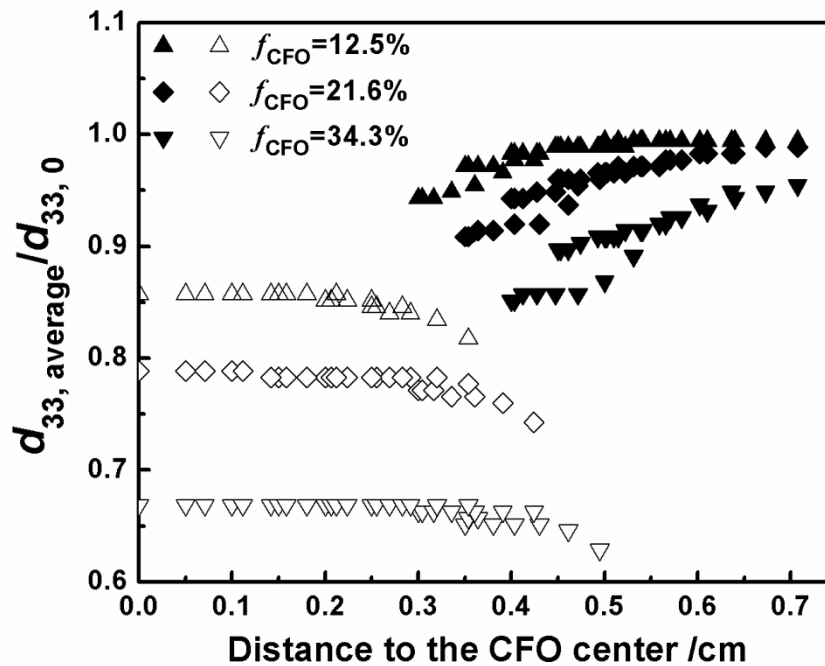


Fig. 5.9 The $d_{33, \text{average}}/d_{33, 0}$ value as a function of position (described with distance to the CFO center) in composites with different volume percentages of CFO.



5.4.4 Overall d_{33}

The averaged d_{33} within the overall unit model can also be estimated. Based on the local d_{33} obtained before, we define an effective d_{33} at one local point (x, y, z) according to the applied electric field, i.e.,

$$S = d_{33}(x, y, z)E_3(x, y, z) = d_{33,\text{effective}}(x, y, z)\frac{V}{L} \quad (5-5)$$

Then we have:

$$d_{33,\text{effective}}(x, y, z) = d_{33}(x, y, z)E_3(x, y, z) / E_{\text{applied}} \quad (5-6)$$

For the whole unit model, we have the overall d_{33} ($d_{33,\text{overall}}$) as:

$$d_{33,\text{overall}} = \frac{\int dV d_{33,\text{effective}}(x, y, z)}{V} = \frac{\int dV d_{33}(E_3)E_3(x, y, z)}{E_{\text{applied}}V} \quad (5-7)$$

The $d_{33}(E_3)$ in Eq. (5-7) is treated as zero when the coordinate (x, y, z) is in the region of CFO. This integration can be calculated with COMSOL 3.5a. The result shows that the $d_{33,\text{overall}}/d_{33,0}$ is 0.94 when the volume percentage of CFO is 12.5 %, 0.88 for 21.6 %, and 0.77 for 34.3 %, indicating a decrease of 5.7 %, 12 %, and 22.8 %



in the overall piezoelectric property caused by the inhomogeneous piezoelectric property in the microstructure.

5.4.5 Overall magnetoelectric coefficient, $\alpha_{E, 33}$

The influence of inhomogeneous microstructure on converse magnetoelectric coefficient is more complex. In 0 - 3 PZT - CFO composites, the coupling is strongest around the CFO particles. However, according to our simulations, it is just in these boundary regions where the electric field concentrates greatly to cause a large weakening in local piezoelectric property. So it is reasonable to conclude that the influence of the inhomogeneous piezoelectric property in microstructure will cause an even larger weakening to the overall magnetoelectric effect when compared to that of the overall piezoelectric property.

Figure 5.10 gives the magnetoelectric coefficient simulated based on the approach introduced in Chapter 4. It can be found that when considering the non-linear piezoelectricity (curve with broken line), the theoretical predicted value of the coupling coefficient is largely decreased. This may also be one of the reasons why the experimental results on ME effect is below the theoretically predicted value.

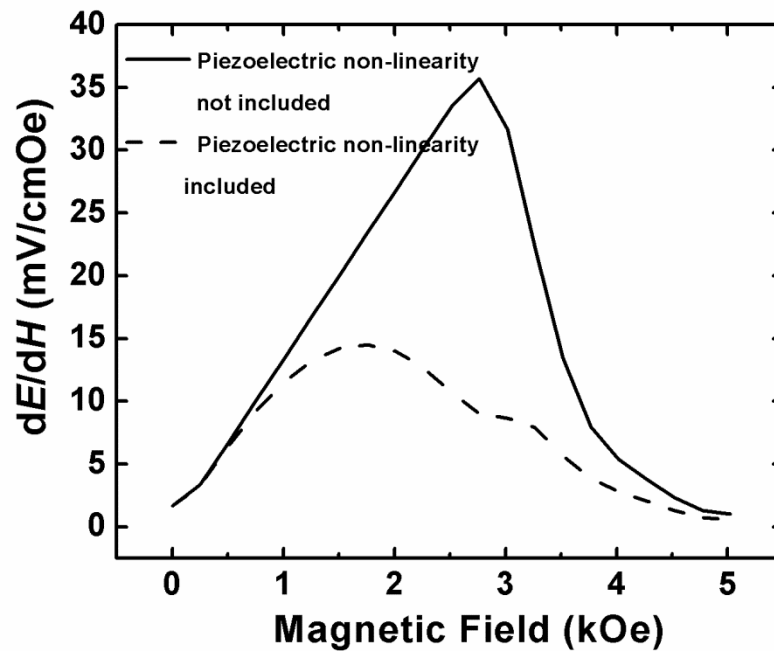


Fig. 5.10 The calculated magnetolectric effect. The straight curve stands for the condition in which non-linear piezoelectricity is not included. The dash curve stands for the condition in which non-linear piezoelectricity is included.

5.5 Summary

In this Chapter, the inhomogeneous internal electric field of 0 - 3 type PZT - CFO composites was simulated via the finite element analysis method. Based on the inhomogeneity of internal electric field, two field-related processes (poling and CME effect) are studied. The results are:

- (1) Piezoelectric poling. We pointed out that small poling voltage and distorted poling direction are the two reasons accounting for insufficient poling in 0 - 3 type ME composites.
- (2) Based on the field-dependent piezoelectricity, the inhomogeneous pie-



zoelectric property and its influence on the overall piezoelectric and magnetoelectric properties were calculated. It has been proposed that the conducting magnetic particles causes large inhomogeneity in microstructural piezoelectric phase and hence a weakening of the overall piezoelectric and magnetoelectric coefficient. This weakening becomes more obvious when increasing CFO's content in the composite.



CHAPTER 6

0 - 3 type CFO - PZT composite with enhanced piezoelectric and magnetoelectric properties

6.1 Introduction

Magnetoelectric composite is a multi-phase system consisted of conducting particles and non-conducting particles. According to the percolation theory, for such system with random arrangement of the particles, electrical percolation will happen inevitably when the volume fraction of the conducting components exceeds a critical value (corresponding to the percolation threshold, p_c). Such effect remains as one of the hindrances in increasing the magnetic phase's volume fraction and adversely affects the improvement of the ME coupling coefficient for 0 - 3 type ME composites. According to those reported in literature, particulate composites exhibit much smaller ME coefficient (0.06 - 0.13 V/Oe·cm) than laminated ones (2 - 20 V/Oe·cm) mainly due to inter diffusion at the grain boundaries and low resistivity of the magnetic ferrites.

To improve the percolation threshold in ME composite, we introduced a method of fabricating co-fired lead zirconate titanate (PZT) /cobalt ferrite (CFO) 0 - 3 composite ceramics in this Chapter. A ZrO_2 layer is introduced into the PZT - CFO composite as highly resistive barrier and lubricant. The ZrO_2 shell plays its roles in three ways: (1) prevent Fe^{3+} and Co^{2+} ion diffusion from the CFO phase to the PZT matrix, (2) improve the mechanical interaction between CFO and PZT due to its complex lattice structure, and (3) enhance electrical resistivity of the composite. As



to be demonstrated later in this Chapter, the composites prepared under optimal conditions exhibit excellent piezoelectric properties which, to the best of our knowledge, have not been reported in the literature.

Based on its good piezoelectric feature, a step-down transformer structure is designed, with its response to both an input AC electric field (with/without DC bias) and an AC magnetic field to be presented in this Chapter. The device shows good sensitivities to both DC and AC magnetic field and therefore has potential as detector of magnetic field, especially for weak AC signal. A further coupled effect between the magnetoelectric effect and the electromechanical effect is observed in the transformer structure, which allows the output signal to be tunable via varying the input magnetic/electric signal.

This Chapter is organized into 3 Sections apart from the introduction and the summary. Section 6.2 gives the experimental approach to synthesize highly resistive CFO - PZT composite. Section 6.3 gives the electric, dielectric, ferroelectric, and magnetoelectric property of the composite, indicating an improved piezoelectric and ME coupling property. In Section 6.4, the design of the transformer is stated in detail.

6.2 Highly resistive CFO - PZT composites

To avoid the electric percolation in 0 - 3 PZT - CFO composite, we aim to form a structure in which the conductive magnetic component (CFO) is wrapped with a shell of highly resistive zirconia, as shown in Fig. 6.1. Such microstructure is supposed to work like Fig. 6.2 when exposed to an external electric field. The dash



curve in Fig. 6.2 stands for the electron path. When the CFO particles (inner sphere) are connected in the composite, an electron path will form in the microstructure as shown in Fig. 6.2 (a). If one (Fig. 6.2 (b)) or more (Fig. 6.2 (c)) of the conductive CFO particles are wrapped with a highly resistive shell, the electron path will be blocked half way. Under an ideal condition in Fig. 6.2 (d), all of the particles have wrappings and no leakage happens.

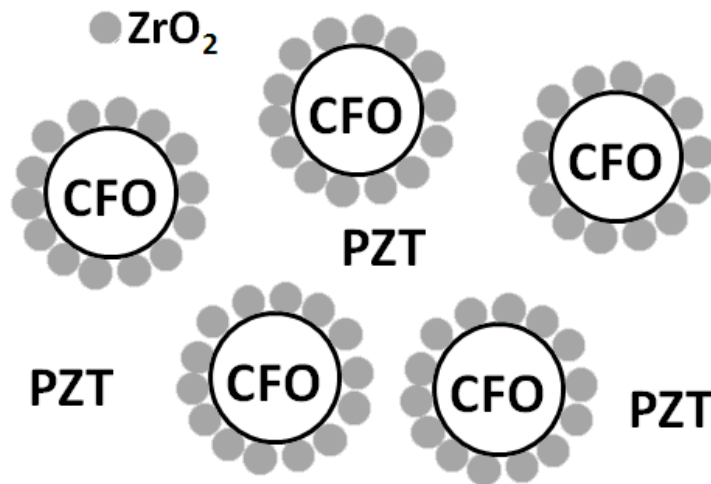


Fig. 6.1 Illustration for the highly resistive PZT - CFO composite.

To synthesize composites with such a microstructure, a wet chemical method is used to fabricate the CFO - ZrO₂ core-shell particles first, and then traditional co-fired process is employed to synthesize the composite ceramics. Different from the conventional preparation of particulate ME composites, some experimental conditions are modified to benefit the formation of core-shell structure.

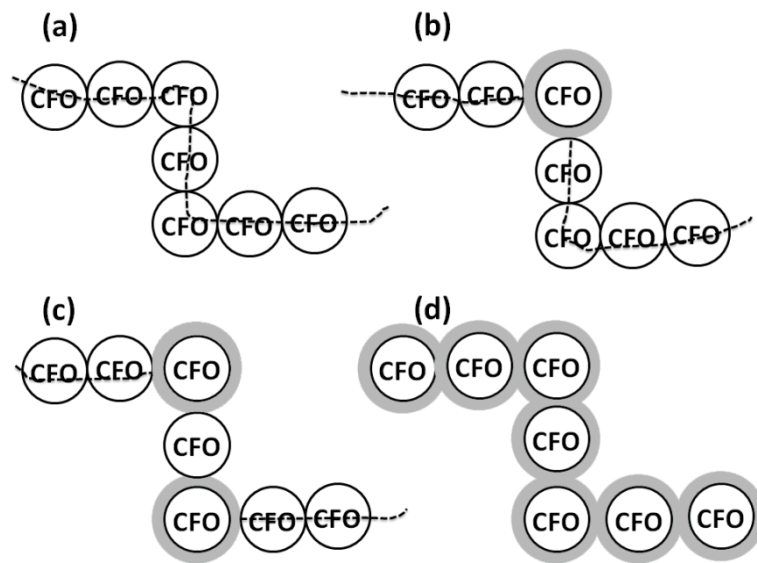


Fig. 6.2 The working principle of the highly resistive composite. (a) No CFO particle is modified with a highly resistive shell; (b) and (c) stand for the condition that one or more of the particles are modified with highly resistive shells; (d) All the CFO particles are modified with highly resistive shells.

6.2.1 Synthesis of the CFO - PZT composites with high resistivity

The experimental procedure to synthesize a highly resistive CFO - PZT composite is divided into three steps as shown below:

1) Preparation of CFO and PZT particles

The magnetostrictive phase, cobalt ferrite (CoFe_2O_4 , CFO) were prepared using reagent-grade Co_2O_3 (purity > 99 %) and Fe_2O_3 (purity > 99 %) as starting materials. After ball-milling and calcining the raw materials at 900 °C for 2 h, CFO powders were obtained. These as-prepared powders were then sintered at a higher temperature of 1270 °C to allow the grains to grow larger, which is preferred to serve as a core in



the core-shell structure. A further ball milling and drying process was used to refine the CFO powders.

The piezoelectric phase, lead zirconate titanate (PZT), was prepared from PZT502 ($\text{PbZr}_{0.52}\text{Ti}_{0.48}\text{O}_3$, from PKI, USA), with an addition of ($0.5\text{Li}_2\text{CO}_3 + \text{Bi}(\text{NO}_3)_3$) by weight percentage as sintering additives. The starting materials were mixed, ball-milled and calcined at 600°C for two hours to form PZT powder.

2) Microstructural modification of the conductive CFO particles

Zirconium n-butoxide was dissolved in toluene (100 ml) to form a clear solution, the concentration of zirconium n-butoxide solution varied from 0.1 to 0.3 mol/L. CFO powders (20 g) were then dispersed in the freshly prepared solution with the aid of ultrasonication for 20 min. A mixture of water/ethanol (1 : 5 in weight) was added at the $\text{Zr}/\text{H}_2\text{O}$ molar ratio of 1 : 2, followed by mixing to benefit the hydrolysis reaction at 80°C for 1 h under stirring before separation. Then, the powder was filtered, dried and calcined at 800°C for 1 h to form a ZrO_2 coated CFO powder.

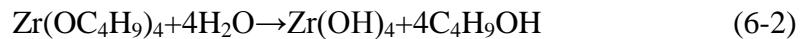
3) Preparation of $x\text{CFO} - (1 - x)\text{PZT502}$ 0 - 3 composite ceramics

The 0 - 3 composites of PZT/CFO were made by conventional ceramic sintering process. The ZrO_2 -coated CFO powders were mixed with the as-prepared PZT at various weight ratios of 9 : 1, 8 : 2 and 7 : 3. The powder samples with three different compositions were then pressed into disks of 1 mm thick and 15 mm in diameter and then sintered at 1050°C for 2 h to form the composite ceramics. In order to perform the electrical measurements, silver electrodes were fired on both sides of the ceramic disks at 550°C for 30 minutes.



6.2.2 Optimization of the experimental conditions

The ZrO_2 used to wrap the CFO particles were synthesized by the hydrolysis of $\text{Zr}(\text{OC}_4\text{H}_9)_4$, with the chemical equations given below:



The deposition of these newly generated ZrO_2 onto CFO particles (dispersed in solution) formed a core-shell-like structure. The morphology of such a structure is affected by both the generation rate and the deposition rate of ZrO_2 particles.[186] When the deposition rate exceeded the generation rate, all generated ZrO_2 particles fell on CFO particles as a shell. Conversely, if the deposition rate cannot keep pace with the generation rate, the ZrO_2 particles tended to self-aggregate, which may lead to an irregular distribution of CFO and ZrO_2 . To control the generation rate of ZrO_2 particles, different concentrations of $\text{Zr}(\text{OC}_4\text{H}_9)_4$ solution is used in our experiment. Fig. 6.3 gives the TEM image of CFO - ZrO_2 structures prepared from different concentrations of $\text{Zr}(\text{OC}_4\text{H}_9)_4$ solution. The results show that when $\text{Zr}(\text{OC}_4\text{H}_9)_4$ solution has the concentration of 0.1 mol/L (Fig. 6.3 (a)), no zirconia coatings can be formed around the CFO particles. When the concentration is increased to 0.19 mol/L, uniform core-shell particles are obtained (Fig. 6.3 (b)). However, when increasing the $\text{Zr}(\text{OC}_4\text{H}_9)_4$ concentration to 0.27 mol/L, self-aggregation of the ZrO_2 particles occurred (Fig. 6.3 (c)). [187] Based on this, the CFO - ZrO_2 core-shell particles we



mentioned later are all prepared from the $\text{Zr}(\text{OC}_4\text{H}_9)_4$ solution with the concentration of 0.19 mol/L.

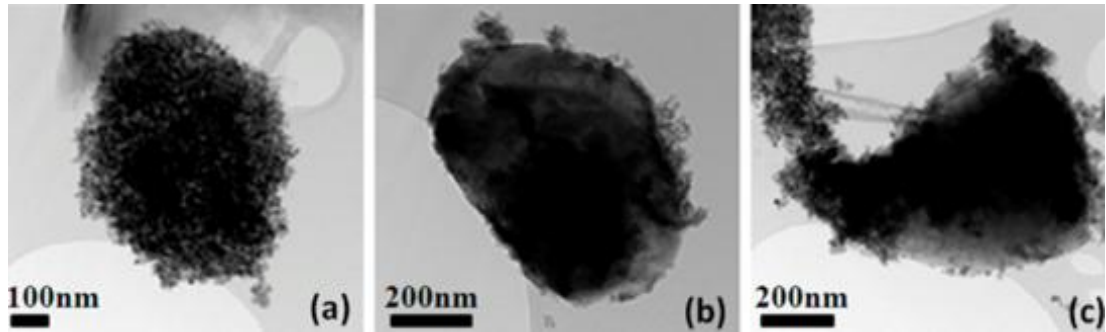


Fig. 6.3 TEM images of ZrO_2 coated CFO particles prepared with solution with different concentrations of zirconium n-butoxide. (a) 0.1 mol/L, (b) 0.19 mol/L and (c) 0.27 mol/L.

6.2.3 Microstructural characterization of the ZrO_2 - CFO particles

The crystalline phases of the prepared ZrO_2 - CFO core shell particles were studied by X-ray diffraction using a Philips X-ray diffractometer (Model PW1710) with $\text{Cu K}\alpha$ (radiation ($\lambda = 1.5418 \text{ \AA}$)), as shown in Fig. 6.4. XRD patterns of the 800 °C-annealed CFO - ZrO_2 particles confirm the coexistence of both phases in the particles. The zirconia precursor is found to crystallize into monoclinic-phase ZrO_2 , with its typical peaks marked in Fig. 6.4.

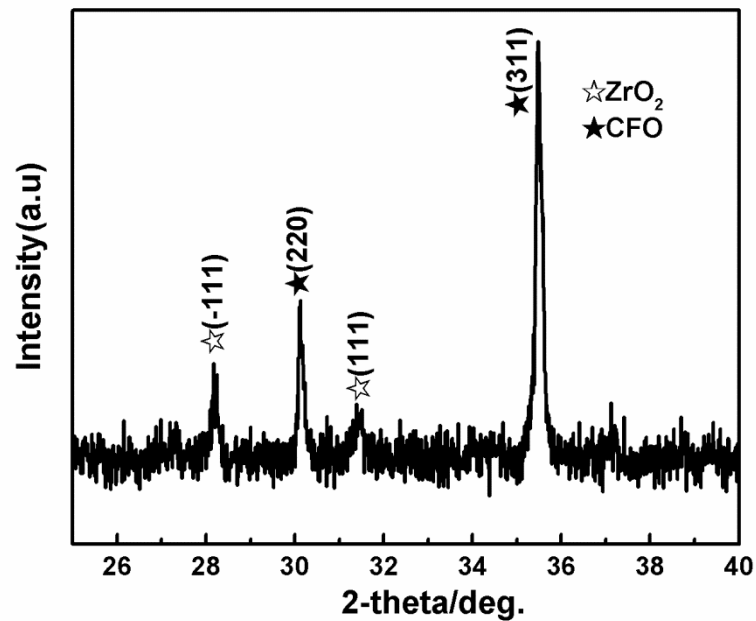


Fig. 6.4 XRD pattern of the ZrO_2 -coated CFO particles.

HRTEM was used to confirm the detailed structure of these particles, as shown in Fig. 6.5. Fig. 6.5 (a) gives the morphology of one typical ZrO_2 -CFO particle. It can be found that the shell particles, ZrO_2 , have a grain size of ~ 10 nm, and the core particle, CFO, has a grain size of 500nm. Figs. 6.5 (b) and 6.5 (c) show the HRTEM image of two edges of the particles. The interplanar spacing of the core phase is found to be 4.89 \AA in accordance with that of the (111) planes of cubic-structured CFO. And the lattice spacing of the shell particles is 2.84 \AA in accordance with that of planes (111) for monoclinic-structured ZrO_2 . This is also in good agreement with the elemental atomic composition of the core and edge regions obtained from the energy dispersive X-ray spectroscopy (EDX). According to the EDX analysis, elements Zr, Co, Fe, and O are present in both the core regions and the edge regions, but the core region shows a larger concentration of Co and Fe and a lower content of



Zr. Fig. 6.5 (d) gives the HRTEM image of the dispersed ZrO_2 particles with a monoclinic structure.

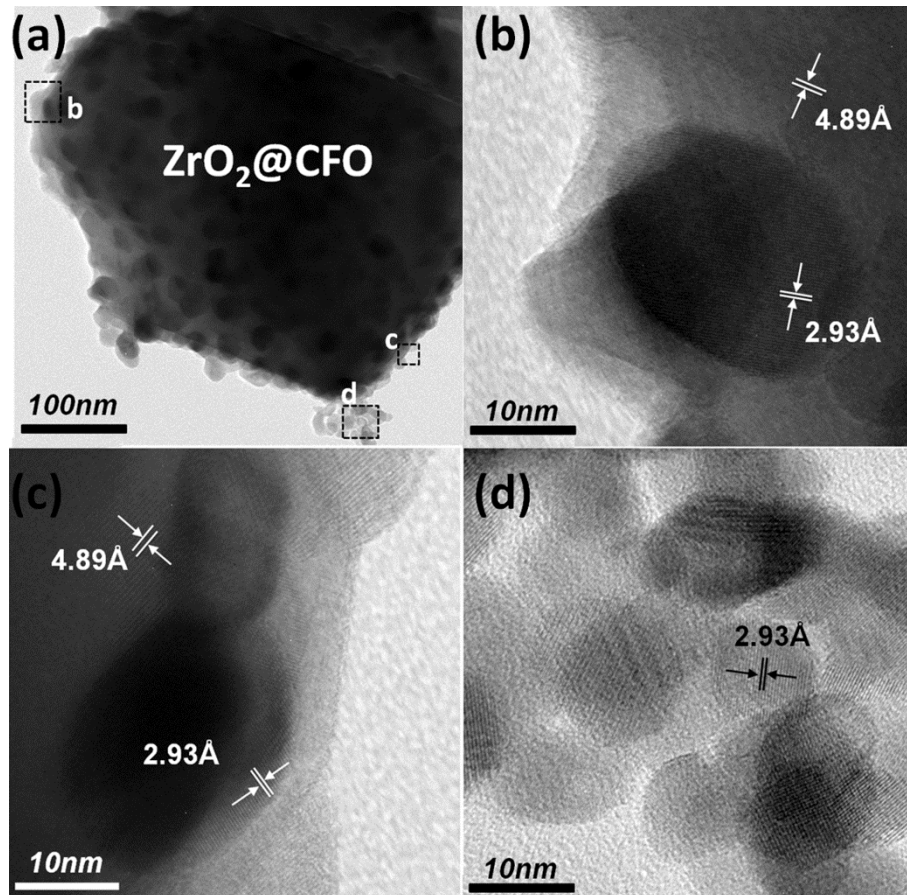


Fig. 6.5 (a) TEM image of CFO particle coated with ZrO_2 particles. (b) and (c) gives the HRTEM image of two edges of the ZrO_2 coated CFO particle. (d) The dispersed ZrO_2 particles.

6.2.4 Microstructural characterization of the PZT - CFO composite

XRD patterns of $x\text{CFO} - (1 - x)\text{PZT502}$ ($x = 0.15, 0.3$ and 0.45) particulate ceramic composites are shown in Fig. 6.6. Both CFO and PZT phases are present in the



composites, with their identified peaks marked in the pattern. ZrO_2 is identified by its highest peak at 28.2° , caused by the planes $(\bar{1}11)$.

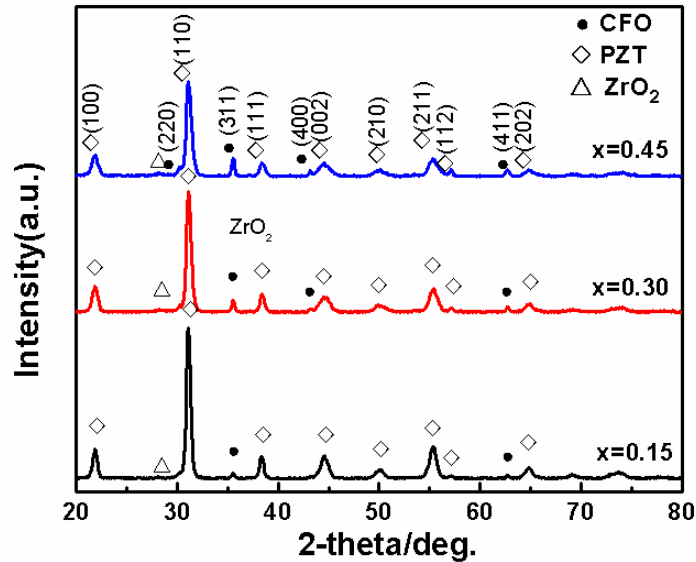


Fig. 6.6 XRD patterns of $x\text{CFO} - (1-x)\text{PZT}502$ ($x = 0.15, 0.3$ and 0.45) particulate ceramic composites prepared with ZrO_2/CFO particles.

Fig. 6.7 gives the STEM-BSE (backscattered electron) image for a typical $0.15\text{CFO} - 0.85\text{PZT}$ ceramic sample. The samples with other volume fractions of CFO show similar microstructural morphologies but with a higher concentration of CFO in the view, which is not presented here. In Fig. 6.7, three kinds of grains with different brightness are found in this image, each with a respective grain chosen from them, marked as a, b, and c respectively.

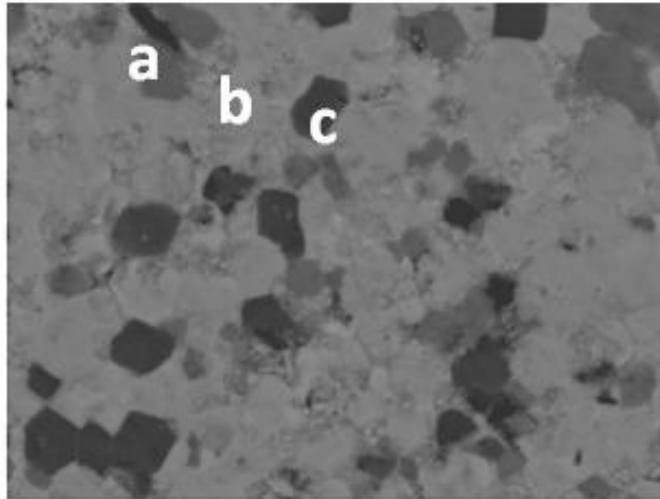


Fig. 6.7 STEM-BSE image of the 0.15CFO - 0.85PZT ceramic composites prepared with ZrO_2/CFO particles.

High spatial resolution energy-dispersive X-ray (EDX) analysis was used to confirm the identities of these grains (Fig. 6.8). For the regions with the same lightness as grain (b), element Pb, Zr, and O exist, and this confirmed its composition as PZT. A well-grown PZT grain in this picture has a grain size of $\sim 2.5 \mu\text{m}$. Grain (a) and grain (c) are both CFO grains, with a grain size of $\sim 2.5 \mu\text{m}$. Within the region of grain (a), only element Zr and O is detected, which confirmed its composition as a ZrO_2 -coated CFO grain (The CFO core is confirmed by its grain size). This content of Zr element is larger than that in grain (b) because of a higher mass fraction of element Zr in ZrO_2 than that in PZT. Within the region of grain (c), elements Co, Fe, and O are found within its region, confirming its composition as CFO, whose ZrO_2 coating may be smoothed away when polishing the sample.

To confirm the above conclusion, a linear scan of EDX analysis was also performed. The elemental compositions of the grains with the marks (a), (b), and (c) are



given in Fig. 6.9. Along the line picked, three typical grains appeared. The elemental distribution recognized their composition as ZrO_2 -coated CFO, PZT, and CFO respectively.

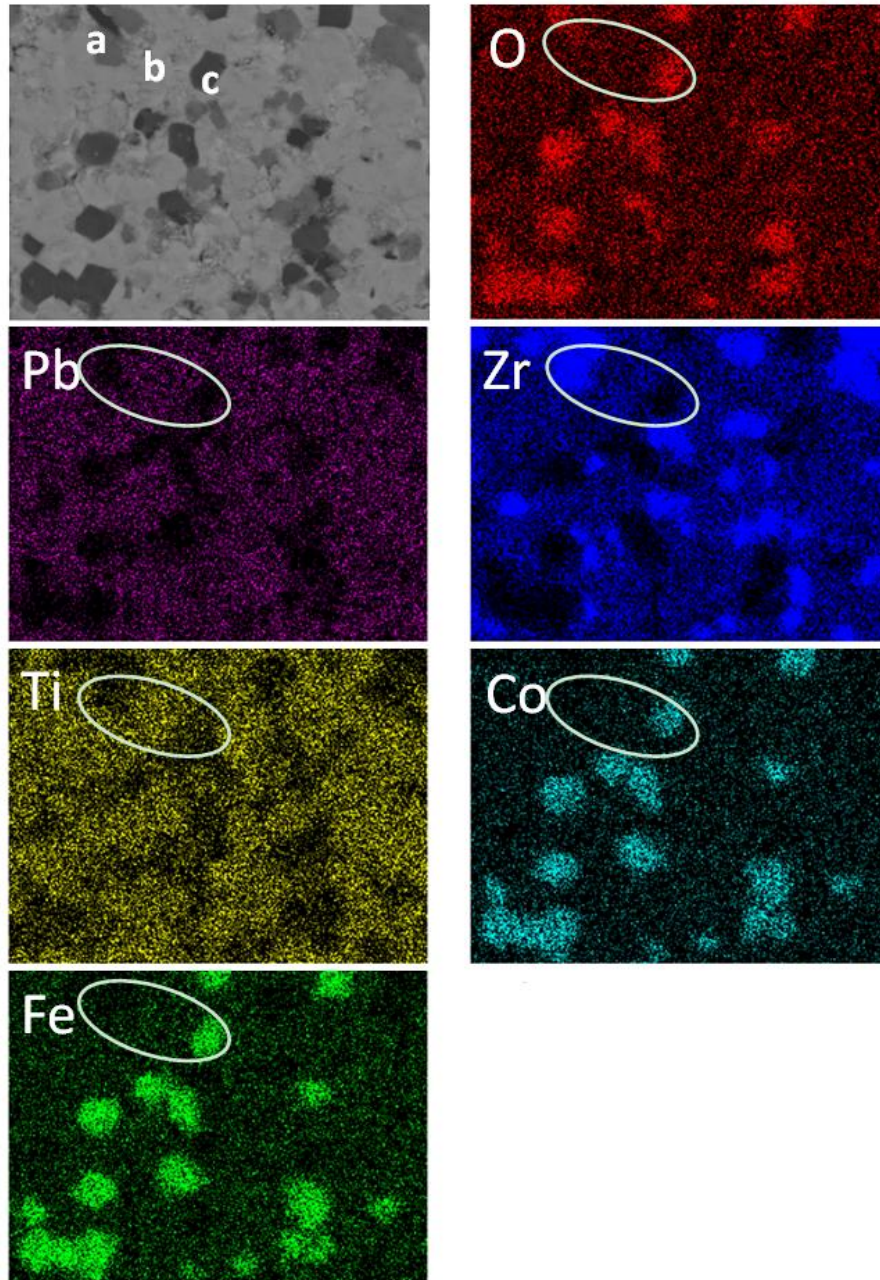


Fig. 6.8 SEM-EDX element maps of the 0.15CFO - 0.85PZT ceramic composites.

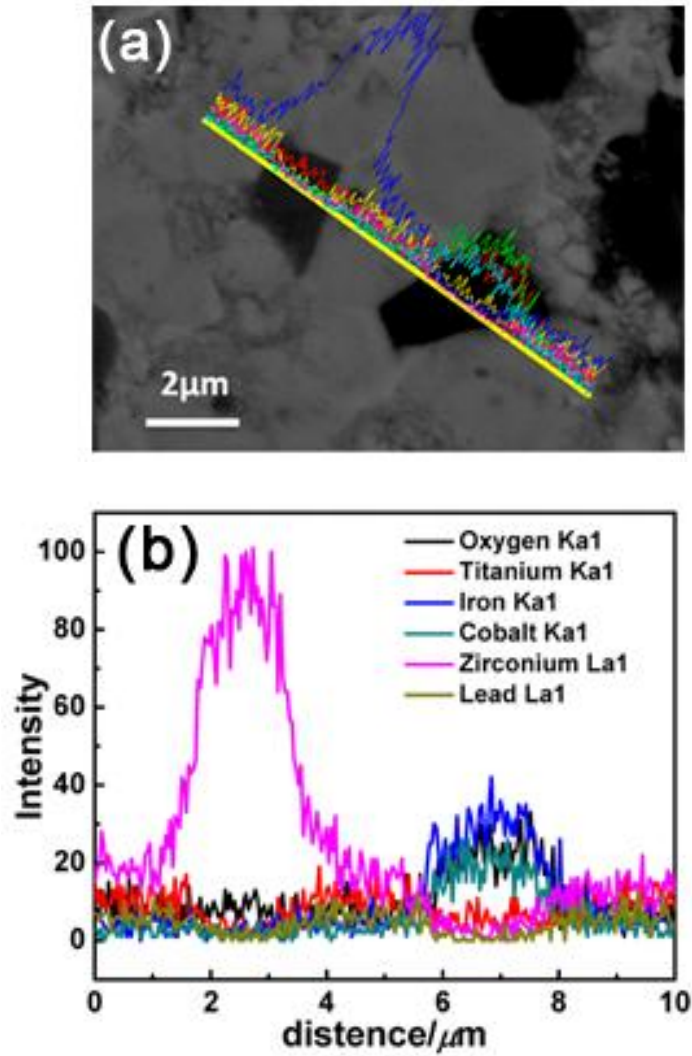


Fig. 6.9 SEM-EDX analysis of the 0.15CFO - 0.85PZT ceramic composites (linear scan). (a) SEM image and (b) elemental analysis.

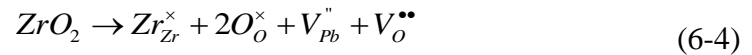
6.2.5 Mechanism of the microstructural modification

ZrO₂ is chosen as an electric barrier between CFO particles mainly due to its high resistivity (in the order of $\sim 10^{10} \Omega\cdot\text{m}$), large breakdown electric field (4 - 5 MV/cm), chemical durability in the sintering process, and complex lattice structure

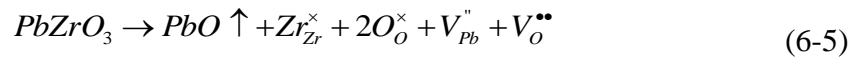


to optimize the lattice coupling between PZT and CFO.

When mixed with PZT, the coated ZrO_2 shell isolates the conducting CFO particles from each other. During the sintering process, the wrapped ZrO_2 nanoparticles tend to disperse into the PZT lattice as the reaction equation below:



At the same time, due to the volatility of PbO, the lead-based ceramics releases PbO when sintering at high temperature, with following reaction:



The vacancies generated in Eq. (6-5) suppress the incorporation of zirconia into the PZT lattice, and thus the ZrO_2 nanoparticles could remain in the matrix after sintering. Also, a relatively low-temperature sintering process with short soaking time for the composite ceramics would benefit in preventing ZrO_2 nanoparticles from dispersing into the PZT lattice.

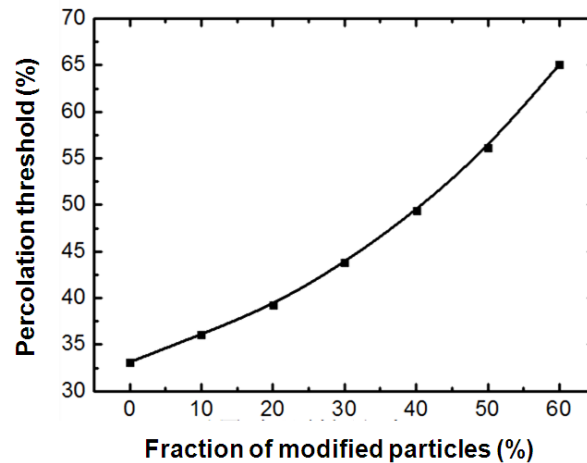


Fig. 6.10 The percolation threshold as a function of the fraction of ZrO_2 modified CFO particles in the PZT - CFO particulate composites.

The effects of ZrO_2 in the ME complex material can be understood from two perspectives: one is to increase the percolation threshold in the PZT - CFO particulate composites, and the other is to enhance the coupling of magnetic phase and piezoelectric phase. Fig. 6.10 illustrates the increase of percolation threshold (volume percentage) due to the ZrO_2 coating of conductive CFO particles calculated according to the percolation theory. The x -axis stands for the percentage of ZrO_2 -coated CFO particles in all the CFO particles. It can be found that as the modified particles increases, the percolation threshold increases too. When 60 % of the CFO particles are coated, the percolation threshold can be enhanced twice. Besides, the ZrO_2 also exerts its function in enhancing the lattice coupling between the magnetic and piezoelectric phases. It is known that CFO and PZT have different crystal structures and lattice parameters. Few common values can be found in their inter-planar distances. When the two phases are dispersed in the ceramic composite with random orientations, the lattice matching of the two materials can be expected to be weak. On the



contrary, ZrO_2 has a monoclinic crystal structure with varied inter-planar distances. So it is reasonable to consider that ZrO_2 can work as a matchmaker between CFO and PZT to enhance the lattice coupling at the interface.

6.3 Magnetoelectric property of the CFO - PZT composite with modified microstructure

In order to perform the electrical measurements, silver electrodes were fired on both sides of the ceramic disks at $550\text{ }^\circ\text{C}$ for 30 minutes. And then the samples were electrically polarized in silicone oil under a poling field of about 4.5 kV/mm at room temperature. For the sample with different volume percentages of CFO, the poling voltage is set at the same value, while the leaking current during the poling process is larger for the sample with higher volume percentage. The piezoelectric constant d_{33} was measured using a standard piezo d_{33} meter (model ZJ-3A). An impedance analyzer (Agilent 4294A) was used to measure the electrical resistivity and the dielectric constant of the specimens.

The ME effect was obtained by applying an AC magnetic field superimposed on a DC magnetic field on the sample. An electromagnet (DCT 5010) controlled by a DC current supply (Sorensen DLM300-13E) was used to provide a DC magnetic field of up to 0.8 T (8 kOe). A multi-purpose FFT analyzer (Ono Sokki CF5220) via a constant-current-supply amplifier (AE Techron 7796) was used to drive the Helmholtz coil to generate an AC magnetic field of 1 Oe with various frequencies ($1\text{--}100\text{ kHz}$). H_{AC} and H_{DC} were monitored in situ by a pick-up coil and a Gaussmeter (F.W. Bell 7030), respectively. The charge generated from the sample was measured by the



multi-purpose FFT analyzer (Ono Sokki CF5220). The ME voltage coefficient is estimated from $\alpha_E = \delta E / \delta H = \delta V / t \cdot \delta H$, where δV is the measured voltage across the sample and t is the sample thickness. All measurements were carried out at room temperature and the direction of the applied magnetic field is parallel to the polarization direction of the samples.

6.3.1 Dielectric property

The frequency dependence of dielectric constant (ϵ_r) at room temperature for all samples is shown in Fig. 6.11 (a). The plots show that the dielectric constant decreases with increase in frequency, showing dispersion in the lower frequency range. This dielectric dispersion is attributed to the Maxwell [188] and Wagner [189] type of interfacial polarization in agreement with Koop's theory. [190] The high value of dielectric constant observed at lower frequencies can be explained on the basis of space charge polarization due to inhomogeneity in structure like impurities, porosity and grain structure [191]. At higher frequencies the dielectric constant remains independent of frequency due to inability of electric dipoles to follow the alternating applied electric field. [192]. These frequency independent values are known as static values of the dielectric constant. From this figure it is observed that the dielectric constant decreases with increase in ferrite content. This is because the dielectric constant of ferrite is lower compared to the ferroelectric phase.

Fig. 6.11 (b) shows variation of dielectric loss ($\tan\delta$) with frequency for the composites. The variation in $\tan\delta$ for all samples is similar to the variations of ϵ_r versus frequency. The room temperature value of the dielectric loss is dependent on the



mole fraction of the individual phases [192]. It is observed that as the fraction of CFO increases, the dielectric loss of the ME composites also increases. This increase in dielectric loss is attributed to the increasing volume fraction of CFO phase in the ME composite. The CFO is a more conductive phase as compared to the PZT502 phase which produces the leakage path for the stored charge carriers resulting in the increase in the dielectric loss.

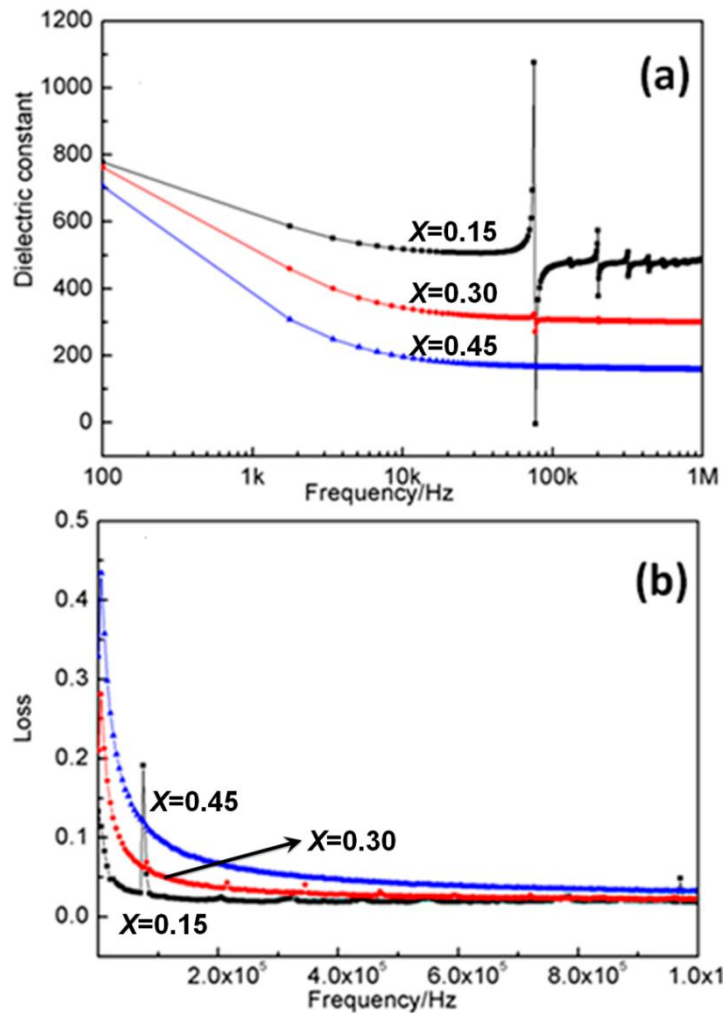


Fig. 6.11 (a) Dielectric constant and (b) loss of x CFO - (1 - x)PZT502 composites. ($x = 0.15, 0.30$ and 0.45)



6.3.2 Ferroelectric property

In the measurement of the ferroelectric hysteresis loop, all the three samples do not break down when the electric field is set to as large as 6 kV/mm, and remnant polarization (P_r) and coercive field (E_c) differs among them (see Fig. 6.12). It is revealed that with the increase of CFO concentration in the composite, E_c increases. This is caused by the steric hindrance from the secondary phase, CFO, which impeded the polarization reversal of PZT. At the same time, P_r decreases with increased CFO concentration. One immediate cause for this is the decrease of PZT fraction from 0.85 to 0.55, whose polarization is the source of P_r .

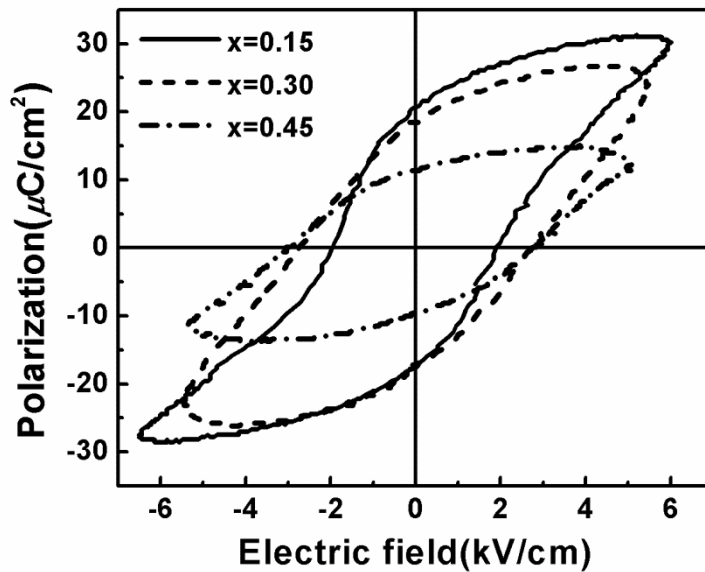


Fig. 6.12 Ferroelectric hysteresis loops of x CFO - $(1 - x)$ PZT502 composites. ($x = 0.15, 0.30$ and 0.45)



6.3.3 Piezoelectric property

The piezoelectric property varies as a function of the ferrite content for the composites, which is shown in Table 6-1. The piezoelectric constant decreases with increase in the volume fraction of CFO due to low resistance of the ferrite phase. Also, with the increase in ferrite content, electrical poling cannot be complete even at high electric field due to the diffusion of low resistant ferrite into the ferroelectric matrix, which deteriorates piezoelectric property of the composites.

Table 6-1 Piezoelectric property of x CFO - (1 - x)PZT502 composites. ($x = 0.15$, 0.30 and 0.45)

x CFO - (1 - x)PZT, x	0.15	0.30	0.45
Poling voltage(kV/mm)	6	6	6
d_{33} (pC/N)	105	50	25

6.3.4 Magnetoelectric property

Figure 6.13 (b) gives the relationship between magnetoelectric coefficient (α_E), and frequency for x CFO - (1 - x)PZT ($x = 0.15$, 0.30, 0.45) composites. Similar variation trends appears for the three samples with different concentrations of CFO. As the frequency increases, α_E increases first, followed by a sharp peak, and decreases to a constant value in the end. The frequency at which the ME coefficient reaches its maximal value is called the electromechanical resonance frequency (f_{EMR}). The value of f_{EMR} is in good agreement with the electromechanical resonance as



shown in Fig. 6.13 (a), which implies that ME resonance is caused by the electromechanical resonance. This means that the piezoelectric component in the composites exhibits its largest property at the frequency of f_{EMR} , and then dominates the ME coupling property. This conclusion also gives the reason why the sample with $x = 0.15$ has the largest α_E at f_{EMR} .

The inset of Fig. 6.13 (b) gives the magnetic field dependence of α_E at EMR frequency for $x\text{CFO} - (1 - x)\text{PZT502}$. There are two factors affecting the relative value of α_E in the three samples, one is the magnetostrictive response caused by CFO, the other is the piezoelectric response caused by PZT. When the magnetic field is small, the first factor dominates, and the sample with more CFO ($x = 0.45$) exhibits larger magnetoelectric coefficient, which is in accordance with theoretical calculations. As the magnetic field increases to a larger value, the effect of voltage loss on the CFO component becomes larger. This leads to an evident decrease of efficient piezoelectric response of PZT, which makes the second factor dominate in the coupling. This is why the sample with most PZT ($x = 0.15$) exhibits the largest ME coefficient at large external magnetic field. These two factor balances at the magnetic field of 2 kOe in our samples.

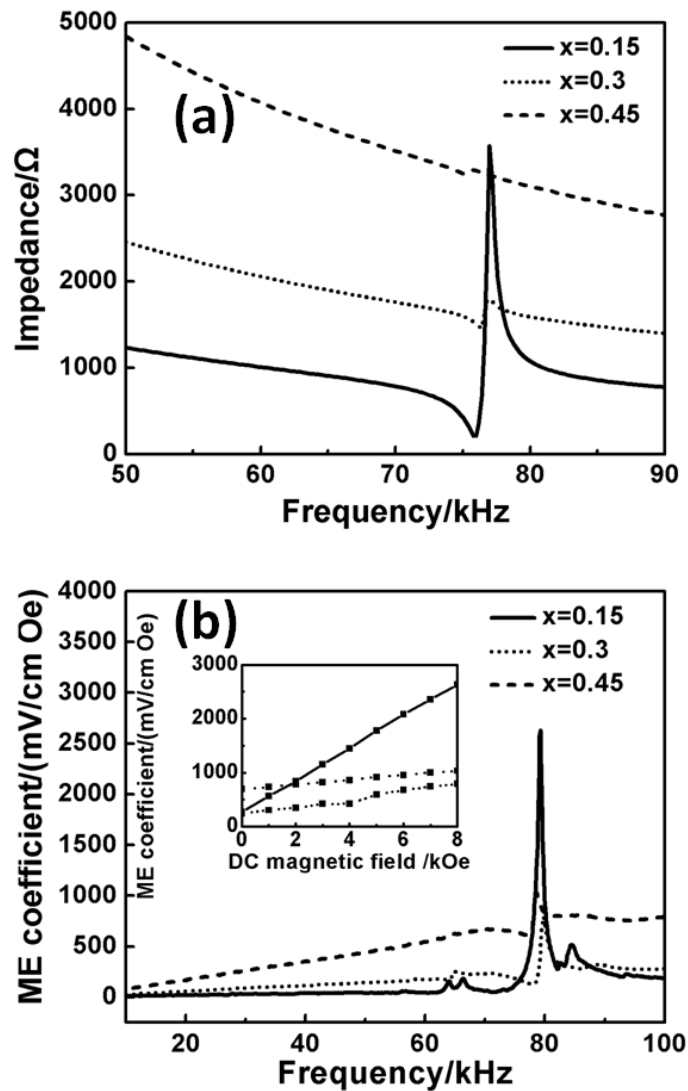


Fig. 6.13 (a) Frequency dependence of impedance for x CFO - $(1 - x)$ PZT502 ($x = 0.15, 0.3$ and 0.45) composites. (b) Variations of α_E with $H_{DC} = 9$ kOe at different frequencies of x CFO - $(1 - x)$ PZT502 composites. The inset is the DC magnetic field dependent variation of α_E at EMR frequency.

6.4 Transformer design

In Section 6.2, a core-shell type microstructure is developed via a wet-chemical method, where CFO (with a grain size \sim tens nm) is the core and a thin layer of insu-



lating metallic oxide (ZrO_2) is the shell. With the shell to act as a barrier to electron and vacancy transportation, the leakage current of the composite material is significantly reduced. A large improvement in ferroelectric properties and an enhanced coupling effect is realized in the ceramics (Section 6.3). In this Section, a piezoelectric transformer has been fabricated using the CFO - PZT composite. The 0.15CFO - 0.85PZT composite is chosen due to its largest piezoelectric property. This transformer structure shows good sensitivity to both DC and AC magnetic field and therefore has potential to be used as detector of magnetic field, especially for weak AC signal. Also, the coupled effect between the magnetoelectric effect and the electromechanical effect allows the output signal tunable via varying the input magnetic/electric signal.

6.4.1 Electrical property of the composite

The DC resistivity of the 0.15CFO - 0.85PZT sample for transformer design is $5.29 \times 10^{12} \Omega \cdot \text{m}$, showing a large resistivity considering the recognized resistivity of PZT ($10^{10} \sim 10^{13} \Omega \cdot \text{m}$), and CFO ($10^6 \sim 10^8 \Omega \cdot \text{m}$).

Complex impedance spectroscopy measurements were also performed to investigate the electronic transport properties of the highly resistive composites. Frequency-dependent impedance data were obtained in the range of 1 kHz to 1 MHz. The impedance Cole-Cole plots of the sample at room temperature is shown in Fig. 6.14. The curve was almost in straight line, indicating the DC conductivity arising from the conducting CFO phase dominates in the composite.

Fig. 6.15 gives the frequency dependence of the real/imaginary part of the



composite's AC impedance. As the frequency increases, the real part of AC impedance increases sharply, and then keeps constant at high frequencies. The imaginary part of the AC impedance shows an opposite variation trend.

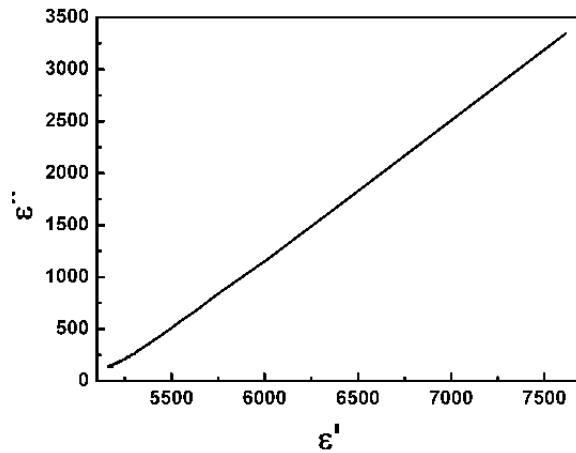


Fig. 6.14 Cole-Cole plots of the 0.15CFO - 0.85PZT sample at room temperature.

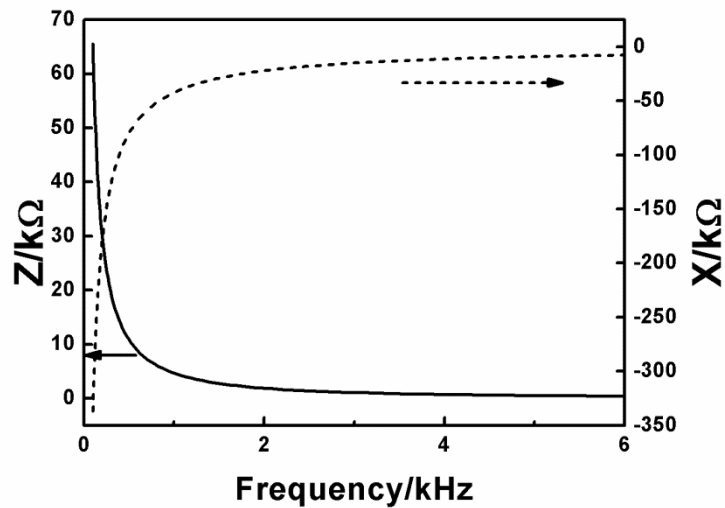


Fig. 6.15 Frequency dependence of the AC impedance's real part and imaginary part for the 0.15CFO - 0.85PZT sample.



6.4.2 The transformer structure

The piezoelectric transformer structure based on our highly resistive 0.15CFO - 0.85PZT composite has a diameter of 26.3 mm and a thickness of 1.2 mm (Fig. 6.16). The piezoelectric poling is conducted to the transformer structure along its thickness direction. One electrode was placed on the external ring surface to input electrical signal, V_{in} . The other two electrodes (with a diameter of 19.3 mm) were made on the upper and lower surface of the ceramic symmetrically for the output signal, V_{out} . When applying an electrical excitation to the external ring, the radial extensional vibration is generated through the converse piezoelectric effect which is propagated to the center of the ceramic, and generates an electrical output signal between the upper and lower electrode via the direct piezoelectric effect. As the distance along the radius direction is larger than that along the thickness direction, the transformer can be considered as a step-down one. The transformer is designed as a step-down one instead of a step-up one because we are focusing not on a large voltage gain but on investigating the coupling effect between the electromechanical-induced signal and the magnetoelectric-induced signal. These two signals couple best when the V_{p-p} (peak-to-peak voltage) is close to each other in value.

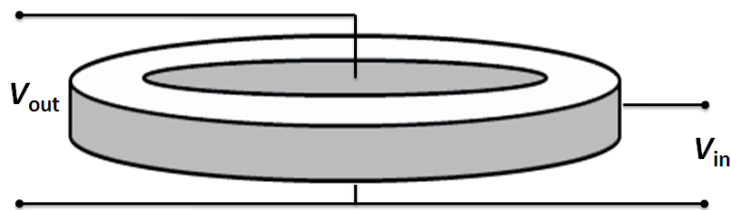


Fig. 6.16 Schematic diagram of the piezoelectric transformer structure.



6.4.3 Impedance spectra of the transformer structure

Fig. 6.17 (a) gives frequency dependence of the designed piezoelectric transformer's impedance. The resonance peak at around 100 kHz is caused by the radial vibration of the ceramic, which is enlarged in Fig. 6.17 (b) to give a clearer view. The resonance frequency is 100.94 kHz.

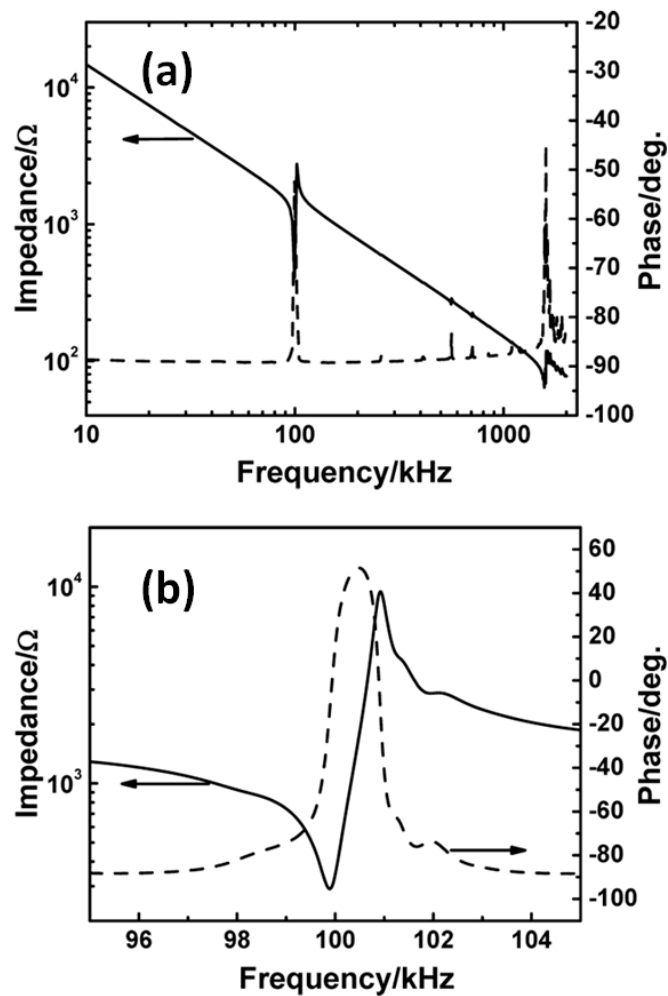


Fig. 6.17 Frequency dependence of the impedance and phase for the transformer structure. (a) 10 - 1250 kHz and (b) 95 - 105 kHz.



6.4.4 The transformer's response to electric/magnetic signal

Fig. 6.18 (a) gives the frequency (around the maximum output voltage) dependence of the transformer's step-down ratio in response to an input voltage of $5 V_{\text{rms}}$. Significant change in the magnitude of the output voltage can be observed over a wide frequency range. The maximum output is achieved at the frequency of 100.83 kHz, which is in good accordance with the structure's resonance frequency shown in the frequency-dependent impedance curve in Fig. 6.17. The output with a DC magnetic field (10 kOe) is also presented in the dash curve to show the influence of DC magnetic field on the transformer's behavior. The current was kept constant in the measurement which is critical to avoid its influence onto the generated magnetic field pattern. It can be noticed that the magnetic field has obvious influence on the frequency dependent property of the transformer's output voltage. In Fig. 6.18 (a), the magnitude of the maximum output voltage at the frequency of 100.83 kHz is $2.57 V_{\text{rms}}$ (input voltage = $5 V_{\text{rms}}$). When an external DC magnetic field of 10 kOe is applied, the maximum output voltage magnitude changes to $2.25 V_{\text{rms}}$ ($\Delta V = 0.19 V_{\text{rms}}$) at the frequency of 101.02 kHz. This result clearly illustrates that the proposed design is sensitive to the DC magnetic field.

Fig. 6.18 (b) gives the output electric voltage between the upper and lower electrodes as a result of an input AC magnetic field (20Oe), which reveals the magnetoelectric coupling effect in the composite. The AC magnetic field was generated by a Helmholtz coil. The diameter of the Cu wire is 0.2 mm, and its total weight is 0.5 kg. The resistivity of the coil is 642Ω at 50 Hz and $3.4 \text{ k}\Omega$ at 40 kHz. The driving voltage to generate a magnetic field is 30 V and the corresponding magnetic field is 20 Oe. The magnetoelectric resonance peak is found at the frequency of 101.1 kHz with



an output voltage of 186 mV, indicating that the magnetoelectric resonance is dominated by the electromechanical resonance in the structure. Also, the output electric signal is found to have the same waveform as the input magnetic signal during the measurement.

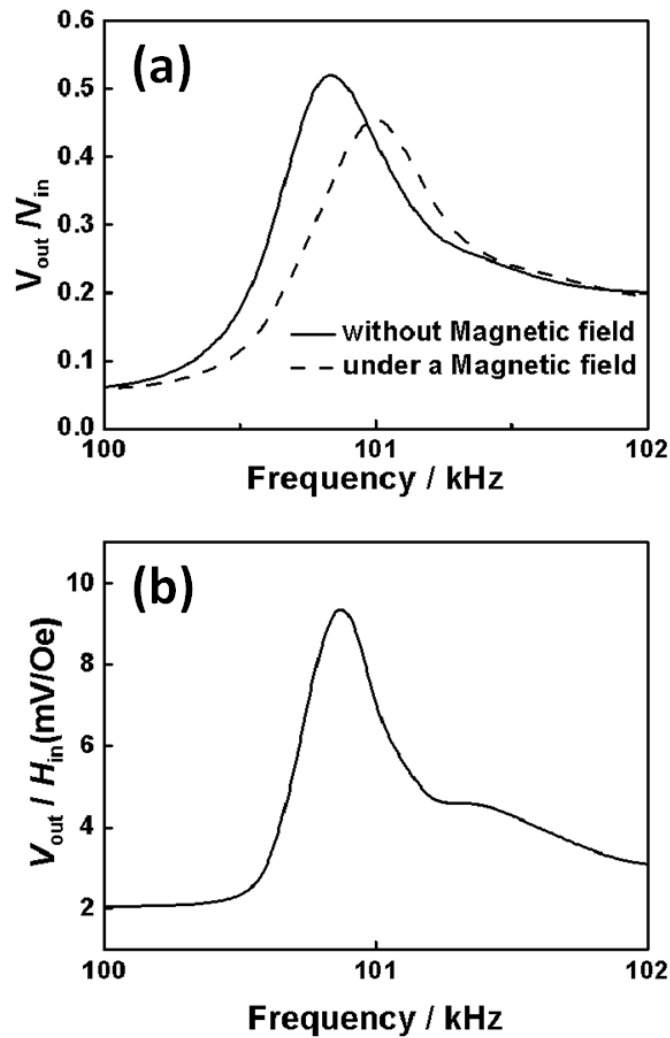


Fig. 6.18 The transformer's response to (a) AC electric signal and (b) AC magnetic signal.



6.4.5 Coupled effect in the transformer

The coupled effect of the AC magnetic input signal and the AC electric input signal on the output electric signal has also been investigated. The magnetic sinusoidal signal is generated by the same Helmholtz coil mentioned before (~ 20 Oe, driven by an electric voltage of 20 V), which generates an output signal (Fig. 6.19 (a)) via the magnetoelectric effect. The input electric sinusoidal signal ($2 V_{\text{rms}}$) is applied between the lower electrode and the outer ring electrode, which generates an output signal between the upper and lower electrodes (Fig. 6.19 (b)) via the step-down transformer. The coupled output is presented in Fig. 6.19 (c), showing a coupling between the magnetoelectric behavior and the piezoelectric behavior. It is also observed that the output signal can be tuned by changing the frequency of the input magnetic/electric signal.

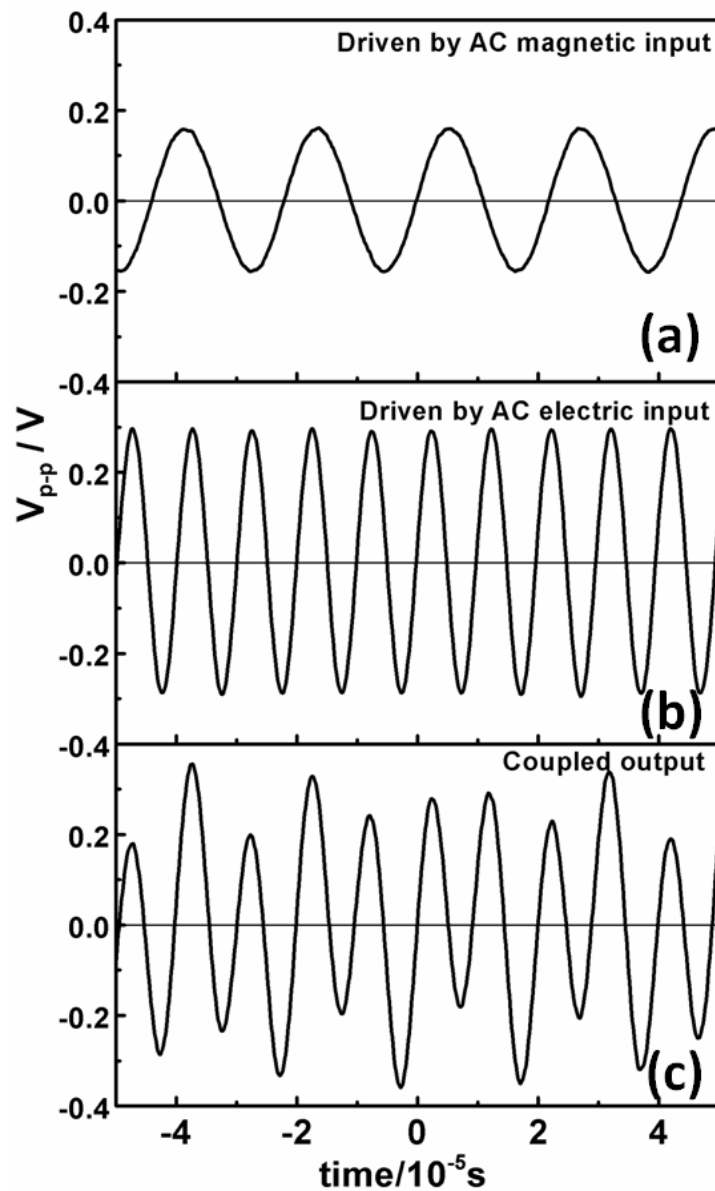


Fig. 6.19 The coupled effect of the AC magnetic input signal and the AC electric input signal on the output electric signal. (a) The output signal driven by AC magnetic input signal, (b) the output signal driven by AC electric input signal and (c) the output signal driven by coupled AC magnetic and AC electric input signals.



6.5 Summary

In this Chapter, 0 - 3 type CFO - PZT composites with enhanced piezoelectric coefficient have been synthesized by introducing a thin layer of ZrO_2 around the CFO particles which serves as a blocking layer to avoid electrical percolation and therefore improve the percolation threshold of the composite system. A magnetic-tunable piezoelectric transformer has been fabricated based on its piezoelectric feature. The transformer shows good sensitivity to both input electric signal and magnetic signal. It also has potential to be used to fabricate devices to detect weak magnetic field and as magnetic-field-tunable transformers.



CHAPTER 7

Conclusion and future work

7.1 Conclusion

In the course of this study, the microstructure - property relationship in 0 - 3 type $\text{Pb}(\text{Zr}, \text{Ti})\text{O}_3$ - CoFe_2O_4 (PZT - CFO) magnetolectric composites is investigated both experimentally and theoretically. Firstly, the lattice coupling between PZT and CFO under a static electric field is studied via in-situ X-ray diffraction. Based on the lattice coupling, the relationship between lattice strain and the ME coupling coefficient is investigated. Secondly, a numerical approach based on the finite element analysis method is proposed to deal with magnetolectric composites with complex structures. An evaluation method is developed to judge the interfacial coupling efficiency between any two components with any given structures. Thirdly, the inhomogeneity of internal electric field is studied theoretically based on the FEM modeling. Its influence on the poling efficiency, component performance and coupling effect is studied. Fourthly, a 0 - 3 type composite with core-shell type microstructure is prepared aiming at improving the poling efficiency, the electric/piezoelectric property and the magnetolectric property. This composite is then used to fabricate a magnetically tunable piezoelectric transformer based on its excellent piezoelectric and magnetolectric performance, demonstrating the possible application in industry. The main conclusions can be summarized as follows:

- 1) We have investigated the crystalline structure of PZT - CFO particulate composites under electric field via X-ray diffraction. Particularly, the lattice strain



within its two components is studied. The PZT - CFO particulate composites were prepared by conventional ceramic sintering process. According to the microstructure and XRD characterization under no external field, the composites were of high crystalline quality. A clear interface existed between PZT and CFO, indicating a direct contact without any second phases. When applying a static electric field to the composites, coupled distortion in crystal lattice of both components was observed. The change in lattice parameter under external field gives direct evidence for the mechanical interaction between these two phases. This is the first observed evidence for the coupling in 0 - 3 type magnetoelectric composites in the scale of grain lattice. Besides, we established a correlation between lattice distortion and the magnetoelectric coupling effect. Simple models were proposed to estimate the ME coupling coefficient based on the mechanical interaction under ideal cases.

2) A self-consistent numerical method is developed to simulate the ME coupling coefficient for composites with any given structures. This method is based on the finite element analysis method. With this method, the relationship between output electric field and input magnetic field can be simulated directly. Two examples with typical 1 - 3 and 0 - 3 type structures were given. In particular, to simulate the ME effect in 0 - 3 type composites, a Monte - Carlo method is introduced to model the random distribution of CFO particles. The simulation results, including both ME coefficients and its dependence on the magnetic fields, is in good accordance with the reported experimental results in literature.

3) A method based on lattice coincidence is proposed to evaluate the coupling efficiency (k_c) in ME composites. The components can be of any given lattice struc-



tures and orientations. By taking the lattice structures into account, this method explains the dependence of magnetoelectric effect on material selection. And by including the lattice orientation effect, the method explains why materials connected with different connectivity lead to distinguished coupling property. This evaluation system can help to select materials and compositing structures in order to get a large coupling effect.

4) The inhomogeneous internal electric field in 0 - 3 type ME composites was simulated via a finite element analysis method. It was found that the large inhomogeneity influences the ME coupling effect in two ways. One is to inhibit efficient poling of the piezoelectric phase before application. The other is to weaken the efficient piezoelectric performance under application. The local piezoelectric coefficient under a DC electric field was studied in detail. It has been proposed that the introduction of the magnetic phase causes large divergence in property of the piezoelectric phase. Such weakening concentrates in the interaction areas between PZT and CFO, indicating that it may cause an enlarged weakening in the overall magnetoelectric effect.

5) 0 - 3 type CFO - PZT composites with enhanced piezoelectric coefficient have been synthesized by introducing a thin layer of ZrO_2 around the CFO particles which serves as a blocking layer to avoid electrical percolation and therefore improve the percolation threshold of the composite system. A magnetic-tunable piezoelectric transformer has been fabricated based on its piezoelectric feature. The transformer shows good sensitivity to both input electric signal and magnetic signal. It also has potential to be used to fabricate devices to detect weak magnetic field and as



magnetic field-tunable transformers.

7.2 Future work

We investigated the mechanical coupling between the magnetic phase and the piezoelectric phase in 0 - 3 type composites upon a given electric fields. However, further work is still needed to develop a thorough understanding about the mechanism of such mechanical interaction, including: (1) The influence of the orientation of the static electric field on the lattice distortion; (2) The relationship between the magnitude of the electric field and the lattice distortion; (3) The lattice distortion at AC electric field and at resonant frequency.

Besides, restricted by the experimental condition, our experiment did not include the influence of magnetic field, which could be studied in later work. The experimental method can also be conducted to other combinations of materials with varied structures to establish a relationship between the lattice distortion and the selection of materials, which may provide an experimental evidence for the different coupling factor in various composite systems.

Using the X-ray diffraction, we investigate the coupling in ME composite in the level of grain lattice. Further work can also try to use other analytical method to characterize the coupling. For example, using the Raman spectra, we can observe how different functional groups in the components acts under external field.

Although we have successfully used the finite element analysis method to explore the magnetoelectric composites with any given structures, the simulation method focuses on the static condition. It is desirable to have a more comprehensive



model for more complex field conditions. The resonant magnetoelectric effect should also be studied.

We have proposed an interface coordination factor to evaluate the coupling efficiency (i.e., the coupling factor, k_c), which explains the coupling efficiency in material systems with different connectivity. Apart from the match of lattice at the interface, the state of the material far from the interface can also be a factor influencing the coupling factor, k_c . Further work will continue to include other possible factors which may influence k_c into the evaluation method. Also, the condition for materials with preferred orientation can be studied.

The influence of non-uniform electric field on the local material performance is studied in detail. While its influence on the poling behavior still needs a further discussion. Besides, the electric field can be extended to AC field.

We have used ZrO_2 as a highly resistive shell to improve the electric property of the PZT - CFO matrix. Different shell materials can be considered in further work, such as TiO_2 and SiO_2 . The preparation method, such as in - situ preparation of the core-shell particles and other sintering methods of the ceramics (e.g., SPS), can also be used.

The design of magnetic tunable piezoelectric transformer could be optimized, eg. the size and shape of the transformer can be designed to suit different use. Moreover, the electrode fabrication process need to be further improved to decrease the loss.



Reference

- 1) C. W. Nan, M. I. Bichurin, S. X. Dong, D. Viehland and G. Srinivasan, *J. Appl. Phys.* 103, 031101 (2008).
- 2) S. Priya, R. Islam, S. X. Dong and D. Viehland, *J. Electroceram.* 19, 147 (2007).
- 3) J. Ryu, S. Priya, K. Uchino and H. E. Kim, *J. Electroceram.* 8, 107 (2002).
- 4) Manfred Fiebig, *J. Phys. D: Appl. Phys.* 38, R123 (2005).
- 5) W. C. Röntgen, *Ann. Phys.* 35, 264 (1888).
- 6) H. A. Wilson, *Phil. Trans. R. Soc. A*204, 129 (1905).
- 7) P. Curie, *J. de Physique (3rd Series)* 3, 393 (1894).
- 8) L. D. Landau and E. Lifshitz, *Electrodynamics of Continuous Media* (Addison-Wesley: Translation of a Russian edition of 1958), (1960).
- 9) I. E. Dzyaloshinskii, *Sov. Phys.-JETP* 37, 628 (1960).
- 10) D. N. Astrov, *Sov. Phys.-JETP* 11, 708 (1960).
- 11) G. T. Rado, V. J. Folen and E. W. Stalder, *Phys. Rev. Lett.* 7, 310 (1961).
- 12) B. I. Alshin and D. N. Astrov, *Sov. Phys. JETP* 17, 809 (1963).
- 13) G. T. Rado, *Phys. Rev. Lett.* 13, 335 (1964).
- 14) E. Ascher, H. Rieder, H. Schmid and H. Stossel, *J. Appl. Phys.* 37, 1404(1966).
- 15) R. P. Santoro, D. J. Segal and R. E. Newnham, *J. Phys. Chem. Solids* 27, 1192(1966).
- 16) T. Watanabe, K. Kohn, *Phase Trans.* 15, 57 (1989).
- 17) T. H. O'Dell, *Phil. Mag.* 16, 487 (1967).



- 18) B. B. Krichevtsov, V. V. Pavlov, R. V. Pisarev and A. G. Selitsky, *Ferroelectrics* 161, 65 (1993).
- 19) H. Schmid H, *Int. J. Magn.* 4, 337(1973).
- 20) Y. N. Venevtsev, V. V. Gagulin and I. D. Zhitomirsky, *Ferroelectrics* 73, 221 (1987).
- 21) S. M. Skinner, *IEEE Trans. Parts, Mater. Packaging* 6, 68 (1970).
- 22) F. Kubel and H. Schmid, *Acta Crystallogr. B* 46, 698 (1970).
- 23) S. V. Kizelev, R. P. Ozerov and G. S. Zhdanov, *Sov.Phys.-Dokl.* 145, 1255 (1962).
- 24) C. Moure, M. Villegas, J. F. Fernandez, J. Tartaj and P. Duran, *J. Mater. Sci.* 34, 2565 (1999).
- 25) B. B. van Aken, J. W. G. Bos, R. A. de Groot, and T. T. M. Palstra, *Phys. Rev. B* 63, 125127 (2001).
- 26) M. Bieringer, J. E. Greedan and A. S. Wills, *Appl. Phys. A* 74, S601 (2002).
- 27) N. Fujimura, H. Sakata, D. Ito, T. Yoshimura, T. Yokota and T. Ito, *J. Appl. Phys.* 93, 6990 (2003).
- 28) E. Ascher, H. Schmid and D. Tar, *Solid State Commun.* 2, 45 (1964).
- 29) H. Schmid, H. Rieder and E. Ascher, *Solid State Commun.* 3, 327(1965).
- 30) J. F. Scott, *Ferroelectrics* 24, 127(1980).
- 31) M. Eibschütz and H. J. Guggenheim, *Solid State Commun.* 6, 737 (1968).
- 32) J. Van Suchetelene, *Philips Res. Rep.* 27, 28 (1972).
- 33) C. W. Nan, *Phys. Rev. B* 50, 6082 (1994).
- 34) R. E. Newnham, D. P. Skinner and L. E. Cross, *Mater. Res. Bull.* 13, 525 (1978).



-
- 35) C. W. Nan, *Prog. Mater. Sci.* 37(1), 1 (1993).
 - 36) H. J. A. Molegraaf, J. Hoffman, C. A. F. Vaz, S. Gariglio, D. VanDerMare, C. H. Ahn and J. M. Triscone, *Adv. Mater.* 21, 3470 (2009).
 - 37) A. M. J. G. Run, D. R. Terrell and J. H. Scholing, *J. Mater. Sci.* 9, 1710 (1974).
 - 38) J. van den Boomgaard, A. M. J. G. Van Run, and J. Van Suchetelene, *Ferroelectrics*, 10, 295 (1976).
 - 39) J. Boomgard and R. A. J. Born, *J. Mater. Sci.* 13, 1538 (1978).
 - 40) J. Boomgard, D. R. Terrell, R. A. J. Born and H. F. J. I. Giller, *J. Mater. Sci.* 9, 1705(1974).
 - 41) I. Bunget and V. Raetchi, *Rev. Roum. Phys.* 27, 401 (1982).
 - 42) R. P. Mahajan, K. K. Patankar, A. N. Patil, S. C. Chaudhari, A. K. Ghatge and S. A. Patil, *Indian J. Eng. Mater. Sci.* 7, 203 (2000).
 - 43) M. B. Kothale, K. K. Patankar, S. L. Kadamb, V. L. Mathe, A. V. Raob and B. K. Chougule, *Mater. Chem. Phys.* 77, 691 (2002).
 - 44) M. I. Bichurin, V. M. Petrov, R. V. Petrov, Y. V. Kiliba, F. I. Bukashev, A. Y. Smirnov and D. V. Eliseev, *Ferroelectrics* 280, 365 (2002).
 - 45) S. L. Kadam, K. K. Patankar, V. L. Mathe, M. B. Kothale, R. B. Kale and B. K. Chougule, *Mater. Chem. Phys.* 78, 684 (2002).
 - 46) G. Srinivasan, E. T. Rasmussen and R. Hayes, *Phys. Rev. B* 67, 014418 (2003).
 - 47) J. Y. Zhai, N. Cai, L. Liu, Y. H. Lin and C. W. Nan, *Mater. Sci. Eng. B* 99, 329 (2003).



-
- 48) Y. R. Dai, P. Bao, J. S. Zhu, H. M. Shen, J. M. Liu and Y. N. Wang, *Acta Metall. Sin.* 39, 1209 (2003).
 - 49) G. Srinivasan, E. T. Rasmussen, A. A. Bush, K. E. Kamentsev, V. F. Meshcheryakov and Y. K. Fetisov, *Appl. Phys. A* 78, 721(2004).
 - 50) G. Engdahl, *Handbook of Giant Magnetoresistive Materials* (New York: Academic) (2000).
 - 51) J. Ryu, A. V. Carazo, K. Uchino and H. E. Kim, *Japan. J. Appl. Phys.* 40, 4948 (2001).
 - 52) J. H. Ryu, S. Priya, A. V. Carazo, K. Uchino and H. E. Kim, *J. Am. Ceram. Soc.* 84, 2905 (2001).
 - 53) J. G. Wan, J. M. Liu, H. L. W. Chand, C. L. Choy, G. H. Wang and C. W. Nan, *J. Appl. Phys.* 93, 9916 (2003)
 - 54) S. X. Dong, J. F. Li, and D. Viehland, *IEEE Trans. Ultrason. Ferroelectr. Freq. Control* 50, 1253 (2003).
 - 55) S. X. Dong, J. R. Cheng, J. F. Li and D. Viehland, *Appl. Phys. Lett.* 83, 4812 (2003).
 - 56) S. X. Dong, J. F. Li and D. Viehland, *J. Appl. Phys.* 95, 2625 (2004).
 - 57) J. F. Li and D. Viehland, *Appl. Phys. Lett.* 84, 4188 (2004).
 - 58) M. Zeng, J. G. Wan, Y. Wang, H. Yu, J. M. Liu, X. P. Jiang and C. W. Nan, *J. Appl. Phys.* 95, 8069 (2004).
 - 59) S. X. Dong, J. F. Li and D. Viehland, *IEEE Trans. Ultrason. Ferroelectr. Freq. Control* 51, 794 (2004).
 - 60) N. Nersessian, S. W. Or and G. P. Carman, *IEEE Trans. Magn.* 40, 2646 (2004).



- 61) S. X. Dong, J. F. Li and D. Viehland, *J. Appl. Phys.* 96, 3382 (2004).
- 62) A. Bayrashev, W. P. Robbins and B. Ziaie, *Sensors Actuators A* 114, 244 (2004).
- 63) S. X. Dong, J. F. Li and D. Viehland, *Appl. Phys. Lett.* 85, 2307 (2004).
- 64) J. Kuwata, K. Uchino and S. Nomura, *Ferroelectrics* 37, 579 (1981).
- 65) J. Kuwata, K. Uchino and S. Nomura, *Japan. J. Appl. Phys.* 21, 1298 (1982).
- 66) K. K. Patankar, R. P. Nipankar, V. L. Mathe, R. P. Mahajan and S. A. Patil, *Ceram. Int.* 27, 853 (2001).
- 67) K. Mori and M. Wuttig, *Appl. Phys. Lett.* 81, 100 (2002)
- 68) V. L. Mathe, K. K. Patankar, U. V. Jadhav, A. N. Patil, S. D. Lotake and S. A. Patil, *Ceram. Int.* 27, 531 (2000).
- 69) S. X. Dong, J. F. Li and D. Viehland, *Appl. Phys. Lett.* 83, 2265 (2003).
- 70) G. Srinivasan, E. T. Rasmussen, B. J. Levin and R. Hayes, *Phys. Rev.B* 65, 134402 (2002).
- 71) S. Shastry, G. Srinivasan, M. I. Bichurin, V. M. Petrov and A. S. Tatarenko, *Phys. Rev.B* 70, 064416 (2004).
- 72) U. Laletsin, N. Padubnaya, G. Srinivasan and C. P. Devreugd, *Appl. Phys. A* 78, 33 (2004).
- 73) A. E. Clark, in: E.P. Wohlfarth (Ed.), *Ferromagnetic Materials*, Amsterdam, North Holland (1980).
- 74) E. du Trémolet de Lacheisserie, *Magnetostriction Theory and Applications of Magnetoelasticity*, CRC Press, Boca Raton (1993).
- 75) J. Smit and H. P. J. Wijn, in *Ferrites*, Philips Technical Library, Eindhoven, Netherlands (1959).



-
- 76) APC International, Piezoelectric Ceramics, Mackeyville, PA (2000).
 - 77) S. Park and T. Shrout, *IEEE Trans. Ultrason. Ferroelect. Freq. Contr.* 44(5), 1140 (1997).
 - 78) T. Ikeda, Fundamentals of Piezoelectricity, Oxford University Press, New York (1990).
 - 79) L. Bornstein, Series on Ferroelectric Oxides, Springer Verlag, Berlin Heidelberg (1999).
 - 80) J. Lekkala, J. Tuppurainen and M. Paaajanen, Material and operational properties of large-area membrane type sensors for smart environments, IM-EKO World Congress, Dubrovnik, Croatia (2003).
 - 81) V. E. Wood and A. E. Austin, *Int. J. Magn.* 5, 303 (1973).
 - 82) M. I. Bichurin, V. M. Petrov, Y. V. Kiliba and G. Srinivasan, *Phys. Rev. B* 66, 134404 (2002).
 - 83) G. Srinivasan, E. T. Rasmussen, J. Gallegos, R. Srinivasan, Y. I. Bokhan and V. M. Laletin, *Phys. Rev. B* 64, 214408 (2001).
 - 84) J. P. Zhou, H. C. He, Z. Shi, G. Liu and C. W. Nan, *J. Appl. Phys.* 100, 094106 (2006).
 - 85) R. A. Islam and S. Priya, *Appl. Phys. Lett.* 89, 152911 (2006).
 - 86) N. Zhang, W. Ke, and T. Schneider, *J. Phys.: Condens. Matter* 18, 11013 (2006).
 - 87) I. V. Lisnevskaya, I. A. Bobrova and E. A. Bikyashev, *Inorg. Mater.* 42, 1147 (2006).
 - 88) G. Srinivasan, I. V. Zavislyak and A. S. Tatarenko, *Appl. Phys. Lett.* 89, 152508 (2006).



-
- 89) Y. H. Lin, N. Cai, J. Y. Zhai, G. Liu and C. W. Nan, *Phys. Rev. B* 72, 012405 (2005)
- 90) D. Seguin, M. Sunder, L. Krishna, A. Tatarenko and P. D. Moran, *J. Cryst. Growth* 311, 3235 (2009).
- 91) J. J. Yang, Y. G. Zhao, H. F. Tian, L. B. Luo, H. Y. Zhang, Y. J. He and H. S. Luo, *Appl. Phys. Lett.* 94, 212504 (2009).
- 92) Y. Wu, J. Wan, C. Huang, Y. Weng, S. Zhao, J. Liu and G. Wang, *Appl. Phys. Lett.* 93, 192915 (2008).
- 93) N. Ortega, A. Kumar, P. Bhattacharya, S. B. Majumder, and R. S. Katiyar, *Phys. Rev. B* 77, 014111 (2008).
- 94) J. Ma, Z. Shi and C. W. Nan, *Adv. Mater.* 19, 2571 (2007).
- 95) Z. Shi, C. W. Nan, J. Zhang, J. Ma and J. F. Li, *J. Appl. Phys.* 99, 124108 (2006).
- 96) T. Li, S. W. Or and H. L. W. Chan, *J. Magn. Magn. Mater.* 304, e442 (2006).
- 97) A. Singh and R. Chatterjee, *Appl. Phys. Lett.* 93, 182908 (2008).
- 98) R. A. Islam, J. Jiang, F. Bai, D. Viehland and S. Priya, *Appl. Phys. Lett.* 91, 162905 (2007)
- 99) S. Ren, R. M. Briber and M. Wuttig, *Appl. Phys. Letts.* 93, 173507 (2008).
- 100) S. H. Xie, J. Y. Li, Y. Qiao, Y. Y. Liu, L. N. Lan, Y. C. Zhou and S. T. Tan, *Appl. Phys. Lett.* 92, 062901 (2008).
- 101) L. Mitoseriu, V. Buscaglia, M. Viviani, M. T. Buscaglia, I. Pallecchi, C. Harnagea, A. Testino, V. Trefiletti, P. Nanni and A. S. Siri, *J. Eur. Ceram. Soc.* 27, 4379 (2007).



-
- 102) B. K. Bammannavar, G. N. Chavana, L. R. Naik and B. K. Chougule, *Mater. Chem. Phys.* 117, 46 (2009).
- 103) Y. Q. Lin and X. M. Chen, *Mater. Chem. Phys.* 117, 125 (2009).
- 104) J. Shen, J. Zhou, B. Li and L. Li, *Mater. Lett.* 60, 1071 (2006).
- 105) Y. R. Dai, P. Bao, J. S. Zhu, J. G. Wan, H. M. Shen and J. M. Liu, *J. Appl. Phys.* 96(10), 5687 (2004).
- 106) Y. B. Kamble, S. S. Chougule and B. K. Chougule, *J. Alloys Compd.* 476, 733 (2009).
- 107) L. Jia, S. Chen, H. Zhang and Z. Zhong, *Mater. Chem. Phys.* 114, 697 (2009).
- 108) J. L. Chen, Z. Xu, S. B. Qu, X. Y. Wei and X. H. Liu, *Ceram. Int.* 34, 803 (2008).
- 109) C. A. Randall, N. Kim, J. P. Kucera, W. Cao, and T. R. ShROUT, *J. Am. Ceram. Soc.* 81, 677 (1998).
- 110) M. I. Bichurin, D. A. Filippov, V. M. Petrov, V. M. Laletsin, N. Paddubnaya, G. Srinivasan, *Phys. Rev. B* 68, 054402 (2003).
- 111) V. M. Petrov, G. Srinivasan, V. Laletsin and M. I. Bichurin, *Phys. Rev. B* 75, 174422 (2007).
- 112) G. Srinivasan, R. C. P. DeVreugd, C. S. Flattery, V. M. Laletsin and N. Paddubnaya, *Appl. Phys. Lett.* 85, 2550 (2004).
- 113) Q. H. Jiang, Z. J. Shen, J. P. Zhou, Z. Shi and C. W. Nan, *J. Eur. Ceram. Soc.* 27,279 (2007).
- 114) Z. J. Shen and M. Nygren, *Chem. Rec.* 5, 173 (2005).



-
- 115) S. L. Kadam, C. M. Kanamadi, K. K. Patankar and B. K. Chougule, *Mater. Letters* 59, 215 (2005).
- 116) K. K. Patankar, V. L. Mathe, R. P. Mahajan, S. A. Patil, R. M. Reddy and K. V. SivaKumar, *Mater. Chem. Phys.* 72, 23 (2001).
- 117) K. K. Patankar, V. L. Mathe, A. N. Patil, S. A. Patil, S. D. Lotke, Y. D. Kolekar and P. B. Joshi, *J. Electroceram.* 6, 115 (2001).
- 118) K. K. Patankar, P. D. Dombale, V. L. Mathe, S. A. Patil and R. N. Patil, *Mater. Sci. Eng., B* 87, 53 (2001).
- 119) R. P. Mahajan, K. K. Patankar, M. B. Kothale and S. A. Patil, *Bull. Mater. Sci.* 23, 273 (2000).
- 120) S. A. P. K. K. Patankar, K. V. Sivakumar, R. P. Mahajan, Y. D. Kolekar and M. B. Kothale, *Mater. Chem. Phys.* 65, 97 (2000).
- 121) G. Srinivasan, V. Laletsin, R. Hayes, N. Puddubnaya, E. T. Rasmussen and D. J. Fekel, *Solid State Commun.* 124, 373 (2002).
- 122) S. Q. Ren, L. Q. Weng and S. H. Song, *J. Mater. Sci.* 40, 4375 (2005).
- 123) L. Q. Weng, Y. D. Fu and S. H. Song, *Scr. Mater.* 56, 465 (2007).
- 124) J. G. Wan, H. Zhang and X. W. Wang, *Appl. Phys. Lett.* 89, 122914 (2006).
- 125) V. Corral-Flores, D. Bueno-Baques and D. Carrillo-Flores, *J. Appl. Phys.* 99, 08J503 (2006).
- 126) K. Ban, M. Gomi, T. Shundo and N. Nishimura, *IEEE Trans. Magn.* 41, 2793 (2005).
- 127) A. S. Zubkov, *Elektrichestvo* 10, 77 (1978).



-
- 128) G. Harshe, J. P. Dougherty and R. E. Newnham, *Int. J. Appl. Electromagn. Mater.* 4, 161 (1993); G. Harshe, J. P. Dougherty and R. E. Newnham, *Int. J. Appl. Electromagn. Mater.* 4, 145 (1993).
- 129) J. Y. Li and M. L. Dunn, *Philos. Mag. A* 77, 1341 (1998).
- 130) J. Y. Li, *Int. J. Eng. Sci.* 38, 1993 (2000).
- 131) Q. J. Mech, *Appl. Math.* 56, 35 (2003).
- 132) S. Srinivas and J. Y. Li, *Acta Mater.* 53, 4135 (2005).
- 133) S. Srinivas, J. Y. Li and Y. C. Zhou, *J. Appl. Phys.* 99, 043905 (2006).
- 134) L. J. Li and J. Y. Li, *Phys. Rev. B* 73, 184416 (2006).
- 135) J. H. Huang and W. S. Kuo, *J. Appl. Phys.* 81, 1378 (1997).
- 136) J. H. Huang, *Phys. Rev. B* 58, 12 (1998).
- 137) T. L. Wu and J. H. Huang, *Int. J. Solids Struct.* 37, 2981 (2000).
- 138) C. D. Lorenz and R. M. Ziff, *Phys. Rev. E* 57, 230 (1998).
- 139) C. D. Lorenz and R. M. Ziff, *J. Chem. Phys.* 114, 3659 (2001).
- 140) Z. Yu and C. Ang, *J. Mater. Sci.: Mater. Electron.* 13, 193 (2002).
- 141) Z. Yu and C. Ang, *J. Appl. Phys.* 91, 794 (2002).
- 142) S. Lopatin, I. Lopatina and I. Lisnevskaya, *Ferroelectrics* 162, 63 (1994).
- 143) C. B. Sawyer and C. H. Tower, *Physical Review* 35, 269 (1930).
- 144) A. J. Steinfort, P. M. L. O. Scholte, A. Ettema, F. Tuinstra, *Phys. Rev. Lett.* 77, 2009 (1996).
- 145) Z. Li, Y. Wang, Y. H. Lin and C. W. Nan, *Phys. Rev. B* 79, 180406(R)(2009).
- 146) R. K. Zheng, Y. Wang, H. L. W. Chan, C. L. Choy and H. S. Luo, *Appl. Phys. Lett.* 92, 082908 (2008).



-
- 147) R. K. Zheng, Y. Jiang, Y. Wang, H. L. W. Chan, C. L. Choy and H. S. Luo, *Appl. Phys. Lett.* 93, 102904 (2008).
- 148) G. R. Harsh é Ph.D. thesis, Pennsylvania State University, (1991).
- 149) M. I. Bichurin, V. M. Petrov and G. Srinivasan, *J. Appl. Phys.* 92 (12), 7681 (2002).
- 150) S. X. Dong, J. Y. Zhai, J. F. Li, D. Viehland and S. Priya, *Appl. Phys. Lett.* 93 (10), 103511 (2008).
- 151) G. Liu, C. W. Nan, N. Cai and Y. H. Lin, *J. Appl. Phys.* 95 (5), 2660 (2004).
- 152) C. W. Nan, Y. H. Lin and J. H. Huang, *Ferroelectrics* 280, 319 (2002).
- 153) C. W. Nan, M. Li and J. H. Huang, *Phys. Rev. B* 63 (14), 144415 (2001).
- 154) C. W. Nan, M. Li, X. Q. Feng and S. W. Yu, *Appl. Phys. Lett.* 78 (17), 2527 (2001).
- 155) Y. X. Liu, J. G. Wan, J. M. Liu and C. W. Nan, *J. Appl. Phys.* 94 (8), 5111 (2003).
- 156) S. Chikazumi, *Physics of ferromagnetism*, Oxford University Press, Oxford (2005).
- 157) COMSOL Group, Nonlinear magnetostrictive transducer, COMSOL Model Gallery, 6063.
- 158) C. Mudivarthi, S. Datta, J. Atulasimha and A. B. Flatau, *Smart Mater. Struct.* 17, 035005 (2008).
- 159) Z. Shi, C. W. Nan, J. Zhang, N. Cai and J. F. Li, *Appl. Phys. Lett.* 87, 012503 (2005).
- 160) T. G. Lupeiko, I. V. Lisnevskaya, M. D. Chkheidze and B. I. Zvyagintsev, *Inorg. Mater.* 31, 1245 (1995).



-
- 161) M. I. Bichurin, I. A. Kornev, V. M. Petrov and I. Lisnevskaya, *Ferroelectrics* 204, 289 (1997).
- 162) J. Ryu, A. V. Carazo, K. Uchino and H. E. Kim, *J. Electroceram.* 7, 17 (2001).
- 163) J. Y. Zhai, N. Cai, Z. Shi, Y. H. Lin and C. W. Nan, *J. Phys. D* 37, 823 (2004).
- 164) J. Y. Zhai, N. Cai, Z. Shi, Y. H. Lin and C. W. Nan, *J. Appl. Phys.* 95, 5685 (2004).
- 165) X. M. Chen, Y. H. Tang and I. W. Chen, *J. Appl. Phys.* 96, 6520 (2004).
- 166) Y. H. Tang, X. M. Chen and Y. J. Li, *Mater. Sci. Eng., B* 116, 150(2005).
- 167) M. Sayer, B. A. Judd, K. Ellassal and E. Prasad, *J. Can. Ceram. Soc.* 50, 23 (1981).
- 168) D. W. Stroock, *Probability Theory: An Analytic View*, Cambridge University Press, Cambridge (1993).
- 169) M. H. Lee, A. Halliyal and R. E. Newnham, *Ferroelectrics* 87, 71 (1988).
- 170) T. Granzow, A. B. Kounga, E. Aulbach and J. Rodel, *Appl. Phys. Lett.* 88, 252907 (2006).
- 171) Y. S. Koo, T. Bonaedy, K. D. Sung, J. H. Jung, J. B. Yoon, Y. H. Jo, M. H. Jung, H. J. Lee, T. Y. Koo and Y. H. Jeong, *Appl. Phys. Lett.* 91, 212903 (2007).
- 172) R. A. Islam, V. Bedekar, N. Poudyal, J. P. Liu, and S. Priya, *J. Appl. Phys.* 104, 104111 (2008).
- 173) L. P. Curecheriu, M. T. Buscaglia, V. Buscaglia, L. Mitoseriu, P. Postolache, A. Ianculescu, and P. Nanni, *J. Appl. Phys.* 107, 104106 (2010).



-
- 174) C. W. Nan and D. R. Clarke, *J. Am. Ceram. Soc.* 80, 1333 (1997).
- 175) L. Wu, T. S. Wu, C. C. Wei and H. C. Liu, *J. Phys. C: Solid State Phys.* 16, 2823 (1983).
- 176) J. J. Dih and R. M. Fulrath, *J. Am. Ceram. Soc.* 61, 448 (1978).
- 177) M. Takahash, *Japan. J. appl. Phys.* 10, 643(1971).
- 178) J. Y. Feng and C. M. Chan, *Polym. Eng. Sci.* 38, 1649 (1998).
- 179) B. A. Cook, J. L. Haringa and T. Hansen, *J. Appl. Phys.* 87, 776 (2000).
- 180) L. H. Xu, C. B. Jiang, and H. B. Xu, *Appl. Phys. Lett.* 89, 192507 (2006).
- 181) G. H. Jonker, *J. Phys. Chem. Solids* 9, 165 (1959).
- 182) Y. Yamazaki and M. Satou, *Jpn. J. Appl. Phys.* 12, 998 (1973).
- 183) O. Nakada, *J. Phys. Soc. Jpn.* 15, 2280 (1960).
- 184) Y. Saito, *Jpn. J. Appl. Phys.* 34, 5313 (1995).
- 185) A. J. Masys, W. Ren, G. Yang and B. K. Mukherjee, *J. Appl. Phys.* 94, 2 (2003).
- 186) J. Lu, J. B. Zang, S. X. Shan, H. Huang and Y. H. Wang, *Nano Lett.* 8, 4070 (2008).
- 187) F. Zhao, Y. F. Gao and H. J. Luo, *Langmuir* 25, 6940 (2009).
- 188) Y. R. Dai, P. Bao, J. S. Zhu, J. G. Wan, H. M. Shen and J. M. Liu, *J. Appl. Phys.* 96, 5687 (2004).
- 189) S. Q. Ren, L. Q. Weng, S. H. Song, F. Li, J. G. Wan and M. Zeng, *J. Mater. Sci.* 40, 4375 (2004).
- 190) J. Lu, J. B. Zang, S. X. Shan, H. Huang and Y. H. Wang, *Nano Lett.* 8, 4070 (2008).
- 191) F. Zhao, Y. F. Gao and H. J. Luo, *Langmuir* 25, 6940 (2009).



192) J. Y. Zhai, S. X. Dong, Z. P. Xing, J. F. Li and D. Viehland, *Appl. Phys. Lett.*
91, 123513 (2007).